공학박사 학위논문

작고 무거운 입자에 의해 변화하는 균질 등방성 난류에 대한 실험 및 이론적 연구

Experimental and Theoretical Investigation of Homogeneous and Isotropic Turbulence Modulation by Small and Heavy Particles

2023년 2월

서울대학교 대학원

기계항공공학부

이 훈 상

작고 무거운 입자에 의해 변화하는 균질 등방성 난류에 대한 실험 및 이론적 연구

Experimental and Theoretical Investigation of Homogeneous and Isotropic Turbulence Modulation by Small and Heavy Particles

지도교수 황 원 태

이 논문을 공학박사 학위논문으로 제출함
2022년 10월

서울대학교 대학원
기계항공공학부
이 훈 상

이훈상의 공학박사 학위논문을 인준함
2022년 12월

위 원 장 _____ 김 호 영 _____ (인)

부위원장 _____ 황 원 태 _____ (인)

위 원 _____ 박 형 민 _____ (인)

위 원 _____ 이 창 훈 _____ (인)

위 원 _____ 신 승 원 _____ (인)

Abstract

Understanding turbulence modulation by particles has been a long-standing challenge. Previous studies have proposed various models to predict the modulated physical quantities in particle-laden turbulence. However, these models all have some limitations; moreover, some of them have not been adequately experimentally verified. In this study, turbulence kinetic energy (TKE) and dissipation rate modified by particles have been investigated experimentally using homogeneous isotropic turbulence (HIT). The particle size is 164 μm (comparable to the HIT Kolmogorov scale), and the density is about 2,000 times heavier than the carrier phase which is air. 2D particle image velocimetry (PIV) was used for measuring HIT before and after particle injection. The Taylor microscale Reynolds number of the turbulent flow before particle injection reached up to 271. As confirmed by rms velocity and TKE, the turbulence was fairly homogeneous and isotropic. Energy spectra results also verify that the generated turbulence follows isotropic turbulence theory. When small and heavy particles were added to this HIT, both the TKE and dissipation rate tended to decrease. Starting from the turbulence transport equation, a new physical model for the modulated TKE and dissipation rate was derived. To overcome the limitations of the point-particle approach, additional dissipation occurring at the particle surface and wake effects occurring behind finite-sized particles were considered. The proposed model exhibited satisfactory performance, consistent with the experimental results.

Keywords: Particle-laden turbulence, Multiphase flow, Homogeneous isotropic turbulence, Turbulence modulation, Particle-turbulence interaction

Student number: 2017-24654

Table of Contents

List of Figures

List of Tables

1. Introduction

Turbulent flow laden with particles or droplets can easily be found in nature or industrial applications (Kuerten 2016). Some examples observed in nature are dispersion of small airborne droplets containing a virus (Park et al. 2022), transport of volcanic ash into the atmosphere, and distribution of plankton in the ocean. From an industrial point of view, examples are influx of sand particles into a jet engine, flow in a cyclone separator, and the distribution and behavior of soot particles generated by incomplete combustion inside a combustor.

Various phenomena occur in particle-laden turbulence. When the number of particles in the flow is small, the effect of the particles on the turbulence is negligible. This is termed one-way coupling (Elghobashi 1994). When the number of particles in the flow is further increased, the momentum exchange between the particles and the flow increases. If the momentum the particles give to (or receive from) the flow is sufficiently large, the flow can be modulated as shown in Fig. 1-1 (Lucci et al. 2010), and this is termed two-way coupling (Elghobashi 1994). In the two-way coupling regime, the interaction between the flow and particles should be considered and dynamic motion of the particles need to be solved, which complicates the analysis. In previous studies, various experimental and numerical approaches have been used to improve the understanding of this complex phenomenon and to predict turbulence modulation (Balachandar and Eaton 2010; Kuerten 2016).

Homogeneous isotropic turbulence (HIT) without a mean flow has been widely adapted to enable transformation of complex turbulence equations into simple forms. Squires and Eaton (1990) used direct numerical simulation (DNS) to study the modification of particle-laden HIT. They demonstrated the modulation of the spatial energy and dissipation spectra of turbulence by the particles. As the number of particles increased, the spectra at high wavenumbers increased and at low wavenumbers decreased. This resulted in decreased overall turbulence kinetic energy (TKE) and dissipation rate across the flow field. Boivin et al. (1998) also studied particle-laden stationary HIT using DNS and reported turbulence attenuation similar to that observed by Squires and Eaton (1990). Ferrante and Elghobashi (2003) used DNS to examine the modulation of decaying HIT by particles with various timescales. They showed that the decay rate of TKE decreases when the particle timescale is small; conversely, it increases when the timescale is large. Most of these simulation studies assume the absence of gravity condition to prevent additional energy injection. Rosa et al. (2020) simulated with and without gravity for various

particle sizes and mass loading cases to analyze the effect of gravity on turbulence modulation and particle dynamics. In the absence of gravity, as reported in previous studies, the energy increased at low wavenumbers and decreased at high wavenumbers, showing pivoting. On the other hand, when gravity exists, a large amount of momentum is received from the falling particles, and at the same time, a larger velocity gradient is formed by the particles, resulting in a large increase in energy in medium and high wavenumbers. Although these studies played a major role in improving the understanding of the interaction mechanism between particles and turbulence, they have a limitation in that they used a "point-particle approach," which does not consider the size of the particles (i.e., treating the particle as a point of matter).

To overcome this limitation, a particle-resolved DNS (PR-DNS) technique that resolves the finite-sized particles was developed. Burton and Eaton (2005) first studied a fixed single particle in HIT and observed turbulence modulation. They estimated the influence of the non-slip condition on the particle surface by comparing situations with and without particles. In the local area around the particle, the dissipation rate was greatly increased, whereas the TKE showed a large decrease. This phenomenon does not occur in the point-particle approach. Vreman (2016) performed PR-DNS of HIT with 64 fixed particles. The study confirmed the boundary layer effect in the area around the particle surface and showed that the local dissipation rate was approximately 100 times larger than the spatially averaged value. In addition, a local increase in the dissipation rate around the particle surface has also been reported using PR-DNS in a decaying HIT study (Luo et al. 2017; Schneiders et al. 2017). Shen et al. (2022) identified the effect of particle characteristics on forced HIT through PR-DNS. Particle-fluid density ratio and particle size are the parameters of interest. They reported that the TKE is more decreased as the density ratio increased and as the particle size decreased. They explained that the reason for this phenomenon was that the higher the density ratio, the higher the slip velocity and the higher the dissipation rate on the particle surface, and the smaller the particle size, the lower the probability of vortex occurrence. Mehrabadi et al. (2018) directly compared point particle DNS (PP-DNS) and PR-DNS in decaying turbulence. They showed that in the high Stokes number case, the results of PP-DNS and PR-DNS matched well when drag correction considering the finite Reynolds number was properly performed.

Experiments have also been conducted on the modulation of particle-laden HIT. Hwang and Eaton (2006) created HIT without mean flow in a confined chamber

using synthetic jet actuators. They injected heavy particles on the Kolmogorov lengthscale into the flow and measured the turbulence using particle image velocimetry (PIV). They found that both the TKE and dissipation rate decreased by these particles. Hassaini and Coletti (2022) conducted an experiment using settling particles smaller than the Kolmogorov lengthscale. In their experiment, TKE tended to increase by particles, and in particular, in the highest mass loading, it increased by about 2 times compared to the particle-free turbulence. They cited particle preferential concentration as the reason for the contradictory results of Hwang and Eaton (2006). They claimed that the particles increased the turbulent fluctuations more effectively than high Stokes number particles in localized regions where they formed clusters. Tanaka and Eaton (2010) observed particle-laden turbulence using sub-Kolmogorov-resolution PIV. High-resolution experiments allow access to physical phenomena that occur near the particle surface. Similar to the PR-DNS studies, they also reported an overall decrease in the TKE with an increase in the dissipation rate at the particle surface. Additional information on particle-laden HIT can be found in the review paper by Poelma and Ooms (2006) and Brandt and Coletti (2022)

Based on these results, various efforts have been made to establish a model for turbulence statistics modified by particles. Tanaka and Eaton (2008) proposed a dimensionless number called the particle momentum number, by using a nondimensionalized Navier–Stokes equation that included a fluid–particle momentum coupling term. This dimensionless number succeeded in classifying turbulence attenuation and augmentation in experimental data. However, this model can only discriminate between the attenuation and augmentation of turbulence, and cannot predict the amount of modulation. Hwang and Eaton (2006), Tanaka and Eaton (2010) and Kulick et al. (1994) approached this problem using the Reynolds-averaged transport equation.

They derived a relationship between the modulated TKE and dissipation rate of particles. Crowe (2000) and Schwarzkopf et al. (2009) pointed out the inconsistency in the particle-laden Reynolds-averaged transport equation and suggested a volume-averaged method as an alternative. The model presented by Crowe (2000) could predict the change in turbulence intensity caused by particles, and the model of Schwarzkopf et al. (2009) described the relationship between the modulated TKE and dissipation rate. Although the results of some of these models matched the experimental results fairly well, these models have limitations in that they only explain the relationship between the modified TKE and dissipation rate. In other

words, they cannot predict the extent to which particle-free turbulence is modulated by the particles.

The purpose of this study is to experimentally investigate HIT modulation by small and heavy particles, and to develop a model for predicting it. We focused on the modification of the TKE and dissipation rate, and compared them with the results of various previous models. The validity of the proposed model was confirmed based on the experimental results. In addition, to further develop the model limited by the point-particle assumption, the interaction between the mean kinetic energy (MKE) and additional dissipation occurring at the particle boundary is discussed. The significance of this study lies in the improvement of understanding of two-way coupling and development of a more robust predictive model.

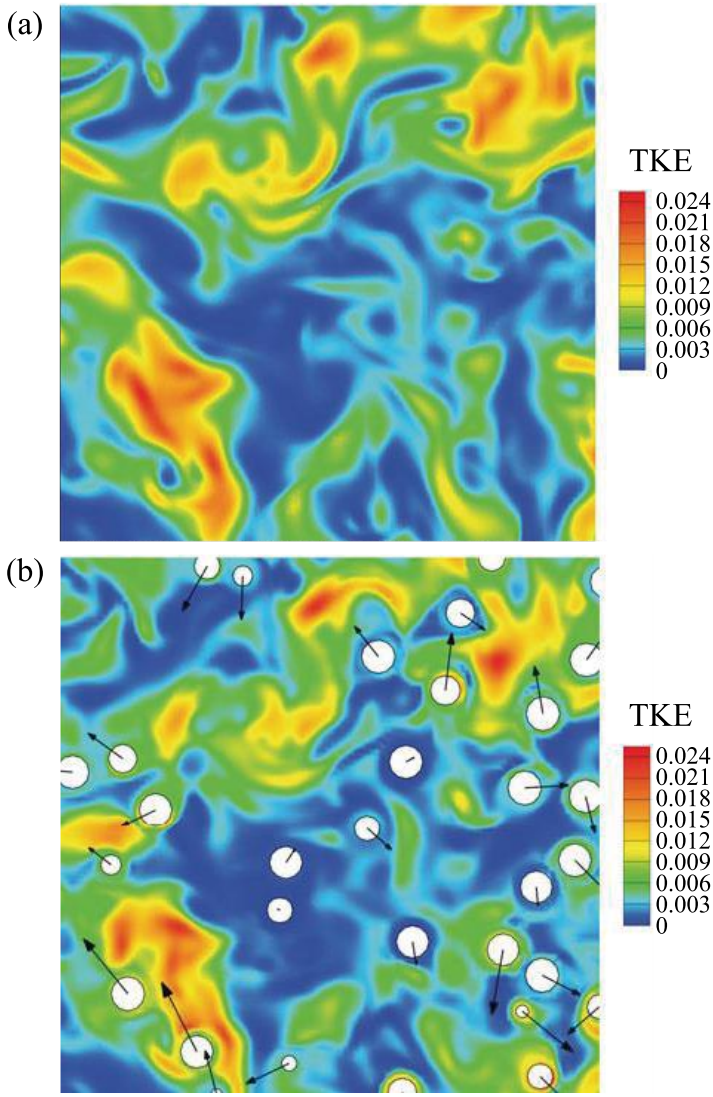

Fig. 1-1 Example of turbulence kinetic energy modulation by particles (a) particle un-laden turbulence (b) particle-laden turbulence. This figure is a reproduction of Fig. 25 in Lucci et al. (2010) *J. Fluid Mech.*

2. Experimental Setup

2.1. HIT chamber and measurement system

To generate HIT, various types of generators suggested by previous studies were considered. The most traditional method is to use grid turbulence (Monchaux et al. 2010). Grid turbulence can be created with a relatively simple method of attaching a passive or active grid to a wind tunnel. However, it does not guarantee isotropy of turbulence and has a strong mean flow, making it unsuitable for studying particle-turbulence interactions. Also, because the turbulent flow decays downstream, it adds complexity to the analysis. To compensate for these shortcomings, Dou et al. (2016) fabricated a flow generator by attaching a fan to a soccer ball-shaped chamber. In this chamber, isotropic turbulence with small mean flow was successfully generated by attaching the same type of fan to 20 faces at the same distance from the center. However, this experimental device has a fan attached to the top, thus heavy particles cannot be dropped and injected while reaching the terminal velocity. In addition, when a fan is used as an actuator, the fan may break down or the particles may be broken due to collision between the fan and the particles.

Considering these points, we fabricated a truncated cube-shaped chamber using the synthetic jet suggested by Hwang and Eaton (2004), as shown in Fig. 2-1 (a). This chamber is identical to that used by Han et al. (2020) and Lee et al. (2018). The truncated cube-shaped acrylic box has a side length of 380 mm, and synthetic jet actuators shown in Fig. 2-1 (b) were attached to the eight vertices. Each synthetic jet actuator was fabricated by attaching an orifice plate to a sub-woofer speaker. A random frequency sine wave generated by a National Instruments LabVIEW analog output module was amplified by a stereo amplifier and then input to the woofer speaker. Different sine waves with random frequencies between 80 and 120 Hz were created. The frequency of the sine wave was changed randomly once every 0.1 s, thus preventing any fixed flow structure from occurring in the turbulence chamber. Fig. 2-2 shows the LabVIEW code for generating a random frequency sine wave using the analog output module. The sine wave generated by the LabVIEW module was measured with an oscilloscope and is shown in Fig. 2-3 (a). It can be seen that the waveform is generated properly without distortion. Fig. 2-3 (b) shows the result of fast Fourier transform (FFT) of the sine wave measured for a sufficiently long time. As can be seen from the figure, the generated sine wave has a frequency mostly between 80 - 120 Hz.

When the diaphragm of the speaker vibrates in accordance with the input voltage

signal, the repeated ejection and suction of air through the 20 mm orifice hole generates a synthetic jet. This jet has zero mean flow and generates only a momentum flux (Kim et al. 2021). The jet moves forward within an ejector tube, breaks up at the mesh, and is then ejected toward the center of the box. Jets from eight directions merge at the center of the box to create HIT. Overheating of the speaker can reduce the intensity of the generated turbulence over time, and thus the speaker is cooled with water at 8°C. The generated turbulence can therefore be maintained in a steady state without decay.

A conventional 2D PIV system was used to measure the HIT generated in the chamber, as depicted in Fig. 2-1 (a). Windows allowed optical access through four sides of the box, and measurements were performed by placing the light source and camera on two orthogonal windows. A dual-cavity 200 mJ Nd:YAG pulse laser with sheet optics module was used as the light source. The laser energy was measured with a power meter for about 300 seconds until the value converges. Fig. 2-4 shows the pulse energy of the first and second laser head. The converged values are 1.40 and 1.44 mJ/pulse, respectively. Although this value is quite a bit smaller than the generally used PIV laser intensity, it was set low to prevent damage of the PIV camera sensor from strong light scattering caused by large particles. A 4 Mpx dual-frame CCD camera with 200 mm focal length lens was used to image the 17.4 × 17.4 mm^2 region of interest (ROI), corresponding to a scale factor of 8.5 μm/px. To compensate for the low laser intensity, the gain of the camera was increased such that the tracers could be imaged.

Aluminum oxide particles (0.3 μm) were used as tracer particles. To prevent the particles from agglomerating due to humidity, they were heated in an oven at 150°C for at least 10 min before the experiment. A fluidized bed seeder discharged the tracers through a cyclone separator to filter any remaining large particles before they finally flowed into the chamber. The PIV images were pre-processed using contrast-limited adaptive histogram equalization, high-pass filtering, and wiener2 de-noise filtering before being analyzed using the open software PIVlab (Thielicke and Stamhuis 2014; Thielicke and Sonntag 2021). PIV analysis was conducted using a two-pass window deformation method (Scarano 2001), starting with the first interrogation window (IW) of 64 px, which was reduced to 32 px for the second window. The experiments were repeated at least five times for each case. All error bars in this manuscript represent 95% confidence interval calculated using Student's t-distribution. Table 2-1 presents the details of the PIV system parameters, which were applied to both pre-unladen and particle-laden experiments.

2.2. Particle description and analysis

Spherical glass particles were used in the turbulence modulation experiments. The size distribution of the particles is shown in Fig. 2-6 (a). Particle size analysis was performed at the Korea Polymer Testing & Research Institute (KOPTRI) using a laser diffraction method compliant with ISO 13320. When a Gaussian distribution was fitted to the particle size distribution, the mean (μ) was 164.4 μm and standard deviation (σ) was approximately 12%. This is reasonable considering that several previous studies used particles with standard deviation of approximately 9 – 17% (Park and Park 2021). The Stokes number in the particle-laden turbulence calculated based on the mean diameter is 90.1, and the values calculated by the $\mu \pm 2\sigma$ are from the 62.7 and 117.

The glass particles were fed into a particle chute (Fig. 2-1) using a magnetic feeder at a height of approximately 3 m from the HIT chamber. A mesh was attached at the inlet of the chute to ensure a homogenous distribution of particles. The particles traveled a sufficiently long distance and reached their terminal velocity before entering the chamber. An electronic scale was placed under the magnetic feeder to measure the weight of particles that left the feeder in a given amount of time. This value was used to calculate the mass or volumetric loading of the particles in the fluid.

The resolution of the scale used in the experiment is 1g. The amount of evacuated particles was measured every 5 seconds, and it was converted to a mass flow rate by linear regression. In order to estimate the accuracy of measurement results due to the low resolution of the scale, we compared the scale used in the experiment with a different scale having 0.1g resolution. By allowing the particles discharged from one scale to flow into the other one, the mass flow rate was obtained from both scales at the same time. Fig. 2-5 shows the mass flow rate measured with the two scales. This graph shows that there was no difference in the measurement result due to the resolution limit.

To quantify the turbulence modulation, particle-laden turbulence must also be measured using PIV. In this case, the glass and tracer particles were imaged together, as shown in the upper panel of Fig. 2-6 (b). It is necessary to separate these particles so that the flow can be measured accurately from the tracers. Because the size of the tracer particle in the PIV image was diffraction limited to approximately 2 – 4 px, it could be removed using a median filter (Kiger and Pan 2000; Hwang and Eaton

2006). Considering the size of the glass particles, a 7×7 px^2 2D median filter was used. The lower-left image in Fig. 2-6 (b) depicts only the large particle that remained after the filtering. By subtracting this image from the original image, an image with only the tracer (as shown on the right side), can be obtained. In the case of large-particle images, the center position of the particle can be obtained through circle fitting, and the displacement (and subsequent velocity) can be calculated using the difference between the center values of the first and second images. In other words, particle tracking velocimetry (PTV) could be applied. The velocity field of the flow was obtained by applying PIV to the images containing only the tracers. Because there were insufficient tracers in the area where large particles were erased, an outlier often appeared and in this case the value obtained by interpolating the surrounding vectors was substituted.

(a)

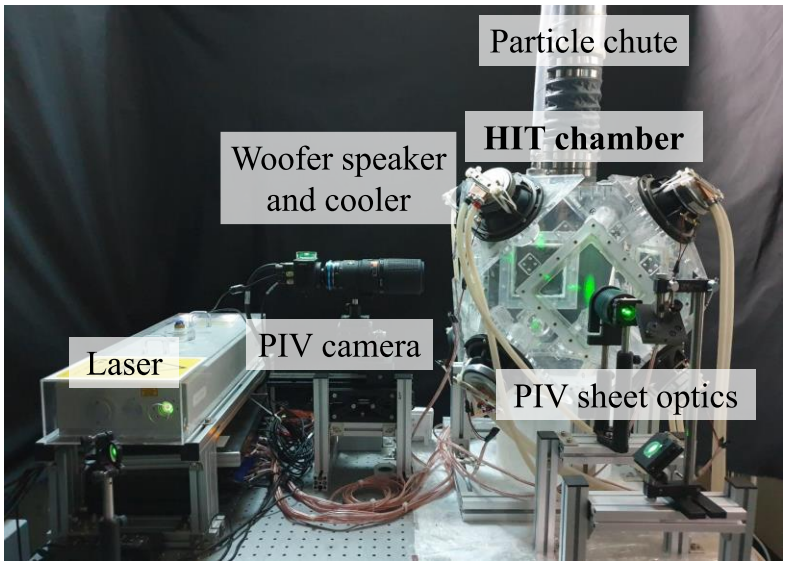

(b)

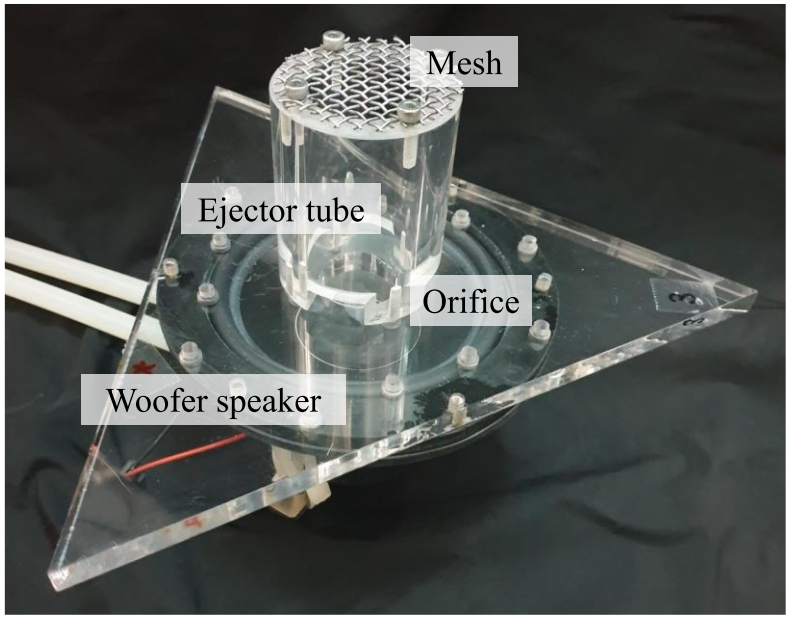

Fig. 2-1 (a) HIT chamber and 2D PIV measurement system, (b) synthetic jet actuator with sub-woofer speaker.

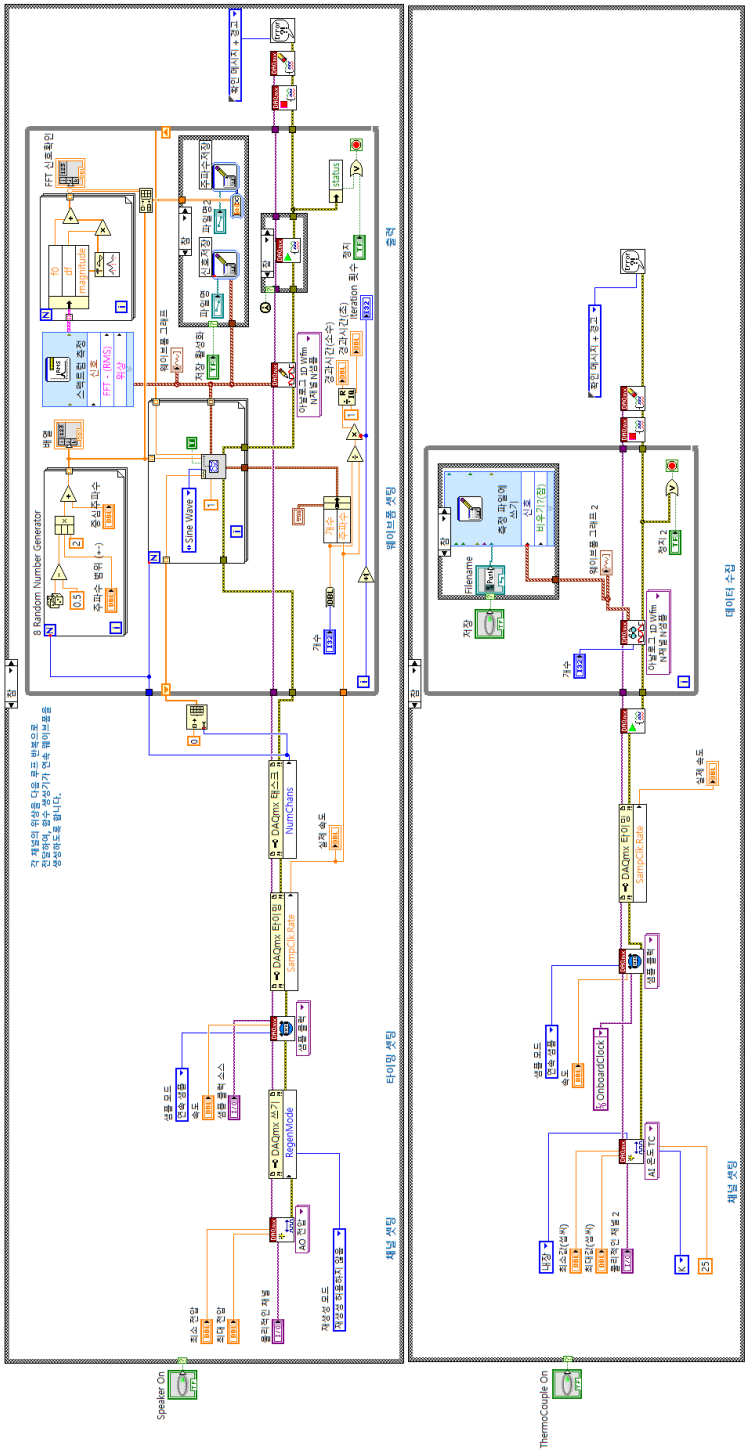

Fig. 2-2 LabVIEW code for generating random frequency sine wave and measuring speaker temperature.

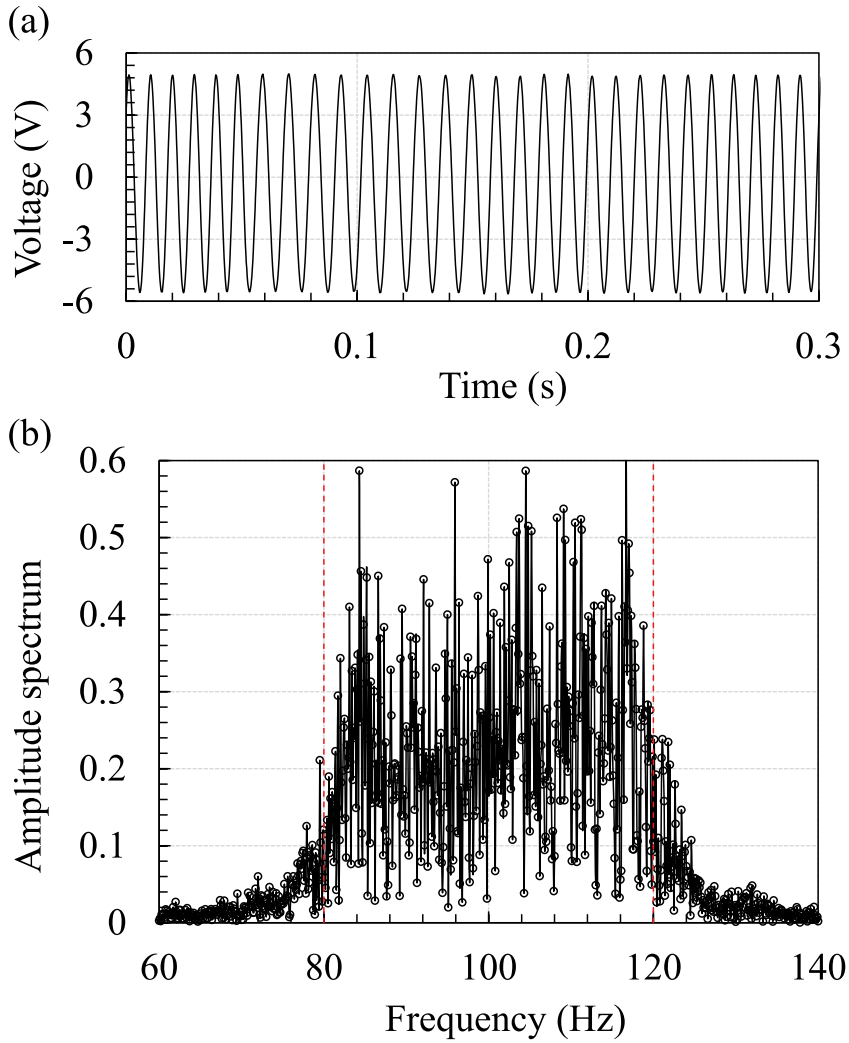

Fig. 2-3 (a) Example of random frequency sine wave generated by analog output module, (b) FFT analysis result of the generated sine wave.

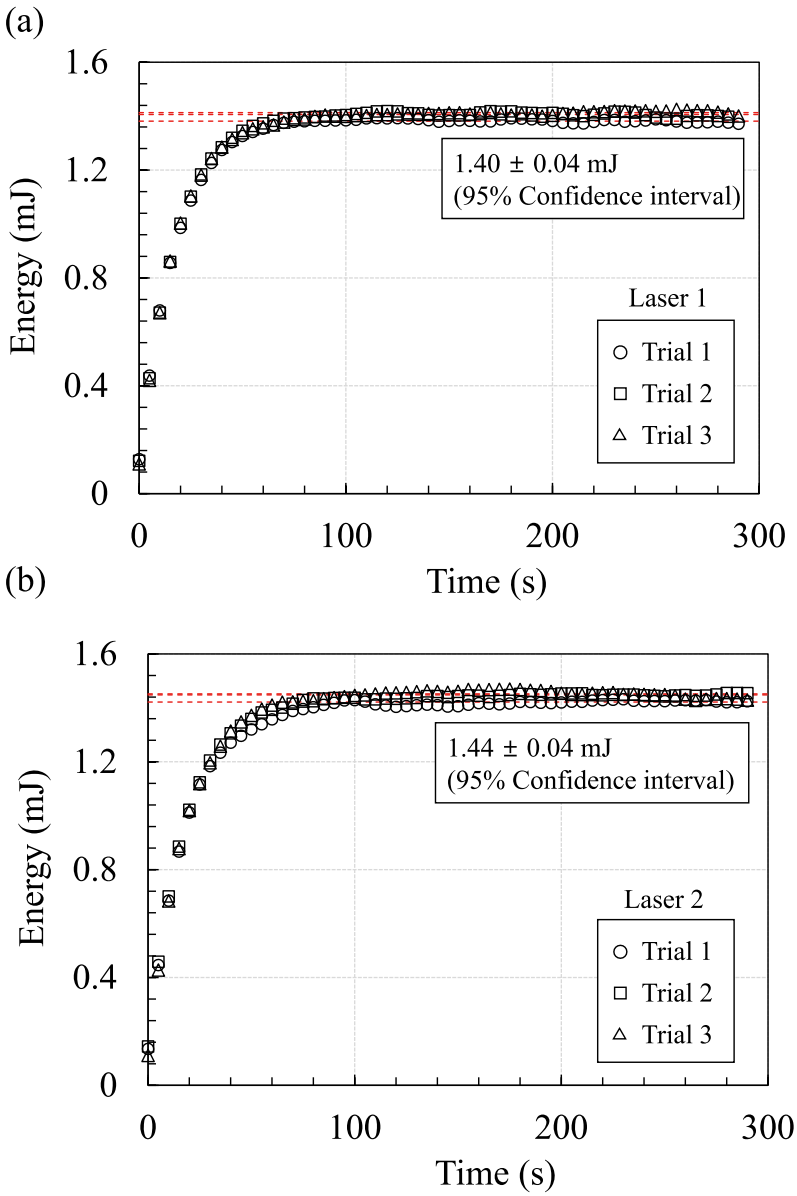

Fig. 2-4 Laser energy for (a) 1st and (b) 2nd head.

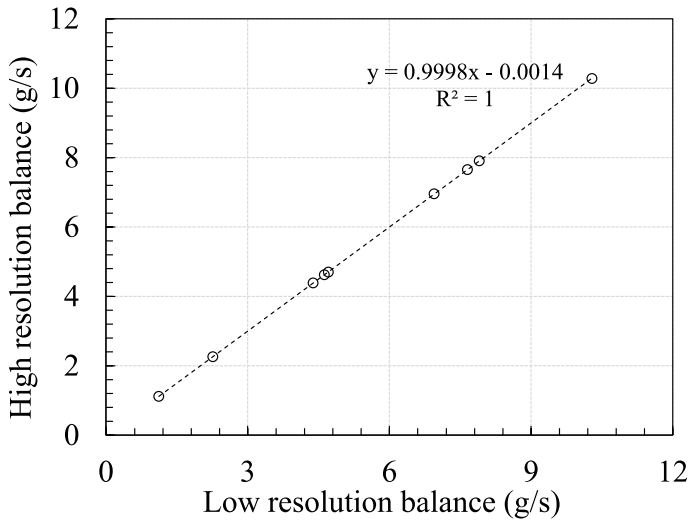

Fig. 2-5 Comparison of mass flow rates measured with low and high resolution balances.

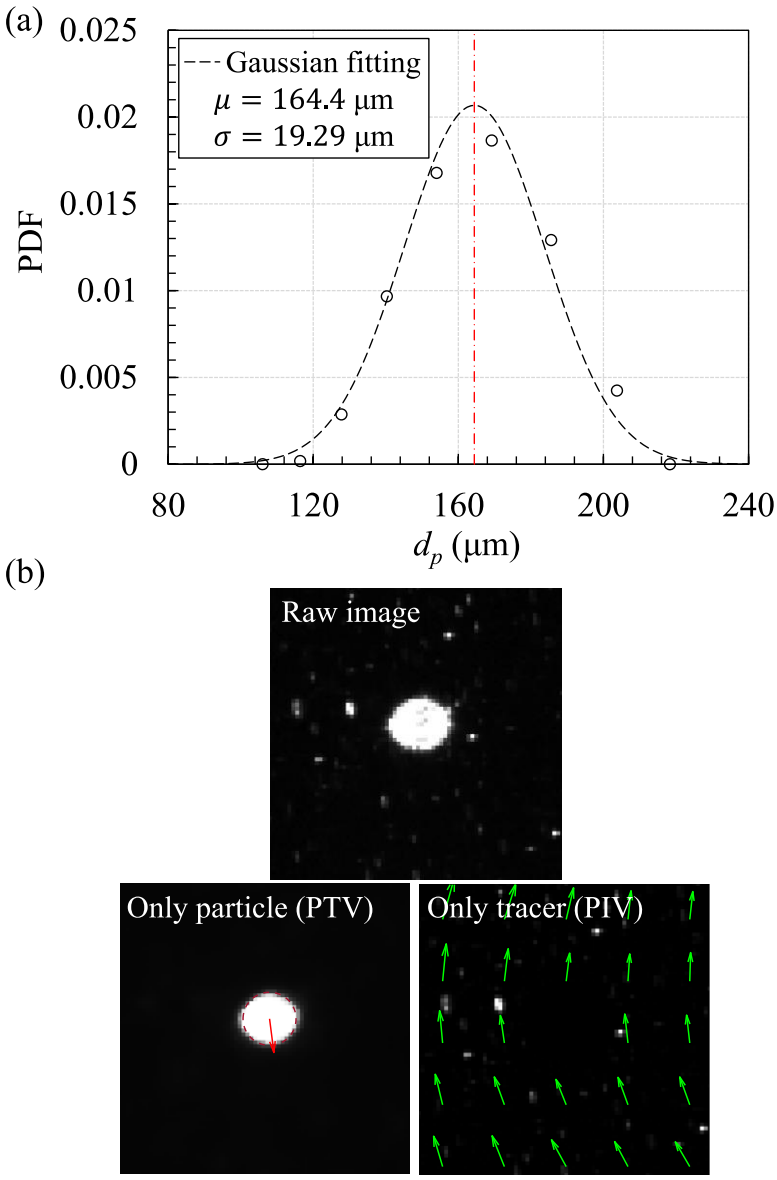

Fig. 2-6 (a) Glass particle size distribution, (b) particle image separation and analysis method for large particles and tracers.

Table 2-1 PIV system parameters.

Laser intensity	1.4 mJ / pulse
Acquisition rate	9 Hz
Camera resolution	2048 × 2048 px^2
ROI	17.4 × 17.4 mm^2
Final IW size	32 × 32 px^2, 50% overlap
Vector spacing	136 μm
Tracer particle	0.3 μm alumina
Number of pairs	1,000 pairs
Number of trials	> 5 times / case

3. Error & Uncertainty analysis

In this chapter, the errors and uncertainties that occur when measuring HIT with 2D PIV are discussed. It has been previously published in Lee and Hwang (2019)[①] and Lee et al. (2022)[②]

3.1. Background

Homogeneous isotropic turbulence (HIT) is an ideal type of turbulence, and many theories related to it have been established. HIT is used in basic turbulence research for its well-defined flow structure and energy cascade, and also in a wide range of engineering flows such as multiphase flow and turbulent premixed combustion (Birouk et al. 1996; Fallon and Rogers 2002; Mazellier et al. 2010; Carter and Coletti 2018). Wind tunnels with passive or active grids have been classically used to create this type of turbulence (Batchelor and Townsend 1947; Comte-Bellot and Corrsin 1966; Roach 1987; Makita and Sassa 1991; De Silva and Fernando 1994). However, this approach has the disadvantage that the mean flow is dominant compared to the fluctuations, and the turbulence decays in the streamwise direction. Hwang and Eaton (2004) first created stationary HIT without mean flow using synthetic jets, and several researchers have built similar apparatuses ever since (Webster et al. 2004; Variano and Cowen 2008; Goepfert et al. 2010; Bellani and Variano 2014; Carter et al. 2016; Dou et al. 2016; Hoffman and Eaton 2021).

For quantitative field measurement of HIT, particle image velocimetry (PIV) (Westerweel et al. 2013) can be used. PIV has been utilized to measure various flows, ranging from basic shear flows, pipe and channel flows, to supersonic flows. Although many of these flows are inherently three-dimensional in nature, 2D PIV is still widely used due to its simple set up and high reliability (Scharnowski et al. 2017a; Scharnowski et al. 2017b). Although HIT is a fully 3D flow, 2D PIV is still

---

[①] Lee H, Hwang W, "Error quantification of 3D homogeneous and isotropic turbulence measurements using 2D PIV." International Journal of Heat and Fluid Flow 78:108431, 2019, © Elsevier

[②] Lee H, Park HJ, Kim M, Han J, Hwang W, "The effect of perspective error on 2D PIV Measurements of homogeneous isotropic turbulence." Experiments in Fluids 63:122, 2022, © Springer Nature

widely being used (Hwang and Eaton 2004; Carter et al. 2016; Han et al. 2020; Hoffman and Eaton 2021), even though three dimensional and three component (3D3C) measurement systems such as tomographic PIV have been developed. This is because 2D PIV is economical and simple to set up compared to a high-dimensional system that requires multiple cameras, more powerful light source, and complicated calibration process. However, when measuring a 3D flow using 2D PIV, the following two problems can occur.

The first problem is loss-of-pair. When particles leave the laser sheet due to 3D motion, the cross-correlation signal can decrease, which increases the uncertainty or number of outliers. Many studies have attempted to determine the effect of loss-of-pair on PIV accuracy. F_o, a parameter that quantifies out-of-plane motion, has been utilized to assess the effect of this motion on PIV uncertainty (Keane and Adrian 1992; Scharnowski and Kähler 2016; Scharnowski et al. 2017b). Westerweel (1997) proposed a PIV design rule in regards to F_o, and Scharnowski and Kähler (2020) analyzed measurement uncertainty according to F_o and showed that the optimal value to increase precision was between 0.6 and 0.9.

The second problem is caused by the 3D motion of particles within the laser sheet, i.e. perspective error. Loss-of-pair causes random error, whereas perspective error is a type of systematic error. It occurs because the 3D motion of the particle is projected onto a 2D image, which affects the 2D displacement measurement. In Section 3.2 and 3.3, the effects of loss-of-pair and perspective error are analyzed in detail, respectively.

3.2. Loss-of-pair

Out-of-plane motion occurs when the tracer particles move in a normal direction to the image plane and disappear. Errors in the measured velocity field will propagate to the turbulence statistics, producing larger errors and consequently distorting turbulence characteristics. Thus, it is important to properly understand 3D flow effects before conducting experiments.

PIV error due to out-of-plane motion has been analyzed previously. Keane and Adrian (1990) analyzed the degradation of correlation peaks by out-of-plane motion through Monte-Carlo simulations and optimized system parameters. They noted that relative out-of-plane displacements of less than 40% may have a valid particle pair detection probability of more than 90% at sufficient particle image density and proper in-plane displacement. Hart (2000) showed that when out-of-plane displacement increases, the probability of valid correlation decreases by up to nearly 30%. He showed that the use of correlation based correction (CBC) can significantly reduce the number of error vectors. It should be noted that these studies focused only on the correlation signal magnitude and error vector detection probability.

There have been attempts to quantify the out-of-plane motion. If the particles disappear from the image due to out-of-plane motion, the matching particle pairs cannot be found between the two consecutive images. This is called loss-of-pair. Keane and Adrian (1992) quantified the loss-of-pair effect through the F_o factor. The F_o factor is a measure of the degree to which particles disappear from the focal plane, based on the degree of intensity change when the laser intensity profile and out-of-plane direction displacement are known. It was defined to be $F_o = 0$ when all the particles lose pairs between the two images by out-of-plane motion, and $F_o = 1$ when there was no loss of pairs. The F_o value is highly correlated with error because when it has a low value, the particle pair detectability and SNR of valid vectors decreases during the cross-correlation process. Keane and Adrian (1990; 1991) selected three factors that affect PIV detectability: F_o, particle image density (N_I), and the normalized correlation of the interrogation intensity across the interrogation window (F_I), and grouped them into one indicator ($N_I F_I F_o$). They created a 'design rule' such that $N_I F_I F_o \geq 7$ (Westerweel 1997), and this criterion has been considered the rule of thumb for many PIV studies. Scharnowski and Kähler (2016) quantified particle displacement error by using this F_o factor and the volume ratio between auto-correlation and cross-correlation. Originally, the F_o factor was difficult to obtain in experiments, because it is necessary to know the out-of-plane direction displacement. This method makes it possible to calculate F_o using images obtained from

experiments. They used synthetic image tests with experiments to take advantage of the ability to precisely control all PIV parameters in a range that is difficult to implement by experimentation. They estimated the displacement vector uncertainty with respect to the F_o value, and optimized this value to minimize the uncertainty. All of these studies have used F_o to assess displacement detectability, uncertainty, and error.

The error and uncertainty of the displacement caused by the out-of-plane motion propagates to velocity error. This, in turn, can have a large effect on turbulence statistics such as turbulence kinetic energy or viscous dissipation rate, which are defined using velocity fluctuations and their spatial derivatives. Wilson and Smith (2013) assessed the propagation of local instantaneous uncertainty from PIV results. They estimated the uncertainty of mean velocity and Reynolds stresses from the velocity uncertainty, due to four parameters: particle image displacement, particle image diameter, particle number density, and the effect of shear. The uncertainty was calculated using the Taylor series method proposed by Wilson and Smith (2013), and validated through experiments. Although they successfully estimated uncertainty for Reynolds stresses, they did not estimate the uncertainty for the dissipation rate, and Taylor or Kolmogorov length scales, which are important statistics in turbulence. In addition, the experiment did not include uncertainty estimation for out-of-plane motion, which can be a significant error source in 2D PIV.

The flow field we are specifically interested in is homogeneous and isotropic turbulence (HIT), which has a significant amount of 3D motion. HIT is the most ideal type of turbulent flow, which can be used to examine basic turbulence theory. There have been many efforts to create HIT in the laboratory. Wind tunnels were initially used to generate turbulence via grids, and HIT was observed within downstream planes. However, the turbulence decays downstream of the grid, and there is a mean flow superposed on the turbulence fluctuations. Birouk et al. (1996) and Fallon and Rogers (2002) implemented HIT with no mean flow in a confined box using rotating fans. Hwang and Eaton (2004) utilized synthetic jet actuators with subwoofers to create a similar flow, and were able to achieve a higher Taylor microscale Reynolds number of 218. They used standard 2D PIV to characterize the flow. Homogeneity and isotropy were quantified using root-mean-square (RMS) velocity fields. Turbulence statistics including turbulent kinetic energy (TKE), dissipation rate, and energy spectrum were calculated.

Many following studies have attempted to generate HIT using a similar approach as Hwang and Eaton (2004), and analysis has been conducted via various

measurement techniques. Zimmermann et al. (2010) obtained the structure function through Lagrangian particle tracking. Using the relationship between the structure function and turbulence statistics such as dissipation rate, Taylor Reynolds number and homogeneity were calculated. The experimental setup was very complicated because three cameras were used. Chang et al. (2012) used laser Doppler velocimetry (LDV) to calculate the structure function by measuring the velocity of two adjacent points in the middle of the instrument. Goepfert et al. (2010) combined 2D PIV with 2 component LDV at two different points in a non-confined experimental setup. They calculated the turbulence statistics by using velocity fields from 2D PIV, assuming that the 3D flow is homogeneous and isotropic as in Hwang and Eaton (2004). Similarly, De Jong et al. (2009) obtained the velocity field in an apparatus with mounted fans using 2D PIV, and calculated the dissipation rate using various methods. Dou et al. (2016) constructed a two-scale PIV technique which consisted of two independent PIV systems to capture the same area at different sizes in a truncated icosahedron-type apparatus. They point out that there is a limit to obtaining turbulence statistics using point measurement techniques such as LDV, which cannot simultaneously measure the spatial covariance of velocity over the region of interest (ROI).

Up to now, most studies have focused on the uncertainty and detectability of the velocity vector due to out-of-plane motion. Since turbulence statistics include first and second order derivatives and correlations, we aim to provide some insight on how the velocity error propagates. The main purpose of this study is to quantify the effect of out-of-plane motion on turbulence statistics measured with 2D PIV in HIT. Synthetic particle images are superimposed on forced isotropic turbulence DNS data, which allows straightforward control of many PIV parameters. Similar to the method of Hwang and Eaton (2004), various turbulence statistics will be calculated, and the 3D flow effects on these statistics will be assessed by comparing the DNS flow fields with the vector fields obtained via PIV. Parameters such as laser thickness, camera inter-frame time, and interrogation window size are optimized to reduce out-of-plane errors in the turbulence statistics. This information can be used to determine how much error results from 2D PIV when characterizing 3D flows such as HIT.

3.2.1. Methodology

3.2.1.1. Synthetic particle image generation

Synthetic particle images are often used to quantify the performance of PIV algorithms and impact of various error sources, because the velocity fields of the moving particles are known, and various PIV parameters can be easily controlled (Stanislas et al. 2003; Stanislas et al. 2005; Stanislas et al. 2008; Kähler et al. 2016). Okamoto et al. (2000a) and Okamoto et al. (2000b) developed a standard evaluation tool that can set various parameters to evaluate PIV algorithms. Parameters such as particle number density, diameter, and laser sheet thickness were investigated. They simulated the particle motion using velocity fields from wall-impinging jet flow obtained via 3-dimensional large eddy simulation (LES). Lecordier and Westerweel (2004) further developed the EUROPIV synthetic image generator, a standard tool for setting more detailed parameters such as the fill ratio of CCD cameras.

Since the purpose of this paper is to quantify the out-of-plane motion effect, conditions are set such that the effects of other parameters such as particle size and distribution are minimized. If the tracer particles are non-uniformly distributed in the flow field, spurious vectors appear in the low particle density regions (Kähler et al. 2012). When the particle size is reduced to under 2 pixels, peak-locking occurs, which makes the particle displacement value an integer. This phenomenon reduces the sub-pixel accuracy regardless of the sub-pixel estimator, and increases the bias error of the displacement (Christensen 2004). With reference to previous studies, these parameters are set to minimize these errors (Wilson and Smith 2013; Raffel et al. 2018). Fig. 3-1 shows an example of a synthetic particle image used in this study. The image size is 1024^2 pixels. The particle number density was set to 0.05 particles per pixel (ppp). Considering the image size, the number of particles is about 52,500. Particles were randomly distributed throughout the image. The size of the particles follow a Gaussian distribution with a mean of 3 pixels and a standard deviation of 1 pixel. The scattering intensity profile of the particles is defined in Eq. (3-1) to simulate a Gaussian distribution (Scharnowski and Kähler 2016; Raffel et al. 2018),

$$I(x,y) = I_0\, e^{-\frac{(x-x_p)^2+(y-y_p)^2}{(1/8)d_p^2}} \tag{3-1}$$

where (x, y) is the coordinates for the image plane displayed in Fig. 3-1. (x_p, y_p) is the center position of the particle, d_p is the particle diameter, and I_0 is the scattering intensity at the center of the particle. I_0 is determined by the laser sheet profile and the particle position within the laser sheet. It is given by the following Eq. (3-2) from Scharnowski and Kähler (2016),

$$I_0(z) = I_{max}\, e^{-\left|\left(\frac{2z}{\Delta z_0}\right)^s\right|} \tag{3-2}$$

where I_{max}, Δz_0, z are the particle brightness at the center of the laser sheet, the sheet width when the light intensity drops to 1/e of the max center value, and particle position within the laser sheet, respectively. In this study, we defined $I_{\max} = 2^8$ to simulate the peak intensity for an 8 bit charge coupled device (CCD) camera. The shape factor $S = 2$, which represents a Gaussian profile. Fig. 3-2 shows the intensity of the laser sheet profile, and the particle intensity distribution according to Eq. (3-2) at three given positions within the laser sheet. As the particle moves away from the laser sheet center (i.e., $z/\Delta z_0$ increases), the scattering intensity of the particle decreases. When a particle starts to leave the laser sheet between an image pair, the intensity decreases, and it reduces the peak of the correlation function, which increases the bias error.

3.2.1.2. Isotropic turbulence flow field

In order to investigate particles with out-of-plane motion, a three-dimensional flow field is required. In order to achieve this, two different approaches have been used for previous studies utilizing synthetic images. In the first approach, an analytic flow field is created, such as a plane shear flow or a tilted vortex (De Kat and Van Oudheusden 2012; Scharnowski and Kähler 2016). However, this type of flow is inherently steady, and velocity fluctuations are not considered. Hence, important turbulence characteristics such as turbulence kinetic energy and viscous dissipation rate are zero. The second method is to use a realistic flow field with velocity fluctuations, obtained using direct numerical simulation (DNS) or LES (Okamoto et al. 2000a; Okamoto et al. 2000b; Kähler et al. 2016). This type of approach is suitable for calculating turbulence statistics because time-dependent velocity changes are simulated. It can also provide sufficient temporal and spatial resolution for gradient calculations. This latter type of flow was selected for the purpose of this study.

The specific flow field we are interested in is HIT. Thus, we decided to utilize forced isotropic turbulence DNS data from the Johns Hopkins turbulent database (JHTDB) (Perlman et al. 2007; Li et al. 2008). The simulation domain is $(0, 2\pi)$ over a 1024^3 grid, with periodic boundary conditions. The temporal resolution of the simulation is 0.0002. Because the DNS data is stored every 10 time steps, the temporal resolution of the data provided is 0.002. Considering the data download capacity and time required, this study used a 4x reduced temporal resolution of 0.008, and reduced spatial domain of 1024 × 1024 × 301. Table 3-1 summarizes the

simulation properties and the main turbulence statistics of the reduced resolution data used in this study, obtained from the JHTDB.

Since the DNS data obtained from the JHTDB are dimensionless, we applied dimensions to it to later compare with experimental data such as that of Hwang and Eaton (2004). Eq. (3-3) shows the relationship between dimensionless variables and variables with dimensions via Reynolds similarity:

$$\nu^* = \frac{1}{Re} = \frac{\nu}{U_c \times L_c} \tag{3-3}$$

where U_C and L_C represent the characteristic velocity and length scale, respectively. The non-dimensional kinematic viscosity ν^* corresponds to the inverse of the Reynolds number, and is given by the JHTDB as 0.000185. On the other hand, ν is the kinematic viscosity with dimensions. In this study, we selected 1.568×10^{-5} m^2/s, the kinematic viscosity of air at 25°C room temperature. If we substitute these values in Eq. (3-3), we can obtain the relationship between the characteristic length and velocity as follows:

$$U_c \times L_c = 0.085\, m^2/s \tag{3-4}$$

The specific characteristic velocity is set to determine the characteristic length, and these two values are used to assign dimensions to the simulation time, velocity, and domain length using Eq. (3-5) to (3-7).

$$t = \frac{L_c}{U_c} \times t^*_{DNS} \tag{3-5}$$

$$\boldsymbol{U}(\mathbf{x}, t) = U_c \times \boldsymbol{U}^*(\mathbf{x}^*, t^*) \tag{3-6}$$

$$\mathbf{x} = L_c \times \mathbf{x}^* \tag{3-7}$$

where t^*_{DNS}, $\mathbf{x}^*$, and $\boldsymbol{U}^*$ are non-dimensionalized time, length, and velocity, respectively, used in the DNS. Based on the HIT chamber from Hwang and Eaton (2004), we adopt U_c = 2.5 m/s as a suitable velocity, so L_c = 0.034 m, which can be considered a representative eddy size. Tracer particle movement was calculated every 10 μs and stored at every predetermined camera inter-frame time step.

3.2.1.3. PIV using synthetic images

The error due to out-of-plane motion in PIV is affected by several variables. Among them, laser sheet thickness, out-of-plane velocity, and camera inter-frame time are considered to have significant effect (Raffel et al. 2018). In addition, the effect of out-of-plane motion may also occur if the two laser pulses of the dual cavity

laser are spatially misaligned, or do not match in beam profile (Scharnowski et al. 2017a; Scharnowski et al. 2017b). In this study, the effect of laser sheet thickness (Δz_0) and camera inter-frame time (Δt) on the error in turbulence statistics is estimated. We also estimate the effect of the PIV interrogation window size (W_s) for each case. Table 3-2 shows the conditions of synthetic image generation using the JHTDB for various cases. Each value is non-dimensionalized by the Kolmogorov length scale η and time scale τ_k from DNS, and the dimensionless values are indicated by the subscript *. Therefore Δz_0^*, Δt^*, and W_s^* given in the table are the dimensionless laser thickness, inter-frame time, and interrogation window size, respectively.

The thickness of the laser sheet is varied between 200 - 1,000μm, which is a typical range for PIV. The inter-frame time, assuming an ultra-high speed camera, is varied from 25,000 to 6,250 frames per second (fps), which is equal to 40 - 160μs. For each case, we also denote the spatial average of the intensity correlation of two successive laser pulses with out-of-plane motion (F_o). F_o is an index that quantitatively evaluates the out-of-plane motion, and the details of this factor are described in the next section. In essence, the lower the spatial averaged F_o value ($\langle F_o \rangle$) is, the out-of-plane effects become more pronounced, and the number of particles disappearing in the image increases. For all cases, the W_s was varied between 16, 32, and 64px squared, with 50% overlap which is commonly used in PIV.

The PIV software that was utilized is an in-house code developed by Sung (2001). Typical cross-correlation technique with fast Fourier transform (FFT) is utilized after image sharpening pre-processing is applied. After the velocity is obtained from the cross-correlation result, we applied post-processing to the vector field. There are various kinds of PIV post-processing, but there is no method or criteria that can completely eliminate spurious vectors. In this study, we used methods and criteria commonly used in PIV experiments. Spurious vectors are detected using two validation methods, primary peak ratio (PPR) and particle displacement range. PPR is the ratio between the primary peak, which is the highest peak obtained through cross correlation, and the second highest peak. For general PIV, the criterion of PPR is about 1.2 (Xue et al. 2014). Hain and Kähler (2007) suggest that this value should be at least 2.0 to avoid error vectors. Thus, for this study, velocity vectors having PPR lower than 2.0 are classified as error vectors. These vectors are then validated once more to ensure they are within a set displacement range. The threshold of the displacement range is set to 2, 4, 6, and 8px, respectively, proportional to the inter-

frame time, to keep the degree of spurious vectors consistent with the amount of out-of-plane motion. These values are selected by considering the largest displacement calculated from DNS at the inter-frame time for each case. Error vectors are corrected using a spatial average filter, which averages the eight neighboring vectors. The results obtained are used as the final PIV results.

In order to verify that the in-house PIV software works properly, we calculated the displacement error and the total kinetic energy from the velocity fields obtained in case 2 from Table 3-2, which has a relatively small amount of out-of-plane motion. The displacement error was calculated by subtracting the DNS displacement value from the PIV displacement value, and then taking spatial and ensemble averages. The displacement error was found to be about 0.2px, indicating reasonable PIV accuracy. Because of the filtering and smoothing effects of PIV itself, the turbulent kinetic energy calculated by PIV was underestimated by 10%, but this was deemed sufficient as initial verification for the in-house code.

Fig. 3-3 (a) shows a sample instantaneous 2D velocity field obtained from 3D DNS, (b) normalized out-of-plane velocity from DNS, (c) velocity field from 2D PIV, and (d) difference between PIV and DNS. Since the spatial resolution of DNS is much higher than that of PIV, a box filter of the same size as the PIV interrogation window is applied to the DNS data for comparison. It can be seen that the flow structure and velocity magnitude are similar to each other. This provides verification that the synthetic images are well constructed, and that the PIV software is working properly.

3.2.2. Results

Some turbulence statistics were selected to characterize the HIT, with reference to the study of Hwang and Eaton (2004). Turbulence kinetic energy (TKE), dissipation rate, Taylor microscale, Kolmogorov length and time scale, and velocity correlations are calculated from the DNS data and simulated PIV results. Before elaborating on the turbulence statistics, velocity error is first examined, to assess the synthetic images and PIV algorithm. This can provide a basic understanding of various error sources and out-of-plane motion effect.

3.2.2.1. Instantaneous velocity

To assess the velocity error, one line was selected parallel to the horizontal x-axis in the flow field of Fig. 3-3. To quantify the out-of-plane motion along this line, we used F_o defined by Keane and Adrian (1992) as follows:

$$F_o = \frac{\int I_1(z - z_1) \times I_2(z - z_2 - \Delta z)dz}{\int I_1(z) \times I_2(z)dz} \tag{3-8}$$

where $I_1(z)$ and $I_2(z)$ denote laser sheet intensities for two consecutive images. z_1 and z_2 are the offset distance of the laser sheet center from the ROI plane, and Δz is the out-of-plane direction displacement of the particle. In this study, assuming that the laser intensity profile is the same between the pulses, and the ROI plane and laser sheets are aligned exactly, the simplified Eq. (3-9) is used.

$$F_o = \frac{\int I(z) \times I(z - \Delta z)dz}{\int \{I_1(z)\}^2 dz} \tag{3-9}$$

where I(z) is from Eq. (3-1). F_o has a value of 1 if there is no out-of-plane motion of the particles. On the other hand, if the motion is large, it will be zero. Fig. 3-4 (a) shows the F_o value obtained from DNS along the selected line for three small inter-frame times with non-dimensional laser sheet thickness $\Delta z_0^* = 3.37$. The horizontal position x is normalized by the magnification factor δ in PIV. For a small inter-frame time of $\Delta t^* = 0.043$, F_o is relatively large with an average of 0.92, and a minimum of 0.68 on the left-hand side of the image which indicates large amount of out-of-plane flow in this region. When the interframe time was doubled, F_o was greatly reduced in a nonlinear fashion. In particular, the minimum value was reduced by about 1/3 to 0.21, and the average value was 0.75.

Fig. 3-4 (b) and (c) depict the in-plane horizontal direction velocity along the aforementioned horizontal line obtained from DNS and PIV for case 5 and 6 in Table 3-2, respectively. The red, blue and green lines represent the results for different W_s. In Fig. 3-4 (b), smaller W_s capture more of the fluctuation velocity. The large W_s does not adequately capture fluctuations, but overall trends are nevertheless similar to DNS.

Fig. 3-4 (c) shows a case with larger out-of-plane motion than (b) by increasing the camera's interframe time. When W_s^* is 18.58, there is a noticeably large error at x/δ = 180, 220 and 600. These points coincide with the small F_o regions in Fig. 3-4 (a). The absolute error at each location is calculated as the absolute difference between the PIV data and DNS data averaged over a window of the same size as the PIV W_s. This error averaged along the selected line is $\Delta U_x/U_c = 0.21$ for $\Delta t^* = 0.086$

(Fig. 3-4c) when the normalized W_s is 18.58. It is about twice higher than the average error value of 0.086 for $\Delta t^* = 0.043$ (Fig. 3-4b).

We also calculated the in-plane mean horizontal velocity for different inter-frame times for the case of $W_s^* = 18.58$ as shown in Fig. 3-4 (d). Although the mean profile still somewhat follows the instantaneous trend due to the limitation in duration of time averaging (as mentioned in Table 3-1), it can be seen that the mean velocity is slightly less sensitive to out-of-plane motion than the instantaneous field, even though F_o changes quite a bit for different inter-frame times.

The results of Fig. 3-4 suggest that when large out-of-plane motion is present, a smaller interrogation window size along with a shorter inter-frame time should be used for PIV.

3.2.2.2. Turbulence kinetic energy

TKE is the mean kinetic energy per unit mass in the fluctuating velocity field. TKE is defined to be the sum of the diagonal components of the Reynolds stress tensor (Pope 2000), as shown in Eq. (3-10),

$$k = \frac{1}{2}\overline{u_i u_i} \tag{3-10}$$

where u_i is the velocity fluctuation in the ith direction and overbar denotes an ensemble average. Since the result obtained through 2D PIV is a 2D velocity field, Eq. (3-10) can be converted into Eq. (3-11) assuming isotropy.

$$k = \frac{3}{4}\overline{u_1^2 + u_2^2} \tag{3-11}$$

Fig. 3-5 (a) shows the normalized TKE calculated using Eq. (3-11) for the DNS and PIV dataset along the line from Fig. 3-3. As shown in the graph, the larger the W_s, more underestimation occurs relative to the true (DNS) value. Since TKE is based on velocity fluctuations, this phenomenon occurs when the W_s is too large to capture the fluctuations properly. Fig. 3-5 (b) shows TKE according to camera interframe time when W_s^* is the medium size of 37.17. TKE from PIV is generally underestimated at this W_s. However, overestimation occurs at the highest interframe time due to errors occurring from large out-of-plane motion.

Fig. 3-6 shows the error of TKE for several cases, spatially averaged over the entire flow field. Fig. 3-6 (a) shows this error variation with laser thickness for three W_s. The error is calculated by the following equation:

$$D_f = f_{\mathrm{PIV}}/f_{\mathrm{DNS}} - 1 \tag{3-12}$$

where f represents an arbitrary turbulence statistic. The subscript PIV and DNS indicates the source of the data used to calculate the corresponding statistic. Since the spatial resolution of DNS and PIV is different, the DNS value is averaged over a window the same size as the PIV interrogation window, in order to calculate the error. The range of error for TKE calculated in this fashion is larger than 30%, and reaches beyond 70% under certain conditions. This is because PIV underestimates TKE due to the low spatial and temporal resolution, as illustrated in Fig. 3-5.

Depending on the W_s, the TKE error trend with laser sheet thickness differs, as can be seen in Fig. 3-6. For the smallest W_s ($W_s^* = 18.58$), the error is relatively high for the thinnest laser sheet, as shown in Fig. 3-6 (a). This is due to the large out-of-plane motion, which is evidenced by the relatively small F_o value in Table 3-2. For a small W_s, the error due to out-of-plane motion can be larger than that of a larger W_s, because there is likely an insufficient number of particle pairs to calculate the velocity, as demonstrated in Fig. 3-6 (b). It should be noted that even if a multigrid algorithm such as window deformation or offset (Scarano and Riethmuller 1999; Scarano and Riethmuller 2000; Scarano 2001) were to be utilized, only in-plane loss of pairs are expected to be reduced. It is difficult to compensate for out-of-plane loss of pairs using multigrid algorithms.

When the normalized laser sheet thickness increases from the initial value of 1.69 to 3.37, the error drastically decreases from 60% to 30%, because the out-of-plane motion is smaller (F_o is larger), and the velocity can be accurately obtained. For the two larger W_s values ($W_s^* = 37.17$, 74.34), the TKE error is lowest for the thinnest laser sheet. This is because the underestimation of TKE for large W_s (as seen in Fig. 3-5a) compensates for the overestimation of TKE due to out-of-plane errors for the thin laser sheet. When the out-of-plane motion is small for Δz_0^* beyond 3.37, this compensation effect is not present.

When the normalized laser sheet thickness (Δz_0^*) increases from 3.37, error increases slightly regardless of the W_s. Since the influence of out-of-plane motion is small due to the large F_o, this is likely due to the thicker laser sheet. As more volume is included in the PIV interrogation window, the TKE will start to deviate from the planar DNS value.

Fig. 3-7 estimates TKE error according to the interframe time. For the smallest interframe time, smaller W_s results in smaller error. This is due to the underestimation of TKE with larger W_s (as seen in Fig. 3-5a). As the interframe time increases, the

error increases drastically for the smallest W_s, and slightly for the medium W_s. As the spatial average value of F_o becomes smaller than 0.87, the error due to the out-of-plane motion becomes more dominant than that due to the limited spatial resolution. This effect is amplified for the smaller W_s, as demonstrated in Fig. 3-6 (b).

Fig. 3-8 shows the distribution of local TKE error D_k throughout the flow field (as opposed to the spatially averaged TKE error $\langle D_k \rangle$), as a function of (original) F_o for different W_s. The normalized interframe time and laser sheet thicknesses of the plots are 0.171 and 3.37, respectively. Note that the y-axis log scale of each graph is different. For the smallest W_s in Fig. 3-8 (a), the error generally decreases for smaller out-of-plane motion (larger F_o), but there is a significant spread of data at the largest F_o, ranging from 0.01% to over 1000%. This suggests that even when the out-of-plane effect is small, errors can be still be significant if there are not enough particle pairs in the small W_s. The spread in data for the $W_s^* = 37.17$ case in Fig. 3-8 (b) is also large, but a slight decrease in error up to about $F_o = 0.4$ can be noticed, and beyond that the error remains constant. For the case where the W_s is the largest in Fig. 3-8 (c), the error remains relatively constant even at small F_o, because the underestimation of TKE due to the limited spatial resolution (evidenced in Fig. 3-5a) is offset by the overestimation caused by out-of-plane errors. The graphs in Fig. 3-8 are summarized in Fig. 3-9, where D_k is binned by F_o to show change in average D_k. The average D_k is calculated from at least 39 samples in each bin. The error bars indicate the 95% uncertainty range for the scattered data.

The non-dimensional F_o factor is originally defined as a function of the laser sheet profile and velocity (displacement) perpendicular to the plane. However, for experimental data the out-of-plane velocity is not known. A modified $F_{o,\ mod}$ can be defined from the images alone, as the ratio of the cross-correlation peak to the auto-correlation peak values, based on a concept proposed by Scharnowski and Kähler (2016). Using this concept, effects from image processing can be evaluated. For example, the effect of image pre-processing on the out-of-plane motion was assessed. This study mainly used image sharpening, which is a widely used method in PIV analysis. This particular technique did not have any noticeable effect on TKE, compared to when just the raw images without any pre-processing were analyzed with the PIV algorithm. Contrast-limited adaptive histogram equalization (CLAHE), which is a commonly used intensity normalization pre-processing method, was also evaluated for cases 5 through 8, with 16 and 32px interrogation windows. These cases were selected because they have a wide range of out-of-plane motion. We obtained $F_{o,\ mod}$ from the CLAHE image and the raw image of these cases and

calculated the TKE error from the PIV result, as shown in Fig. 3-10. The $F_{o,\,mod}$ values obtained from the raw image and original F_o shown in Table 3-2 are similar to each other. As can be seen in Fig. 3-10, when the $F_{o,\,mod}$ factor is used, the spatially-averaged TKE error when CLAHE is applied follows the trend computed from just raw images fairly well. This graph demonstrates that if the F_o factor is estimated from the images, the TKE error level can be predicted for actual experiments with out-of-plane motion, when pre-processing such as CLAHE is applied to the images.

3.2.2.3. Viscous dissipation rate

In turbulence, energy is cascaded from large-scale eddies to small-scale eddies, and eventually dissipated as heat at the Kolmogorov scale, which represents the smallest scale in turbulence. To understand the structure and physics of the turbulent flow, it is important to obtain the viscous dissipation rate accurately. The dissipation rate is proportional to the viscosity and strain rate, as definition in Eq. (3-13):

$$\varepsilon = 2\nu\overline{s_{ij}s_{ij}} \tag{3-13}$$

where ν is the kinematic viscosity and overbar denotes ensemble averaging. s_{ij} is the strain rate for the velocity fluctuations and is defined by Eq. (3-14):

$$s_{ij} = \frac{1}{2}\left(\frac{\partial u_i}{\partial x_j} + \frac{\partial u_j}{\partial x_i}\right) \tag{3-14}$$

where u_i denotes velocity fluctuations in the ith direction. Substituting Eq. (3-14) into Eq. (3-13) and applying the Einstein summation convention and isotropy assumption for 2D measurements, the dissipation rate can be written as Eq. (3-15):

$$\varepsilon = \nu\left[\overline{4\left(\frac{\partial u_1}{\partial x_1}\right)^2} + \overline{4\left(\frac{\partial u_2}{\partial x_2}\right)^2} + \overline{4\left(\frac{\partial u_1}{\partial x_1}\frac{\partial u_2}{\partial x_2}\right)} + \overline{3\left(\frac{\partial u_1}{\partial x_2} + \frac{\partial u_2}{\partial x_1}\right)^2}\right] \tag{3-15}$$

Direct calculation of dissipation from Eq. (3-15), however, requires spatial resolution smaller than the Kolmogorov length scale (Sheng et al. 2000). If the spatial resolution is larger than the Kolmogorov length scale, the values obtained by this method will have large errors (Xu and Chen 2013). Thus, this direct method may be suitable for DNS data, but is not appropriate for PIV where the spatial resolution given by the W_s is generally larger than the Kolmogorov length scale.

Various methods for obtaining the dissipation rate using PIV data with limited resolution are described in De Jong et al. (2009) and Xu and Chen (2013). A widely used method first proposed by Sheng et al. (2000) employs the concepts of large

eddy and sub-grid scales (SGS) in LES. They estimated the dissipation rate assuming dynamic equilibrium, where the amount of turbulence kinetic energy production occurring in large eddies equals the amount dissipated at the sub-grid scale. The method utilizes the Smagorinsky model, and is thus limited by the accuracy of the model itself. Several previous studies of HIT have estimated the dissipation rate using this method. The purpose of this study is to understand the effect of out-of-plane motion on turbulence statistics, so the analysis of errors from the model itself are considered out of scope. The dissipation rate can be obtained from Eq. (3-16) and (3-17):

$$\varepsilon \approx \overline{\varepsilon_{\mathrm{SGS}}} = -2\overline{\tau_{ij}\check{S}_{ij}} \tag{3-16}$$

$$\check{S}_{ij} = \frac{1}{2}\left(\frac{\partial \check{u}_i}{\partial x_j} + \frac{\partial \check{u}_j}{\partial x_i}\right) \tag{3-17}$$

where τ_{ij} and $\check{S}_{ij}$ are the SGS stress and the resolved-scale strain rate, respectively. $\check{u}_i$ is the resolved velocity fluctuation, which is obtained from PIV. SGS stress can be calculated from various LES models. The eddy viscosity model proposed by Smagorinsky is as follows (Pope 2000):

$$\tau_{ij} = -C_s^2 \check{\kappa}^2 \check{S}_{ij}\sqrt{2\check{S}_{mn}\check{S}_{mn}} \tag{3-18}$$

where $\check{\kappa}$ is the filter size, which is equal to the W_s in PIV. C_s is the Smagorinsky coefficient, which is proportional to the filter size used (Pope 2000). This constant can be obtained analytically or determined empirically (Langford and Moser 1999). The product of the strain rate tensor can be transformed using isotropy and the continuity equation as follows:

$$\check{S}_{mn}\check{S}_{mn} = \overline{2\left(\frac{\partial \check{u}_1}{\partial x_1}\right)^2} + \overline{2\left(\frac{\partial \check{u}_2}{\partial x_2}\right)^2} + \overline{2\left(\frac{\partial \check{u}_1}{\partial x_1}\frac{\partial \check{u}_2}{\partial x_2}\right)} + \overline{\frac{3}{2}\left(\frac{\partial \check{u}_1}{\partial x_2} + \frac{\partial \check{u}_2}{\partial x_1}\right)^2} \tag{3-19}$$

when calculating Eq. (3-19) with 2D PIV data, second-order finite differences were used throughout the domain, with first-order finite differences at the boundaries.

To calculate the dissipation rate, a proper C_s must first be selected. In Lilly's analysis and previous studies (Lilly 1967; Sheng et al. 2000), C_s was set to 0.17. In other studies (Canuto and Cheng 1997; De Jong et al. 2009), a corrected value of 0.12 was used. The value of C_s does not seem to be universal, but can change slightly depending on the situation. It should be noted that for LES, C_s is modified for each step of the calculation to obtain accurate results. In this study, we attempted to find an optimum Smagorinsky coefficient which makes the dissipation rate error minimum. C_s acts as a simple proportional constant multiplied to the dissipation rate,

thus the optimized C_s appropriately offsets the dissipation rate value to minimize errors. The dissipation rate obtained from 2D PIV was calculated by using a C_s value in the range of 0 to 0.25 for the different W_s, and compared against the 3D DNS value. Fig. 3-11 shows how the sum of the difference squared varies with C_s. The error is minimized when C_s is 0.07, 0.145 and 0.21 for W_s^* = 18.58, 37.17, and 74.34, respectively. These values are close to the commonly accepted range between 0.1 - 0.2 (Langford and Moser 1999).

Fig. 3-12 (a) shows the non-dimensional dissipation rate along the horizontal line in the flow field of Fig. 3-3, when the C_s value was set to the standard 0.17. For the large W_s, the fluctuations are not properly captured due to the limited spatial resolution, and thus the dissipation rate profile does not accurately follow the DNS profile. For the medium W_s, the general trend follows that of DNS, but the high-frequency undulations are not adequately captured. For the smallest W_s with the highest spatial resolution, the undulations are well captured, but there is a large scale factor discrepancy between the DNS data (Langford and Moser 1999). Fig. 3-12 (b) shows the dissipation rate calculated by applying the optimized constants. Compared with Fig. 3-12 (a), the error has decreased substantially for the smallest W_s case, and it can be seen that the undulations are relatively well captured compared to the higher W_s cases. For the highest W_s case, the dissipation rate remains mostly underestimated compared to that of DNS, and the undulations are not well captured because they are filtered out due to the low spatial resolution.

To verify the correlation between the out-of-plane motion and the dissipation rate error, we calculated the spatial average of the error over several flow fields. Fig. 3-13 depicts this spatially averaged error as a function of (a) laser sheet thickness and (b) interframe time for three W_s. Despite optimizing the Smagorinsky constant, the error is at least 50% for all cases due to the 2D measurement limitations, and increases as the out-of-plane motion increases for small W_s and large interframe time. When compared with the TKE error in Fig. 3-6 (a) and Fig. 3-7, the dissipation rate error is much more sensitive to out-of-plane motion, with significantly larger error values. When the W_s is the smallest, at the maximum interframe time the error reaches about 62.4. This is 8.41 times larger than the TKE error of 7.42 at the same conditions. This is likely due to the estimation of 3D velocity gradients with 2D data.

This trend with out-of-plane motion is also shown in Fig. 3-14, where the average error in ε and k are plotted against F_o. To provide comparison with TKE, Fig. 3-9 is shown again as dotted lines. As F_o decreases in the two cases where W_s is small, the error for the dissipation rate begins to increase much quicker than that of TKE. On

the other hand, the largest W_s is insensitive to out-of-plane motion, with error less than 1 for both ε and k. Thus, when measuring the dissipation rate using 2D planar PIV in a 3D flow with significant out-of-plane motion, using a larger W_s can reduce the occurrence of errors.

3.2.2.4. Taylor microscale & Kolmogorov scale

The Taylor microscale is a length scale used to characterize turbulence. It represents an intermediate length scale between the energetic inertial range, and the small dissipation range where viscosity is important. It is defined in terms of TKE, dissipation rate, and kinematic viscosity. The Taylor microscale (λ) and Taylor Reynolds number (Re_λ) are expressed by the following equations:

$$\lambda = \left(\frac{10\nu k}{\varepsilon}\right)^{1/2} \qquad Re_\lambda = \frac{\lambda(2k/3)^{1/2}}{\nu} \tag{3-20}$$

where ν, k, and ε are kinematic viscosity, TKE, and dissipation rate, respectively. The Kolmogorov scale represents the smallest eddies where energy dissipation occurs, and also plays an important role in characterizing turbulence. The Kolmogorov time scale (τ_k) and length scale (η) can be obtained from Eq. (3-21):

$$\tau_k = (\nu/\varepsilon)^{1/2} \qquad \eta = (\nu^3/\varepsilon)^{1/4} \tag{3-21}$$

Fig. 3-15 shows the relative frequency distribution of Taylor and Kolmogorov length scale error over the entire flow field for various interframe times when the W_s^* is 18.58 and 37.17. The relative frequency distribution was obtained by setting the error bin to 0.1. If the error value is negative, it corresponds to underestimation of the PIV measurement. The opposite case corresponds to overestimation. As shown in these two graphs, when the out-of-plane motion is not significant for small interframe time, the average error is close to 0 and the range is about -1 to 1.5. It is interesting to note that as the interframe time increases, the peak of the distribution decreases and a new peak starts to occur at an error value in between -1 and -0.5. This is indicated by the black arrows in the graph. This means that the length scale measured by PIV becomes underestimated due to the increase in out-of-plane motion. The dotted-line graph shows two interframe time cases for a larger W_s. In the case of the Taylor length scale, the error distribution is shifted to the left. Since the sensitivity for out-of-plane motion decreases with the larger W_s, the shape of the second peak is hardly noticeable, but the distribution is widened. For the Kolmogorov length scale, the error shift does not occur with W_s for small interframe time, but a distinctive

second peak is generated with a wider distribution for larger interframe time. Unlike the Taylor length scale, which is a function of both dissipation rate and TKE, the Kolmogorov length scale is only a function of dissipation rate. Since the dissipation rate uses an optimized Smagorinsky constant for each W_s, the resulting bias error shift does not occur for a change in W_s.

3.2.2.5. Two-point velocity correlation

The correlation tensor refers to the correlation of velocity fluctuations at different locations, and is defined as follows (Mathieu and Scott 2000):

$$R_{ij}(r) = \overline{u_i(x)u_j(x+r)} \tag{3-22}$$

The non-dimensional longitudinal velocity correlation coefficients (F_{11}, F_{22}) are given as:

$$F_{11}(r) = \left\langle \overline{u_1(x_1,x_2)u_1(x_1+r,x_2)} \right\rangle / \left\langle u_{1,rms}^2 \right\rangle \tag{3-23}$$

$$F_{22}(r) = \left\langle \overline{u_2(x_1,x_2)u_2(x_1,x_2+r)} \right\rangle / \left\langle u_{2,rms}^2 \right\rangle \tag{3-24}$$

where the $\langle\cdot\rangle$ denotes spatial averages.

Fig. 3-16 (a) and (b) show the longitudinal velocity correlation coefficient F_{11} and F_{22} as a function of r, normalized by the Kolmogorov length scale. The solid lines on both graphs represent the smallest W_s and the dotted lines represent the largest W_s. Only the smallest and largest interframe time cases are shown, to demonstrate the clear effect of out-of-plane motion. For the small $W_s^* = 18.58$ and $\Delta t^* = 0.043$, the correlation matches the DNS data very well. As the interframe time is increased, the correlation is drastically reduced because of out-of-plane data dropout. For the large W_s case, the correlation value is larger than that of DNS, because of the averaging effect over the larger W_s. When the correlation coefficient converges to zero, the integral length scale can be calculated by integrating the curve (Hwang and Eaton 2004). The integral length scale for the small interframe time and W_s case is 42.96, which is similar to the DNS value of 48.72. As expected, when the interframe time is increased to $\Delta t^* = 0.171$ for the small W_s case, the integral length scale is underestimated at 12.68.

3.3. Perspective error

In this section, we investigate the effect of perspective error on turbulence statistics. Several previous studies have addressed this error before. Raffel et al. (2018) theoretically showed that the perspective error increases with distance from the optical axis of the lens. They suggested the use of a lens with a longer focal length as an alternative to increasing the working distance or reducing the observation angle. Lecordier and Westerweel (2004) included this error effect in synthetic particle image generators. By using the geometry of the optical imaging system, the error could be expressed mathematically, and it was shown that the displacement error reached or exceeded 0.5 px depending on the experimental setup. This value significantly exceeds the generally accepted PIV uncertainty of 0.1 px.

Experimental approaches have been adopted to address this perspective error. Yoon and Lee (2002) measured the flow behind an axial fan using 2D PIV and stereoscopic PIV (SPIV) simultaneously. Because SPIV uses two cameras, perspective error does not occur. The difference in results from the two systems was proportional to the velocity in the out-of-plane direction. Reeves and Lawson (2004) demonstrated the effect of perspective error by comparing the data obtained from single- and dual-lens endoscopic PIV imaging systems. A large error can arise in single-lens endoscopic PIV because of the short focal length of the lens. Their experimental results showed that the error could reach approximately 30% of the in-plane velocity. They argued that a stereoscopic endoscope system should be used to eliminate this effect.

A study on the propagation of such errors was recently reported. Ma and Jiang (2018) assessed the propagation of perspective error in the measurement of 3D vortices. They estimated the errors in vortex-related parameters such as circulation, enstrophy, and vorticity, when perspective error existed in the measured velocity. However, this study only estimated the propagation of error and did not suggest any correction methods.

Although many previous studies have measured HIT turbulence statistics using 2D PIV, the effects of perspective error have not been considered heretofore. In HIT, because the velocity components in the three directions are comparable, they are particularly vulnerable to such error. In addition, there is a lack of insight into the extent to which the error included in the measured velocity is amplified (or damped) as it propagates to various turbulence statistics. To properly interpret the results, it is important to identify and correct this error.

In this study, we investigated the effect of perspective error and proposed a correction model that can be used for HIT. The effect of random error, which lacks direction, can be easily reduced by increasing the number of data points. However, systematic error cannot be removed this way (Taylor 1997); it can only be removed by correction. Therefore, we analyzed the effect of perspective error on various turbulence statistics, and developed a correction method. In Section 3.3.1, the perspective error model is reviewed and validated via a simple experiment. In Section 3.3.2, we mathematically calculate error propagation in isotropic turbulence statistics, and demonstrate how to correct them. Finally, in Section 3.3.3 we validate the correction method using both synthetic turbulence and wind tunnel experiments.

3.3.1. Bias error due to out-of-plane motion

3.3.1.1. Perspective error model

The effect of perspective error on the measured in-plane velocity field has been discussed in previous studies (Lecordier and Westerweel 2004; Ma and Jiang 2018). In this section, we provide detailed derivation of this perspective error which occurs in 2D PIV, using the configuration of the camera imaging system. Fig. 3-17 shows a schematic of a camera imaging a particle. In this particular figure, the particle in the physical domain moves only in the out-of-plane direction (*Z*-direction), but the camera records an *x*-direction displacement. When the actual particle position changes from X_{p1} to X_{p2} during Δt, the *X*-direction velocity in the physical domain is

$$U_r = \frac{X_{p_2} - X_{p_1}}{\Delta t} = 0 \tag{3-25}$$

where the subscript *r* indicates the real (or true) value. Because there is no particle movement in the *X*-direction, U_r is zero. Similarly, the measured velocity, U_m, obtained from the particle images, can be expressed as Eq. (3-26):

$$U_m = \frac{1}{M_o}\frac{x_{p_2} - x_{p_1}}{\Delta t} \neq 0 \tag{3-26}$$

where the magnification factor M_o is defined as d_i/d_o (ratio between image plane distance and object plane distance), and the subscript *m* represents the measured value. The perspective error is the difference in velocities U_m and U_r. Using the geometric relation obtained from Fig. 3-17:

$$\tan(\alpha_1) = \frac{X_{p_1}}{d_o - Z_{p_1}} = \frac{x_{p_1}}{d_i} \tag{3-27}$$

$$\tan(\alpha_2) = \frac{X_{p_2}}{d_o - Z_{p_2}} = \frac{x_{p_2}}{d_i} \tag{3-28}$$

By substituting these two equations into Eq. (3-26) and using Eq. (3-25) and $Z_{p2} = Z_{p1} + W_r \Delta t$ (where W_r is the Z-direction velocity), we can obtain the relation between U_r and U_m in Eq. (3-29).

$$U_m = \frac{d_o}{d_o - Z_{p_2}} U_r + \frac{X_{p_1} W_r d_o}{(d_o - Z_{p_1})(d_o - Z_{p_2})} \tag{3-29}$$

By using Eq. (3-27), Eq. (3-29) can be written as:

$$U_m = \frac{d_o}{d_o - Z_{p_2}} U_r + \frac{d_o x_{p_1} W_r}{(d_o - Z_{p_2}) d_i} \tag{3-30}$$

The distance from the lens to the laser sheet (d_o) is O (10^2 – 10^3 mm) for PIV. Z_{p2} is the distance from the center of the laser sheet to the particle in the thickness direction, which is O (10^{-1} mm). Based on the fact that $d_o >> Z_{p2}$, we obtain Eq. (3-31) from Eq. (3-30):

$$U_m \approx U_r + \frac{x_{p_1}}{d_i} W_r \tag{3-31}$$

In this equation, the initial position of the particle can be approximated by the coordinates of each interrogation window ($x_{p1} \approx x$). This can be done for the Y-direction in a similar fashion, and Eq. (3-32) is finally obtained:

$$\begin{aligned} U_m &\approx U_r + \frac{x}{d_i} W_r = U_r + \alpha(x) W_r \\ V_m &\approx V_r + \frac{y}{d_i} W_r = V_r + \beta(y) W_r \end{aligned} \tag{3-32}$$

These relationships are consistent with the models presented in previous studies (Lecordier and Westerweel 2004; Raffel et al. 2018). The perspective error is the second term on the right-hand side of the two expressions in Eq. (3-32). They are proportional to W_r and the relative position of the particle from the sensor center, and inversely proportional to the image plane distance (d_i).

To estimate the effect of perspective error in experimental conditions, Fig. 3-18 shows the distribution of this error for three types of cameras with different spatial resolution and pixel pitch, calculated using Eq. (3-32). The contour shows the magnitude of the perspective error in terms of displacement. Similar trends can be observed in all cases, wherein the error at the center is zero and increases toward the edge. In addition, the error increases as the physical size of the sensor increases. In particular, it can be seen that a maximum error of 0.7 px occurs in the case of the largest sensor. Considering that the displacement uncertainty caused by random

errors in PIV is approximately 0.1 px (Wieneke 2015), this bias error is approximately seven times larger for this sensor.

3.3.1.2. Validation of perspective error model

To validate the perspective error model equation, Eq. (3-32), we conducted an experiment as depicted in Fig. 3-19 (a). The target plate was marked with dots in a 250 μm interval grid pattern. We measured the in-plane displacement of the dots while moving the target in the normal direction (*Z*-direction) of the camera. Precise alignment is required to make the target move only in the *Z*-direction. Otherwise, the zero-error point may be biased to one side or the error field may not be symmetric, as shown in Fig. 3-19 (b). The camera we used had 2048 × 2048 px^2 spatial resolution with a sensor size of 7.4 μm/px, and a Nikon 105 mm macro lens was installed. In this experiment, M_o was approximately 0.75, and the distance from the subject to the sensor ($d_o + d_i$) was 334 mm. These conditions are typical for 2D PIV experiments.

Fig. 3-20 (a) shows a zoomed-in camera image of a subsection of the target moving out of plane in the *Z*-direction, and the resulting in-plane displacement vectors. We fit circles to the dots using the Hough transform based algorithm 'imfindcircles' within MATLAB. The in-plane displacement was calculated from the difference of the center values of the circle, obtained with sub-pixel resolution from the fitting results. By using all dots on the entire target, we can obtain the vector field of the entire image, which is illustrated in the left of Fig. 3-20 (b). Similar to Fig. 3-18, the error is small at the center of the image and increases toward the edge. The right side of Fig. 3-20 (b) shows the calculated result obtained by substituting the experimental conditions into Eq. (3-32). Compared with the experimental results, the size and direction of the vectors are similar.

For further analysis, the *x*-direction displacement field obtained in Fig. 3-20 (b) was averaged in the *y*-direction, as shown in Fig. 3-21. The circles, triangles, and squares indicate the experimental data for ΔZ = 1, 2, and 3 mm, respectively, and the lines represent the corresponding results of the model. It should be noted that the Z-direction displacement is somewhat large compared to the nominal laser thickness used in PIV. Nevertheless, these cases were selected to demonstrate the validity of the model. Error bars representing experimental uncertainty at 95% confidence interval is small compared to the size of the symbols, and is not drawn in the figure. The difference between the slope obtained by linear regression of the experimental values and that from the model was similar in the three cases, and the average is

6.8%. Because the error is similar in all cases, it is assumed that this error is due to the measurement error of d_i, which is calculated by combining the magnification (d_i/d_o) and distance from the sensor to the object plane ($d_i + d_o$). If each measurement value contains an error of 3 - 4%, this level of error may occur. In addition to this, lens aberrations and assumptions made when deriving the model (i.e. $d_o >> Z_{p2}$) may also cause a difference between the theoretical and experimental values. Nevertheless, fairly good agreement is observed between the model and experimental data for the three different out-of-plane displacements. Thus, it is confirmed that equation Eq. (3-32) is an appropriate physical model for predicting perspective error.

3.3.2. Error propagation and correction model

In this section, we calculate how the perspective error obtained in Section 3.3.1 is propagated to various turbulence statistics. We consider turbulence kinetic energy (TKE), dissipation rate, and two-point statistics, which are frequently calculated in HIT studies. Methods for correcting the error in the statistics using propagation equations are also presented.

3.3.2.1. Fluctuation velocity

All turbulence statistics were calculated based on the fluctuation velocity. The measured fluctuation velocity can be obtained from the Reynolds decomposition of Eq. (3-32):

$$u_m = U_m - \bar{U}_m = U_r + \alpha(x)W_r - \overline{U_r + \alpha(x)W_r} \tag{3-33}$$

where overbar denotes the ensemble average operator. U and u are the total and fluctuation velocities, respectively. Applying the Reynolds decomposition to U_r and W_r in Eq. (3-33) yields the following equation:

$$u_m(x, y) = u_r(x, y) + \alpha(x)w_r(x, y) \tag{3-34}$$

It has the same form as Eq. (3-32), with the difference that the total velocity is replaced by the fluctuation velocity. The y-direction velocity is similarly calculated by simply changing u and α in Eq. (3-34) to v and β, respectively.

3.3.2.2. Turbulence kinetic energy

TKE is a basic quantity in turbulence analysis and is defined by Eq. (3-35):

$$k_r \equiv \frac{1}{2}\overline{u_r^2 + v_r^2 + w_r^2} \approx \frac{3}{4}\overline{u_r^2 + v_r^2} \tag{3-35}$$

The approximation above is valid under isotropic conditions, and in this case, it can be calculated using the 2D velocity components. To express the true TKE (k_r) in terms of the measured velocity, which includes the perspective error, we substitute Eq. (3-34) into Eq. (3-35).

$$k_r^m = \frac{1}{2}\,\overline{u_m^2 + v_m^2 - 2\alpha u_r w_r - 2\beta v_r w_r - [\alpha^2 + \beta^2 - 1]\, w_r^2} \tag{3-36}$$

Here, k_r^m is the actual TKE obtained from the measured velocity. If the flow is isotropic, the Reynolds stress tensor has only diagonal components, and they are all equal to each other. This implies that the following two equations are satisfied.

$$\begin{cases} \overline{u_i v_i} = 0 \quad (i \neq j) \\ \overline{u_r^2} = \overline{v_r^2} = \overline{w_r^2} = \dfrac{2}{3}k_r \end{cases} \tag{3-37}$$

Using these facts, the 3rd and 4th terms on the right-hand side of Eq. (3-36) become zero, and the last term can be expressed in terms of k_r. Thus, we obtain the following final equation:

$$k_r^m(x,y) = \frac{3}{2\,[\alpha(x)^2 + \beta(y)^2 + 2]}\,\overline{u_m^2(x,y) + v_m^2(x,y)} \tag{3-38}$$

However, many previous HIT studies have used the following equation without considering perspective error (Hwang and Eaton 2004; Goepfert et al. 2010; Bellani and Variano 2014; Dou et al. 2016; Han et al. 2020):

$$k_m(x,y) = \frac{3}{4}\,\overline{u_m^2(x,y) + v_m^2(x,y)} \tag{3-39}$$

The comparison of Eqs. (3-38) and (3-39) shows a difference in the coefficient. In Eq. (3-38), α and β are both zero at the center of the image; hence, the two equations are the same. However, toward the edge of the image, the difference between these two quantities is no longer negligible and $k_r^m < k_m$. That is, the TKE will be overestimated if perspective error is not considered.

To assess the effect of systematic perspective error on TKE, we compared it with the random error. The systematic (or bias) error ratio can first be calculated as follows:

$$\frac{\Delta k}{k} = \frac{|k_m - k_r^m|}{k_r^m} = \frac{1}{2}(\alpha^2 + \beta^2) \tag{3-40}$$

The random error can be calculated using the uncertainty of each component constituting the TKE and the Taylor series method (Coleman and Steele 2018). Based on the study by Benedict and Gould (1996), Sciacchitano and Wieneke (2016) calculated the uncertainty of the TKE as follows:

$$\delta k = \sqrt{\overline{u^2}^2 + \overline{v^2}^2 + \overline{w^2}^2}\sqrt{\frac{1}{2N}} \approx \overline{u^2}\sqrt{\frac{3}{2N}} \tag{3-41}$$

where N is the number of samples used for ensemble averaging. In isotropic turbulence, Eq. (3-37) yields the approximation in Eq. (3-41). Based on this equation, the relative uncertainty for random error can be calculated as follows:

$$\frac{\delta k}{k} = \sqrt{\frac{2}{3N}} \tag{3-42}$$

Fig. 3-22 shows the results of the calculation of Eqs. (3-40) and (3-42). In the case of Eq. (3-40), the calculation is performed under the condition $\alpha = \beta$. The random error was approximately 8% when the number of ensembles was 10^2, and dropped to less than 1% when it increased up to 10^4. It is generally set to $N \sim O$ (10^2 – 10^3) in PIV studies, and can be considered to be approximately 2 – 8%. The perspective error is proportional to the squared α (or β). When $\alpha = \beta = 0.1$, the systematic error is comparable to the random error that occurs at $N = 10^4$, and when it becomes 0.3 or more, the error exceeds that at $N = 10^2$. It should be noted that even if the perspective error is smaller than the random error, it should be corrected using Eq. (3-38) because it is a systematic error.

3.3.2.3. TKE dissipation rate

The TKE dissipation rate is an important parameter used for turbulence modeling. It is defined as follows, under the isotropic assumption:

$$\varepsilon_r = 15\nu\overline{\left(\frac{\partial u_r}{\partial x}\right)^2} = 15\nu\overline{\left(\frac{\partial v_r}{\partial y}\right)^2} = 15\nu\overline{\frac{1}{2}\left[\left(\frac{\partial u_r}{\partial x}\right)^2 + \left(\frac{\partial v_r}{\partial y}\right)^2\right]} \tag{3-43}$$

where ν is the kinematic viscosity. To reveal the relationship between ε_r and the measured velocity, Eq. (3-34) is substituted into Eq. (3-43).

$$\varepsilon_r^m = 15\nu\overline{\left(\frac{\partial u_r}{\partial x}\right)^2} = 15\nu\left[\begin{array}{c}\overline{\left(\frac{\partial u_m}{\partial x}\right)^2} - \overline{\left(\frac{d\alpha}{dx}w_r\right)^2} - \overline{\left(\alpha\frac{\partial w_r}{\partial x}\right)^2} \\ -2\overline{w_r\alpha\frac{d\alpha}{dx}\frac{\partial w_r}{\partial x}} - 2\overline{w_r\frac{d\alpha}{dx}\frac{\partial u_r}{\partial x}} - 2\alpha\overline{\frac{\partial w_r}{\partial x}\frac{\partial u_r}{\partial x}}\end{array}\right] \quad (3\text{-}44)$$

The terms on the right-hand side of Eq. (3-44) can be simplified in isotropic turbulence. Using Eq. (3-37), the second term on the right-hand side can be expressed as

$$-\overline{\left(\frac{d\alpha}{dx}w_r\right)^2} = -\left(\frac{d\alpha}{dx}\right)^2\overline{w_r^2} = -\frac{1}{d_i^2}\frac{2}{3}k_r \quad (3\text{-}45)$$

By using Eq. (3-46) below, the 3rd and 6th terms in Eq. (3-44) can be expressed as Eq. (3-47) (Eq. 5.168 – 169 in Pope (2000)).

$$\overline{\frac{\partial u_i}{\partial x_j}\frac{\partial u_k}{\partial x_l}} = \gamma\left(\delta_{ik}\delta_{jl} - \frac{1}{4}\delta_{ij}\delta_{kl} - \frac{1}{4}\delta_{il}\delta_{jk}\right) \quad (3\text{-}46)$$

$$\begin{cases} -\overline{\left(\alpha\frac{\partial w_r}{\partial x}\right)^2} = -2\alpha^2\overline{\left(\frac{\partial u_r}{\partial x}\right)^2} \\ -2\alpha\overline{\frac{\partial w_r}{\partial x}\frac{\partial u_r}{\partial x}} = 0 \end{cases} \quad (3\text{-}47)$$

In Eq. (3-46), δ denotes the Kronecker delta, and γ is a scalar. Finally, the 4th and 5th terms in Eq. (3-44) are transformed as follows:

$$\begin{cases} -2\overline{w_r\alpha\frac{d\alpha}{dx}\frac{\partial w_r}{\partial x}} = -\frac{\alpha}{d_i}\frac{\partial\overline{w_r^2}}{\partial x} = 0 \\ -2\overline{w_r\frac{d\alpha}{dx}\frac{\partial u_r}{\partial x}} = -\frac{2}{d_i}\overline{w_r\frac{\partial u_r}{\partial x}} = \ldots \\ = \frac{2}{d_i}\left(\overline{w_r\frac{\partial v_r}{\partial y} + w_r\frac{\partial w_r}{\partial z}}\right) = \frac{2}{d_i}\left(\overline{w_r\frac{\partial u_r}{\partial x} + \frac{1}{2}\frac{\partial w_r^2}{\partial z}}\right) = 0 \end{cases} \quad (3\text{-}48)$$

It should be noted that $\overline{w_r(\partial v_r/\partial y)} = \overline{w_r(\partial u_r\partial x)}$ assuming isotropy. Combining the 2nd and 4th terms in Eq. (3-48), and assuming homogeneity such that $\overline{\partial w_r^2/\partial z} = 0$, $\overline{w_r\partial u_r/\partial x}$ also becomes 0. By substituting Eqs. (3-45) – (3-48) into Eq. (3-44), the dissipation rate can be estimated for $\partial u_r/\partial x$. The same derivation can be applied to $\partial v_r/\partial y$. In this study, the dissipation rate was calculated using the last definition of Eq. (3-43).

$$\varepsilon_r^m(x,y) = 15\nu\,\overline{\frac{1}{2}\left[\left(\frac{\partial u_r}{\partial x}\right)^2 + \left(\frac{\partial v_r}{\partial y}\right)^2\right]}$$
$$= \frac{15\nu}{2}\left[\begin{array}{c}\frac{1}{1+2\alpha^2}\left(\overline{\left(\frac{\partial u_m}{\partial x}\right)^2} - \frac{1}{d_i^2}\frac{2}{3}k_r\right) + \\ \frac{1}{1+2\beta^2}\left(\overline{\left(\frac{\partial v_m}{\partial y}\right)^2} - \frac{1}{d_i^2}\frac{2}{3}k_r\right)\end{array}\right] \tag{3-49}$$

Equation (3-49) contains the true value of the TKE, which can be obtained using Eq. (3-38).

3.3.2.4. Two-point statistics

Two-point statistics can provide useful information about the energy cascade of turbulence (Pope 2000). The velocity correlation tensor represents the correlation between the velocity fluctuation at two points separated by the vector ***r***. If the turbulence is homogeneous, it becomes a function of ***r***, regardless of the position in space.

$$R_{ij,r}(\boldsymbol{r}) = \overline{u_i(\boldsymbol{x}+\boldsymbol{r})u_j(\boldsymbol{x})} \tag{3-50}$$

If ***r*** and the direction of velocity are aligned, the correlation is longitudinal; otherwise, it is transverse. First, the expression for the longitudinal correlation in the *x*-direction can be derived using Eq. (3-34):

$$\begin{aligned} R_{11,r}^m(r_1) &= \overline{u_r(x+r_1)u_r(x)} = \overline{u_r^+ u_r} \\ &= \overline{u_m^+ u_m} - \alpha\overline{w_r u_r^+} - \alpha^+\overline{w_r^+ u_r} - \alpha\alpha^+\overline{w_r w_r^+} \end{aligned} \tag{3-51}$$

The subscript *r* denotes the real (i.e. true) value, and r_1 denotes the separation in the *x*-direction. To simplify the equation, the quantity at $x + r_1$ is denoted by the superscript +. In isotropic turbulence, $R_{ij} = 0$ for $i \neq j$ and thus the 2nd and 3rd terms on the right-hand side can be eliminated. Additionally, since $R_{33} = R_{22}$, Eq. (3-51) can be written as follows:

$$R_{11,r}^m(r_1) = \overline{u_m u_m^+} - \alpha\alpha^+\overline{w_r w_r^+} = \overline{u_m u_m^+} - \alpha\alpha^+ R_{22,r} \tag{3-52}$$

The transverse correlation (in the *x*-direction) can be calculated similarly:

$$R_{22,r}^m(r_1) = \overline{v_m v_m^+} - \beta\beta^+\overline{w_r w_r^+} = \overline{v_m v_m^+} - \beta\beta^+ R_{22,r} \tag{3-53}$$

β is only a function of *y* and so $\beta = \beta^+$. Thus, the final expression is

$$R_{22,r}^{m}(r_1) = \frac{\overline{v_m v_m^+}}{1+\beta^2} \tag{3-54}$$

The structure function is another two-point statistic and an important parameter related to the Kolmogorov equation and 4/5 law (Kolmogorov 1991). It is defined as the covariance of the velocity difference between two points separated by ***r***. Error propagation of the 2nd order structure function is similar to that for the velocity correlation; hence, it is not repeated here, and only the results are shown below.

$$D_{LL,r}^{m}(r_1) = \overline{[u_m^+ - u_m]^2} - \frac{2k_r}{3}\left(\alpha^{+^2} + \alpha^2\right) + 2\alpha\alpha^+ R_{22,r}(r_1) \tag{3-55}$$

$$D_{NN,r}^{m}(r_1) = \overline{[v_m^+ - v_m]^2} - 2\beta^2\left(\frac{2k_r}{3} - R_{22,r}(r_1)\right) \tag{3-56}$$

The calculation of the longitudinal (D_{LL}) and transverse (D_{NN}) structure functions considering the perspective error includes the transverse velocity correlation and TKE. If these are replaced with Eqs. (3-53) and (3-38), respectively, the calculation can be performed using only the measured velocities u_m and v_m.

3.3.3. Validation of error correction model

In this section, the theoretical equations calculated in the previous section are verified using isotropic turbulence data. Xu and Chen (2013) used direct numerical simulation (DNS) data reported by Li et al. (2008) to conduct a study on accurate dissipation rate measurement using PIV in isotropic turbulence. Although DNS reflects the complete flow physics, the total simulation time is only approximately five times the integral time scale, which prevents the use of the ensemble operator applied in conventional PIV experiments. Therefore, we used synthetic turbulence in this study. A synthetic turbulence generator can create a 3D flow field by expressing the velocity field as a Fourier series of random amplitudes and wavenumbers. If new random seeds are used for every iteration, independent velocity vector fields can be generated, which is similar to the data obtained from conventional PIV.

3.3.3.1. Verification using synthetic isotropic turbulence

We created velocity fields using a synthetic turbulence generator developed by the University of Utah (Saad and Sutherland 2016; Saad et al. 2017; Richards et al. 2018). The detailed procedure is not provided here, as it can be found in the

abovementioned studies. The von Kármán – Pao spectrum shown in Fig. 3-23 was used for the data generation, and the parameters were set as $\xi = 1.45$, $L_e = 0.75/\kappa_e$, $u_{\mathrm{rms}} = 0.25$, $\kappa_e = 40\times(5/12)^{1/2}$, $\nu = 10^{-5}$, and $\kappa_\eta = (u_{\mathrm{rms}}^3/L_e)^{1/4}\nu^{-3/4}$ in reference to previous studies (Saad et al. 2017). Here, ξ, L_e, u_{rms}, ν, and κ_η are scaling constant, integral length scale, rms velocity, kinematic viscosity, and Kolmogorov wavenumber, respectively. κ_e is the wavenumber related to the maximum energy of the spectrum. The generated data represent a 2D slice of the velocity field with grid resolution of 128^2 and box size of $L = 0.2$. The corresponding resolved wavenumber region (comprised of 5,000 modes) within the spectrum is depicted by the red solid line in Fig. 3-23. One thousand flow fields were generated for accurate calculation of the turbulence statistics.

An example of the generated vector field is shown in Fig. 3-24 (a). A random yet coherent flow structure can be observed, similar to the instantaneous velocity fields of previous studies on HIT (Hwang and Eaton 2004; Bellani and Variano 2014; Hoffman and Eaton 2021). Isotropy was first confirmed by examining the velocity statistics in each direction. Fig. 3-24 (b) shows the velocity PDF for each component for all datasets. It can be seen that all components exactly match the Gaussian profile indicated by the solid line. The mean of the three velocity components was also close to zero. Thus, the generated synthetic data resembles isotropic turbulence without a mean flow.

It should be noted that previous studies have added synthetic particles to known flow fields to analyze PIV error and uncertainty (Lee and Hwang 2019; Oh et al. 2021). However, this method includes random errors that occur during PIV analysis, and thus it is difficult to isolate and analyze only the perspective bias error effect. Since flow fields with particles are not needed for this study, we did not use this method.

Utilizing the synthetic turbulence flow field, Eq. (3-34) was applied to superimpose a perspective error on the velocity. To simulate various experimental conditions, five cases of S^*, defined as α_{max} (or β_{max}, which is set to be the same), ranging from 0.05 to 0.7 were simulated. A large S^* suggests that the sensor has a large physical size or the image plane distance is small. Table 3-3 summarizes the simulation conditions of the synthetic turbulence described in this section.

Fig. 3-25 illustrates TKE results calculated using Eqs. (3-34), (3-38), and (3-39) with the original real data u_r and v_r, and the erroneous measured data u_m and v_m. The contours show TKE normalized by the spatially averaged TKE value without error

($\langle k_r \rangle$). In Fig. 3-25 (a), it can be seen that the reference real case values are distributed between approximately 0.9 – 1.1, demonstrating that the turbulence is spatially homogeneous. Fig. 3-25 (b) and (c) depict cases of perspective error propagation for TKE. As expected, near the center of the measurement field, k_m has almost the same value as k_r, with no error; however, the difference gradually increases toward the edge of the image due to the error. The case depicted in Fig. 3-25 (c) with a high S^* shows a larger error than that in Fig. 3-25 (b). The corrected results calculated using Eq. (3-38) for the case of $S^* = 0.7$ is shown in Fig. 3-25 (d). When compared with Fig. 3-25 (c), it can be seen that the errors at the edge are noticeably improved. In addition, compared with Fig. 3-25 (a), the overall turbulence distribution is fairly similar.

For a more detailed analysis, the normalized TKE along the x-direction from the center of the image (see the black dotted line in Fig. 3-25a) is plotted in Fig. 3-26. In case 2, a negligible bias error of less than 1% occurred, compared to the baseline case depicted by the red circles. However, in case 5, an error of up to 27% occurred at the edge of the image. Equations (3-38) and (3-39) were used to predict the error trend with respect to S^* and α/S^*. Using these two equations, we obtain the following relationship:

$$k_m = \frac{\alpha^2 + \beta^2 + 2}{2} k_r^m = \left(\frac{\alpha^2}{2} + 1\right) k_r^m = \left[\frac{S^{*2}}{2}\left(\frac{\alpha}{S^*}\right)^2 + 1\right] k_r^m \qquad (3\text{-}57)$$

where $\beta = 0$ along the horizontal center line. The above equation can be expressed in the following form:

$$k_m / \langle k_r \rangle = \left[\frac{S^{*2}}{2}\left(\frac{\alpha}{S^*}\right)^2 + 1\right] \frac{k_r^m}{\langle k_r \rangle} \approx \frac{S^{*2}}{2}\left(\frac{\alpha}{S^*}\right)^2 + 1 \qquad (3\text{-}58)$$

k_r^m and k_r are similar, and in homogeneous turbulence they have small spatial variation, which allows the approximation in Eq. (3-58). The equation is plotted as lines without symbols in Fig. 3-26. It can be seen that the theoretical results calculated with this equation have a similar trend as that obtained by the simulation. The reason for the slight difference is that the data were not completely homogeneous.

For additional quantitative analysis, we plotted the relative frequency distribution (RFD) of all TKE data. Fig. 3-27 shows the RFD of the normalized k_m and k_r^m. The red dotted line in Fig. 3-27 (a) represents the reference data without error. Since the turbulence is homogeneous, the distribution is Gaussian with a mean

of 1. As can be seen in Fig. 3-25 and Fig. 3-26, the perspective error causes overestimation of the TKE. Hence, the distribution will be skewed to the right as the error increases. Fig. 3-27 (b) shows the results of the corrected k_r^m, which agree well with the data of k_r for all cases. Although the peak is not completely restored in cases 4 and 5 which have large error, the difference in the moments of the distribution (e.g., standard deviation and kurtosis) is less than 5%.

The spatial average of the TKE field obtained via PIV in homogeneous turbulence is often used as a representative value. The effect of the error on the spatially averaged TKE value was analyzed. Fig. 3-28 shows the changes in $\langle k_m \rangle$ and $\langle k_r^m \rangle$ with respect to S^*. Cases 1 and 2 show a small difference of less than 1% from the reference data; however, as S^* increases, the difference increases sharply, up to approximately 16%. The error in the spatially averaged TKE can be calculated using the following equation:

$$\frac{\langle k_m \rangle}{\langle k_r \rangle} = \frac{\int_{-y_s}^{y_s} \int_{-x_s}^{x_s} \frac{k_r^m}{2} \left(\alpha^2 + \beta^2 + 2\right) dxdy}{\langle k_r \rangle \int_{-y_s}^{y_s} \int_{-x_s}^{x_s} dxdy} \approx \frac{S^{*2}}{3} + 1 \tag{3-59}$$

The result of this equation is represented as a black dotted line in Fig. 3-28. The error predicted with the equation shows good agreement with the TKE error obtained from the simulation. Accurate prediction of this bias error makes it possible to properly correct it. In Fig. 3-28, the circles represent the case of using the correction equation, and it can be seen that it is essentially the same as the real value.

Next, we similarly analyzed the TKE dissipation rate. Fig. 3-29 shows the spatially averaged dissipation rate with respect to S^*. The dissipation rate is more sensitive to the effect of perspective error than TKE, and the error reaches 25% when $S^* = 0.7$. To calculate the difference between the reference real case, we rearranged the equation for the dissipation rate in a similar way as in Eq. (3-59).

$$\frac{\langle \varepsilon_m \rangle}{\langle \varepsilon_r \rangle} = \frac{\int_{-y_s}^{y_s} \int_{-x_s}^{x_s} \frac{\left(1+2\alpha^2\right)+\left(1+2\beta^2\right)}{2} \left(\varepsilon_r^m + \frac{10 k_r \nu}{d_i^2}\right) dxdy}{\langle \varepsilon_r \rangle \int_{-y_s}^{y_s} \int_{-x_s}^{x_s} dxdy} \approx \frac{2S^{*2}}{3} + 1 \tag{3-60}$$

Compared with Eq. (3-59), the coefficient of S^{*2} is twice as large. Therefore, the dissipation rate shows a larger error than that of the TKE. However, Eq. (3-60) does not predict the error as accurately as Eq. (3-59), and shows slight differences as can be seen in Fig. 3-29. This is because the assumptions (for example, Eqs. (3-45) – (3-48)) for calculating ε_r^m are not perfect. In the case of TKE, isotropy of the velocity statistics is a sufficient condition, but in the case of dissipation, the 4th order tensor related to the velocity gradient must satisfy the isotropy assumption. Hence,

the correction shown in Fig. 3-29 is not as good compared with that of the TKE. However, the difference between ε_r^m and ε_r is smaller than the overestimation caused by the perspective error. Therefore, the correction is still meaningful when calculating the dissipation rate.

Velocity correlation results are shown in Fig. 3-30, utilizing correlation coefficients normalized to the value at $r = 0$. In the case of TKE or dissipation rate, the perspective error overestimates the calculated value. However, in the case of the longitudinal correlation coefficient in Fig. 3-30 (a), the results are fairly similar, with slight underestimation. The correction reproduces the right correlation. The transverse correlation coefficient in Fig. 3-30 (b) shows no effect of the error. This is because the error effect on the transverse correlation is a function of only y (see Eq. (3-54)), whereas the vector $\boldsymbol{r}$ is parallel to the x-direction.

The velocity correlation is frequently used to obtain the integral length scale (L_{11}). Integrating the longitudinal velocity correlation from zero to infinity yields L_{11}, as follows:

$$L_{11} = \int_0^\infty R_{11}(r)/R_{11}(0)dr \tag{3-61}$$

The calculated L_{11} values are shown in Fig. 3-31. In Fig. 3-30 (a), the longitudinal velocity correlation appeared to have a small error. These differences generate a fairly large error (up to 8%) as they accumulate in the integration process. The correction reduces the error to approximately 1%, and is therefore recommended.

Finally, the structure function was calculated. Fig. 3-32 (a) and (b) show the longitudinal and transverse structure functions, respectively. The measured value was overestimated when compared with the actual value due to the perspective error, as in the cases of the TKE and dissipation rate. In the case of $D_{LL,m}$, the difference gradually increased with r. The difference can be assessed by analyzing the magnitudes of the second and third terms on the right-hand side of Eq. (3-55). ($\alpha^2 + (\alpha^+)^2$) in the second term is always greater than or equal to $2\alpha\alpha^+$ in the third term due to inequality of arithmetic and geometric means. In addition, $2k_r/3$ in the second term exhibits small changes over the entire field, whereas $R_{22,r}$ in the third term decreases with r_1. When $r_1 = 0$, $2k_r/3 \approx R_{22,r}$; and hence, as r_1 increases, $2/3k_r > R_{22,r}$. Thus, the magnitude of the second term is always larger than that of the third term, and as r_1 increases, the difference increases further. The negative sign in the second term causes an overestimation of the measured longitudinal structure function, which is the first term on the right-hand side of Eq. (3-55). In the case of the transverse

structure function in Fig. 3-32 (b), the error increases with r_1, but becomes fairly constant at approximately $r_1 = 0.05$. This is because, in Eq. (3-56), only $R_{22,r}$ changes according to r_1. In Fig. 3-30, it can be seen that $R_{22,r}$ is relatively constant beyond $r_1 = 0.05$.

The error correction results for both D_{LL} and D_{NN} for case 5 are plotted in Fig. 3-32. As with the statistics calculated thus far, the data agreed well with the true value indicated by the red dotted line. We further verified whether the corrected data satisfy the following equation depicting the relationship between D_{LL} and D_{NN} in isotropic turbulence:

$$D_{NN} = D_{LL} + \frac{1}{2} r \frac{\partial}{\partial r} D_{LL} \tag{3-62}$$

The results are shown in Fig. 3-33. The square and diamond symbols are the results calculated by substituting $D_{LL,m}$ and $D_{LL,r}^{m}$ of case 5 into Eq. (3-62), respectively, and the circle shows $D_{NN,m}$ of case 5 for comparison. As can be seen in the figure, D_{NN} obtained from $D_{LL,r}^{m}$ is almost identical to $D_{NN,r}$. However, when the perspective error is included, the calculated D_{NN} is different from both $D_{NN,m}$ and $D_{NN,r}$. This may cause a misinterpretation if Eq. (3-62) is used to verify isotropy in an actual experiment.

The structure function can also be used to indirectly determine the dissipation rate in isotropic turbulence (De Jong et al. 2009; Xu and Chen 2013), based on Kolmogorov's hypothesis that the structure function in the inertial subrange can be expressed with just two variables—the dissipation rate and r.

$$\begin{cases} D_{LL}(r_1) = C_2 \left(\varepsilon r_1\right)^{2/3} \\ D_{NN}(r_1) = \dfrac{4}{3} C_2 \left(\varepsilon r_1\right)^{2/3} \end{cases} \quad \text{(in inertial subrange)} \tag{3-63}$$

$$\varepsilon = \frac{1}{r_1}\left(\frac{D_{LL}(r_1)}{C_2}\right)^{3/2} = \frac{1}{r_1}\left(\frac{3}{4}\frac{D_{NN}(r_1)}{C_2}\right)^{3/2} \quad \text{(in inertial subrange)} \tag{3-64}$$

where C_2 is a universal constant with a value of 2 or 2.12 (Sreenivasan 1995; Pope 2000). Fig. 3-34 (a) shows the results of Eq. (3-64) calculated using $C_2 = 2.12$. The maximum of this graph is estimated as the dissipation rate. When perspective error is included, it can be seen that ε is overestimated. In contrary, the results agree with the reference case (denoted by the red dashed line) when $D_{LL,r}^{m}$ is used for the calculation. The calculated dissipation rate is shown in Fig. 3-34 (b). The results calculated with $D_{LL,r}$ and $D_{NN,r}$ are 0.216 and 0.221, respectively, which are nearly equal. In this figure, the results calculated using $D_{NN,m}$ has smaller errors than that

calculated using $D_{LL,m}$, because the error has a smaller effect on $D_{NN,m}$, as illustrated in Fig. 3-32. The dissipation rate obtained with the corrected structure function also matches well with the reference value.

3.3.3.2. Validation using grid turbulence experiments

In this section, we examine the effect of perspective error for one of the correction equations in an actual experiment, to demonstrate the validity of the technique. Using a closed-loop wind tunnel, we generated grid turbulence. According to the classical wind tunnel experiments of Comte-Bellot and Corrsin (1966), homogeneous turbulence is observed downstream of a grid beyond 40 times the mesh size (M). They also showed that a contraction enhances the isotropy of the turbulence. Based on previous research, we used a contraction with an 8:1 ratio and defined the region of interest as 40M downstream of the grid to ensure local HIT.

Fig. 3-35 shows a schematic of the experimental setup for the validation experiment. The wind tunnel is operated at an averaged streamwise velocity of 0.7 m/s, and the size of the test section is 60 cm wide and 30 cm high. The Reynolds number based on the hydraulic diameter of the test section is thus 18,500. The turbulence was measured using a 5 W diode-pumped solid-state (DPSS) laser and a high-speed camera (Phantom v2640 with sensor size 13.5 μm/px at 2048 × 1952 px^2 resolution). The effect of the perspective error is significant when using a wide-angle lens. In this study, a 28 mm Nikon lens was used to maximize this effect, and the experiment was repeated using a 105 mm Nikon lens with overlapping fields of view (FOV) to obtain a relatively accurate reference value. We performed measurements at the center of the wind tunnel where the homogeneity and isotropy were not disturbed by the walls. Due to the limitation of laser intensity available, distortion of statistics was only observed along the y-direction from the center of the FOV. The PIV results were obtained using PIVlab, a MATLAB-based open-source software (Thielicke and Stamhuis 2014; Thielicke and Sonntag 2021). The experimental parameters and detailed conditions are summarized in Table 3-4.

Fig. 3-36 shows the normalized TKE measured using the two lenses. The TKE random errors obtained from Eq. (3-42) are 1.63 and 1.49% for the 28mm and 105mm lenses, respectively. Normalization was performed using the value obtained at the center of the field with the 28 mm lens. The x-axis represents the distance relative to the center of the domain. In this figure, the black squares and circles denote the results calculated from Eqs. (3-38) and (3-39), respectively, measured

with the 28 mm lens. In the case of k_m, it can be seen that the TKE increases significantly toward the edge of the image, which is consistent with the simulation results shown in Fig. 3-25 and Fig. 3-26. However, in the case of k_r^m, the overestimation occurring at the edge is reduced considerably with the correction, and the TKE remains fairly constant. This result is similar to that measured with the 105 mm lens, which has small error even without correction. Although the results measured with the two lenses do not agree exactly because of differences due to camera lens aberrations or other PIV errors (i.e. random error in TKE) it should be noted that the value obtained via the correction equation is much closer to the reference value. Thus, we have demonstrated (at least for TKE) that the statistical correction equations obtained in Section 3.3 can reduce the perspective error in actual experiments. It should be noted that in this experimental setup, only one representative turbulence statistic was examined due to our limitations of experimental conditions and hardware. It is expected that future studies in isotropic turbulence will be able to demonstrate feasibility of the theory for other turbulence statistics as well.

3.4. Discussion

Because HIT used in the experiment is fully three dimensional, loss-of-pair and perspective errors may occur when measuring it using 2D PIV (Lee et al. 2022). The loss-of-pair error occurs when particles existing in the first frame disappear from the second frame as they are pushed out of the laser sheet by the 3D motion. As demonstrated in Section 3.2, when a particle loses its pair, the PIV correlation signal decreases and the uncertainty or probability of an outlier increases, which can propagate to erroneous turbulence statistics (Lee and Hwang 2019). To quantify the PIV uncertainty, posterior uncertainty quantification methods, particle disparity (PD) (Sciacchitano et al. 2013), and correlation statistics (CS) (Wieneke 2015) were used. Sciacchitano et al. (2015) showed that these methods performed better than the uncertainty surface method (Timmins et al. 2012) or peak ratio method (Charonko and Vlachos 2013) in general situations.

Fig. 3-37 (a) and (b) show the probability density function (PDF) of velocity uncertainty estimated by the CS and PD methods, respectively. In cases with and without particles, the probability density function (PDF) of the velocity uncertainty estimated using PD and CS peaked at approximately 0.06 px. This value is smaller than the nominally accepted PIV random error of 0.1 px (Wieneke 2015; Raffel et al. 2018; Oh et al. 2021).

A perspective error is a systematic error that occurs when the 3D motion of the particles within the laser sheet is projected onto a 2D image. In Section 3.3, the effect of this error on the turbulence statistics in HIT was estimated. It was shown that the error increased as the ratio (S^*) between half the sensor size and the distance from the image plane to the center of the lens increased. In this HIT experiments, S^* was approximately 0.03, which corresponds to TKE and dissipation rate perspective errors of 0.03 and 0.06%, respectively, which can be considered negligible.

In addition, statistical distortion may be caused by data loss. In the case of particle-laden turbulence, data loss due to particle image separation inevitably occurs, as illustrated in Fig. 2-6 (b). Poelma et al. (2006) showed that velocity data loss of 10% could distort the turbulence power spectrum. However, in this study, the data loss was only approximately 2.0% in the case of the highest particle mass loading; hence, the distortion effect could be neglected.

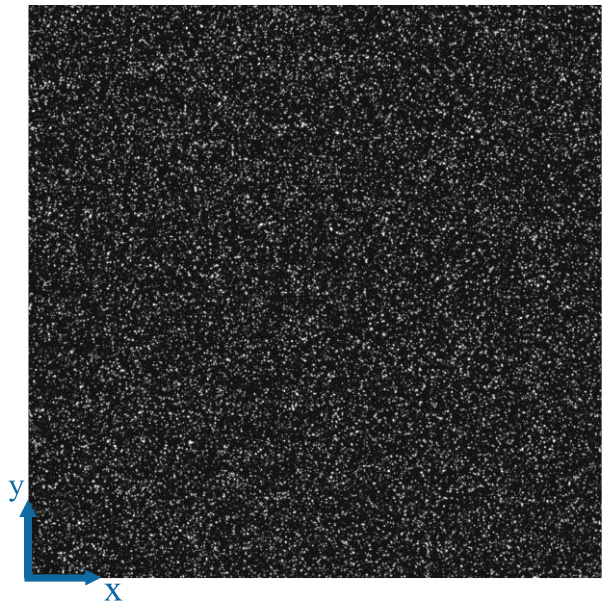

Fig. 3-1 Synthetic image sample with a random particle distribution.

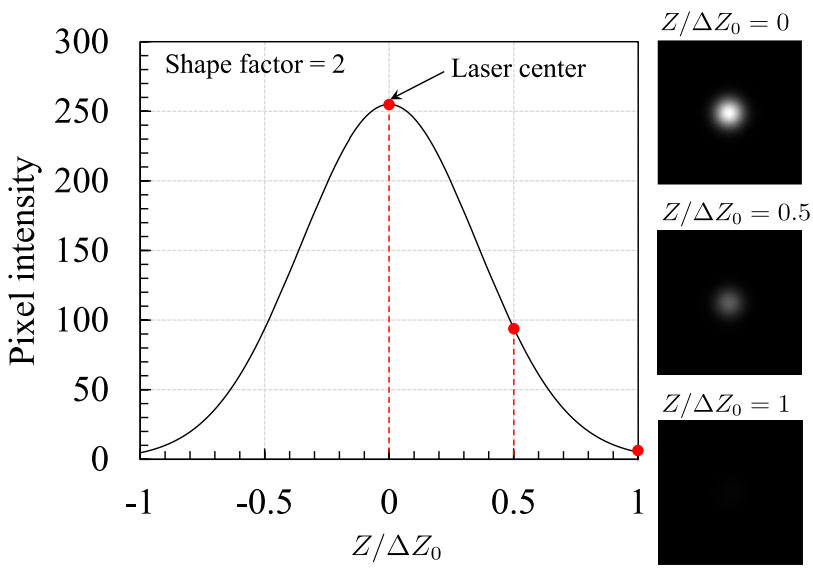

Fig. 3-2 Laser sheet intensity profile for shape factor *S* = 2, and intensity profile of a particle according to its position within the laser sheet.

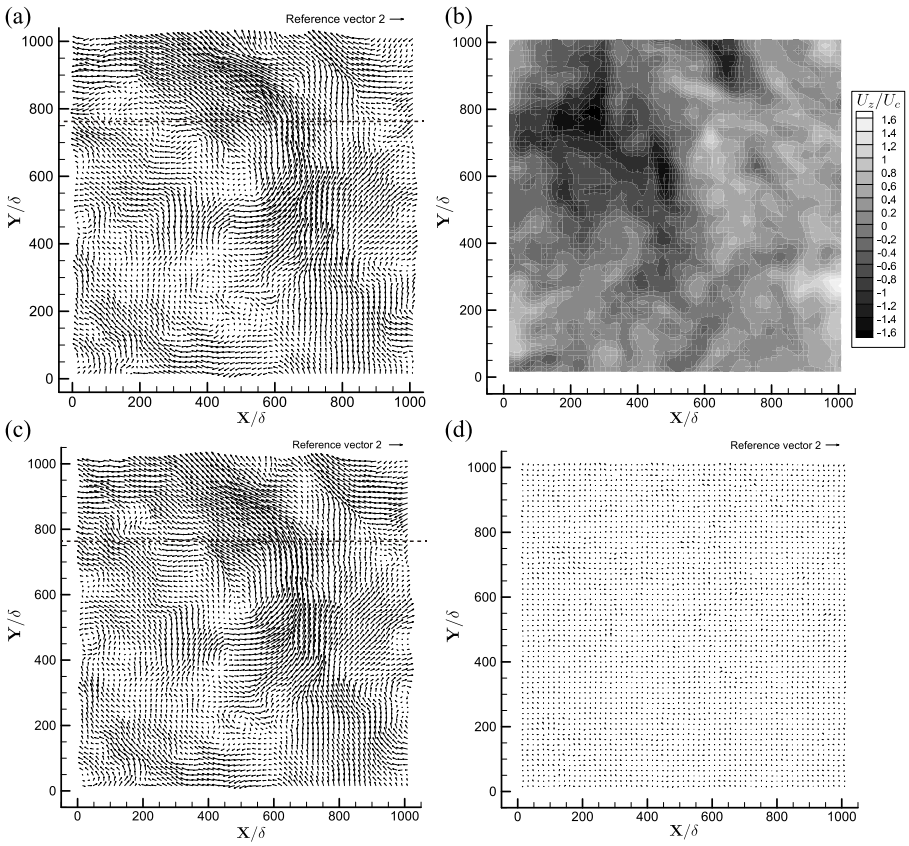

Fig. 3-3 (a) Instantaneous 2D velocity field obtained from 3D DNS, (b) normalized out-of-plane velocity from DNS, (c) PIV velocity field, (d) difference between PIV and DNS.

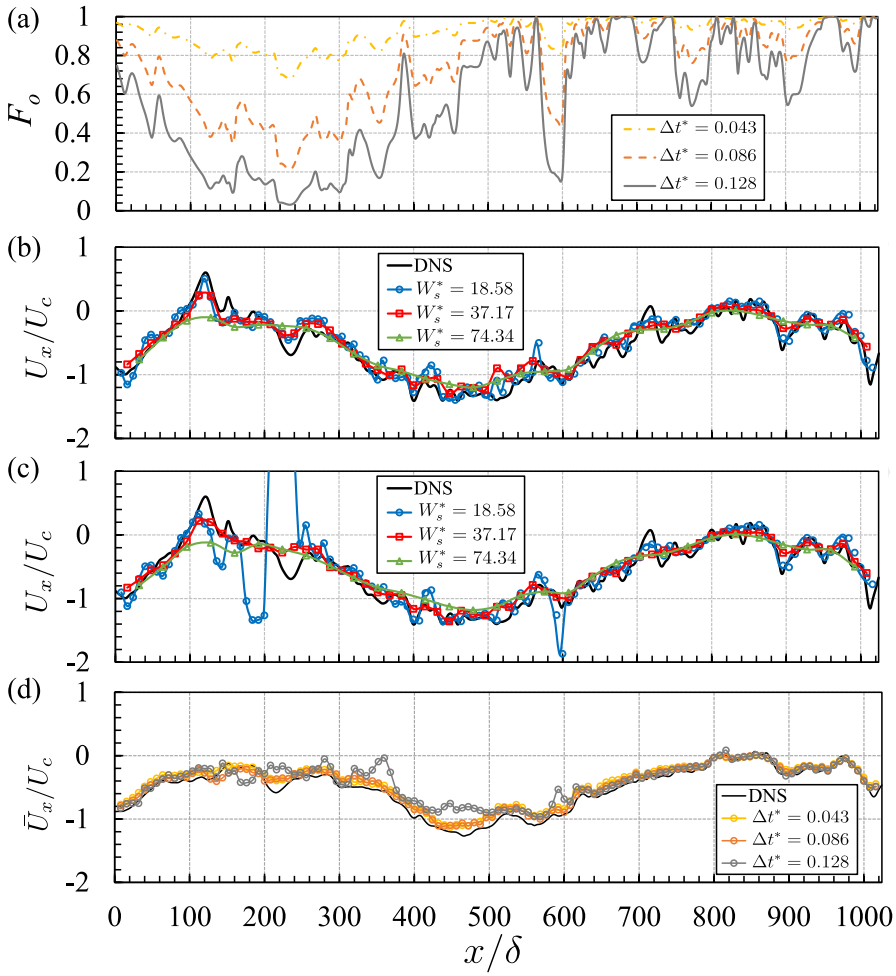

Fig. 3-4 (a) F_o along a horizontal line for three interframe time cases. (b) Instantaneous x-direction velocity along this line for various interrogation window sizes (W_s^*) with small camera inter-frame time ($\Delta t^* = 0.043$) and (c) larger camera inter-frame time ($\Delta t^* = 0.086$). (d) Time averaged x-direction velocity for various interframe time (Δt^*) for $W_s^* = 18.58$.

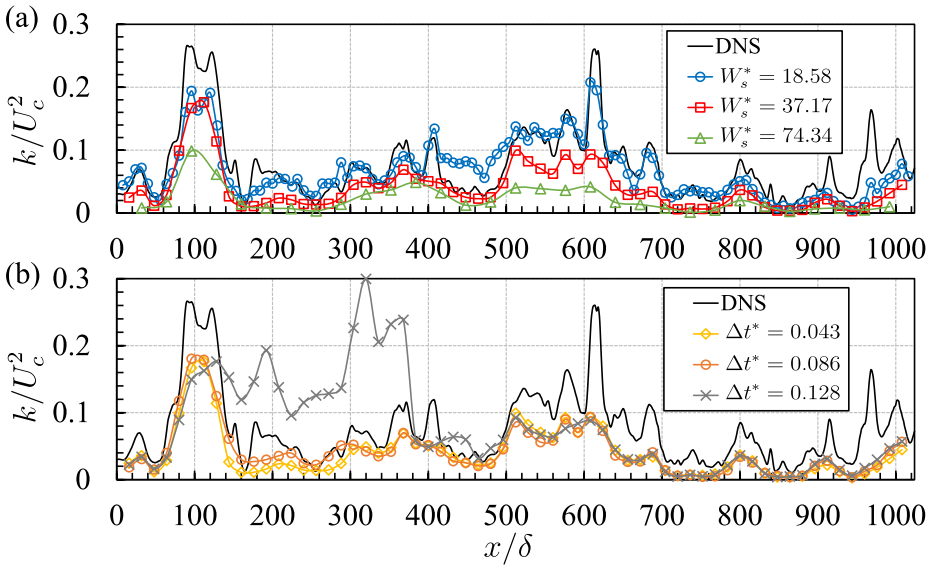

Fig. 3-5 (a) Normalized turbulence kinetic energy (TKE) as a function of IW size along the horizontal line in Fig. 3-3, (b) TKE for various camera interframe time along this line for normalized interrogation window size (W_s^*) of 37.17.

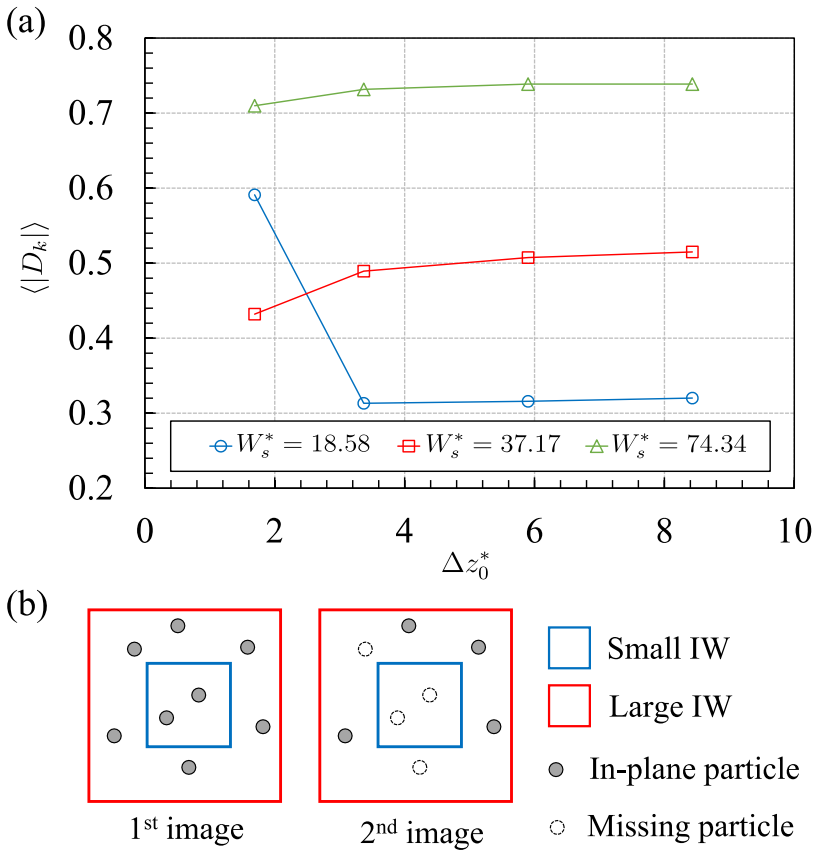

Fig. 3-6 (a) Variation of spatially averaged TKE error with laser sheet thickness for three W_s (b) effect of W_s on out-of-plane motion error.

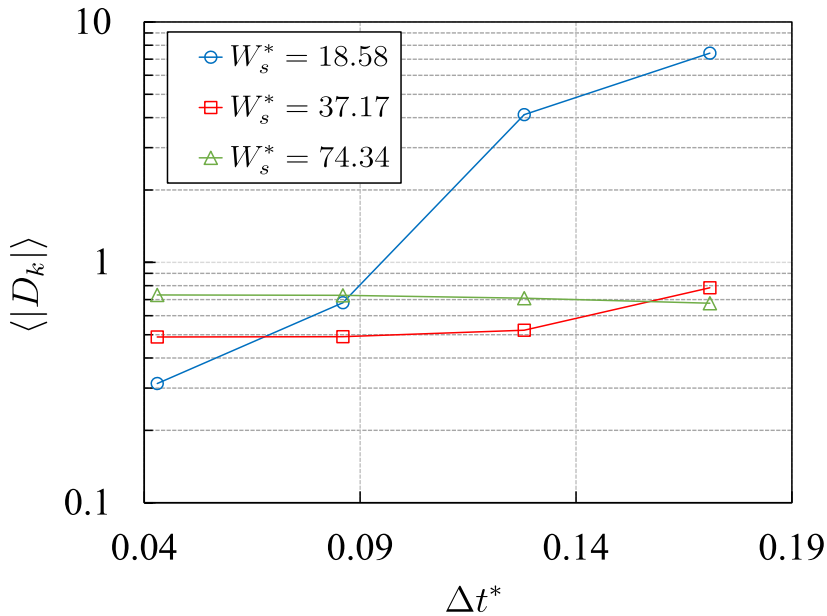

Fig. 3-7 Spatial average of TKE error for camera interframe time and W_s.

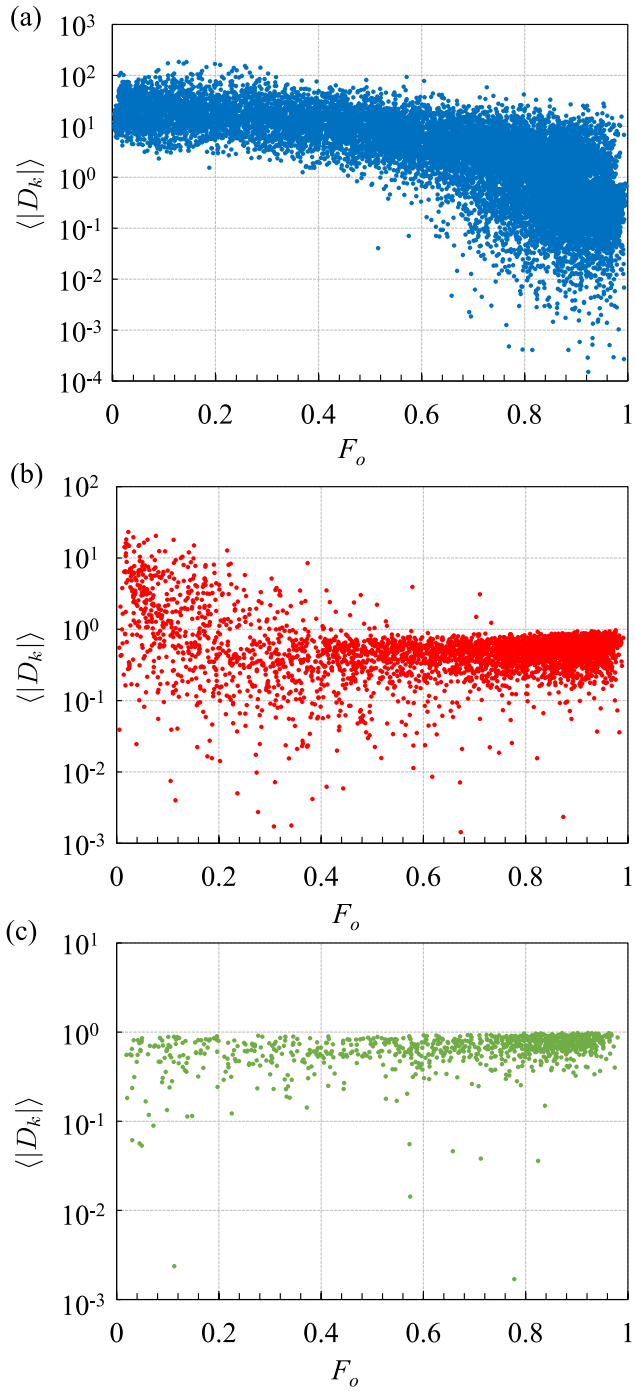

Fig. 3-8 Error of TKE as a function of F_o value, when normalized W_s is (a) 18.58, (b) 37.17, and (c) 74.34. Simulation condition is $\Delta z_0^* = 3.37$, $\Delta t^* = 0.171$.

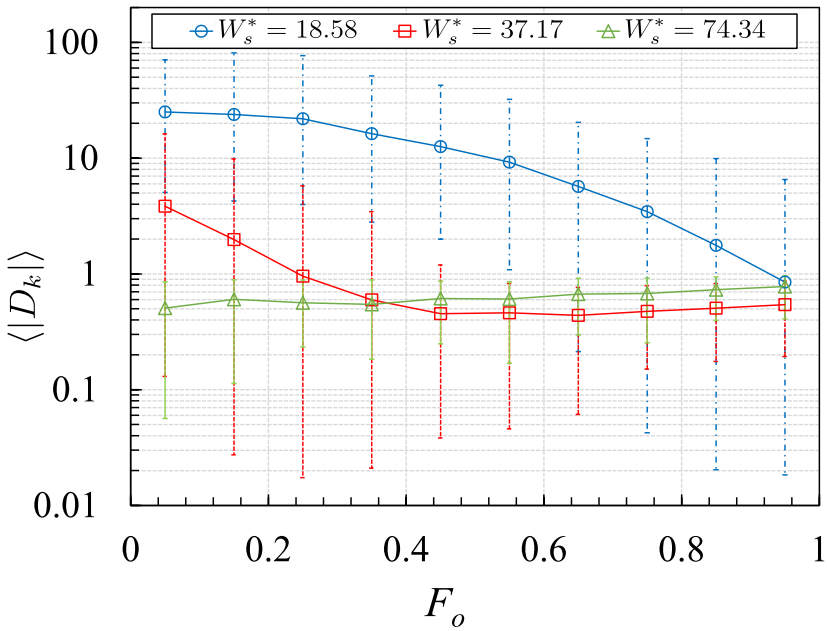

Fig. 3-9 Averaged TKE error according to F_o for various W_s.

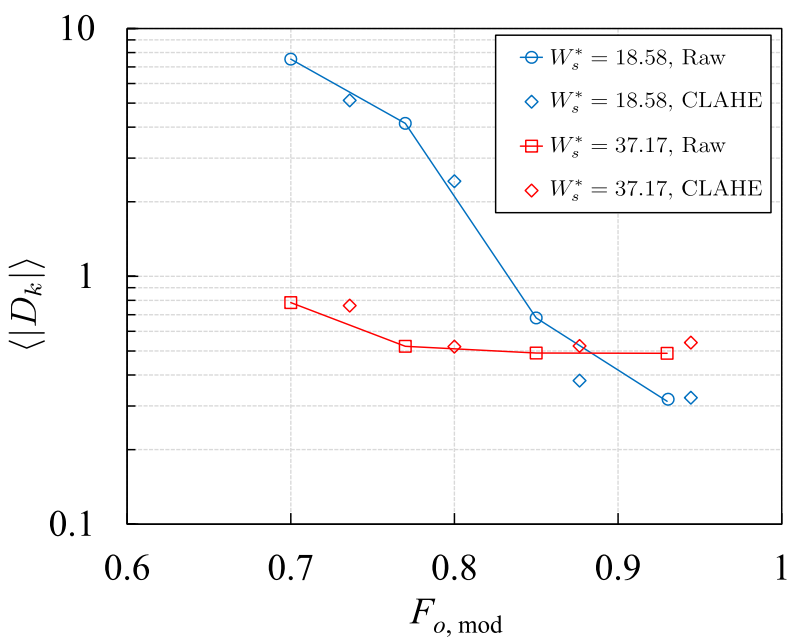

Fig. 3-10 Averaged TKE error according to modified F_o, when CLAHE pre-processing is applied to the raw images.

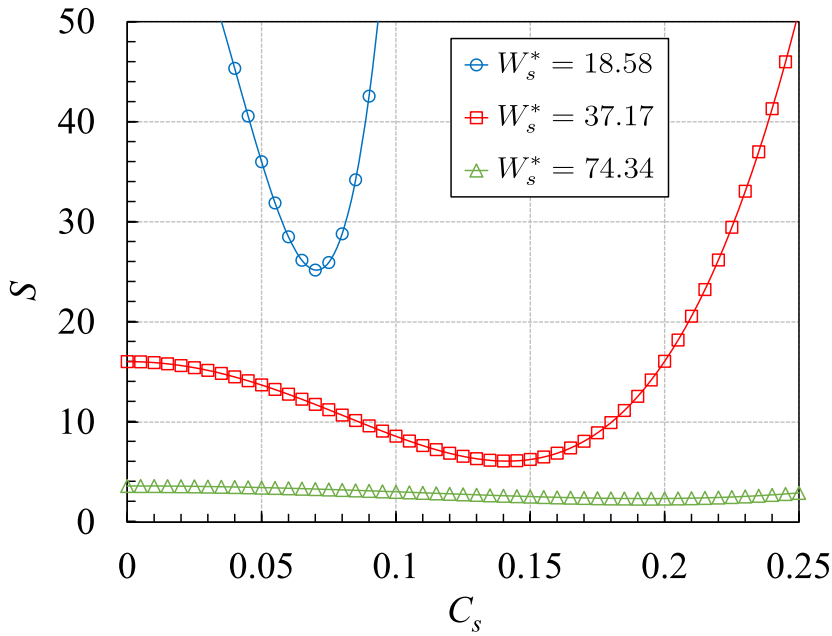

Fig. 3-11 Sum of squared difference between 2D PIV and 3D DNS dissipation rate, according to the Smagorinsky constant (C_s) for various W_s.

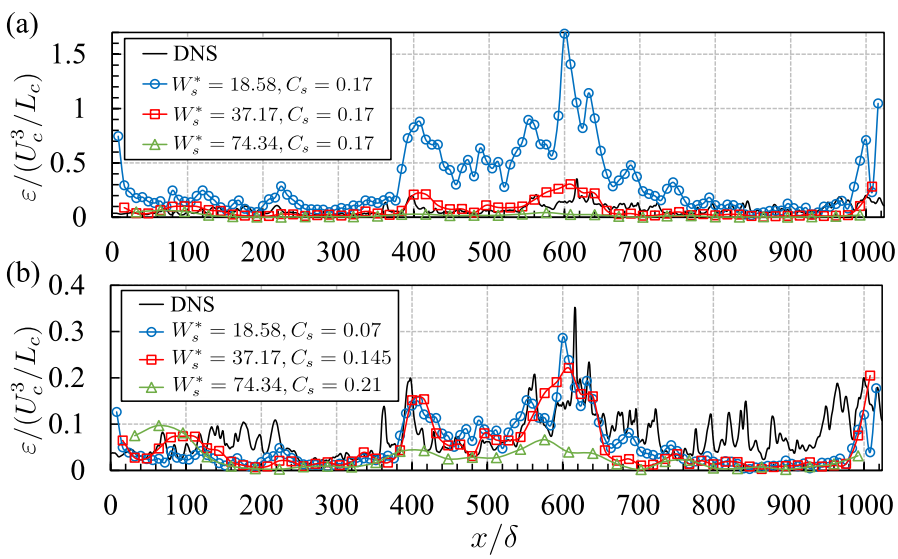

Fig. 3-12 (a) Non-dimensional dissipation rate with $C_s = 0.17$, and (b) with C_s value optimized for W_s, along one selected line for various interrogation window sizes. The normalized interframe time of the image is 0.043 and normalized laser sheet thickness is 5.90.

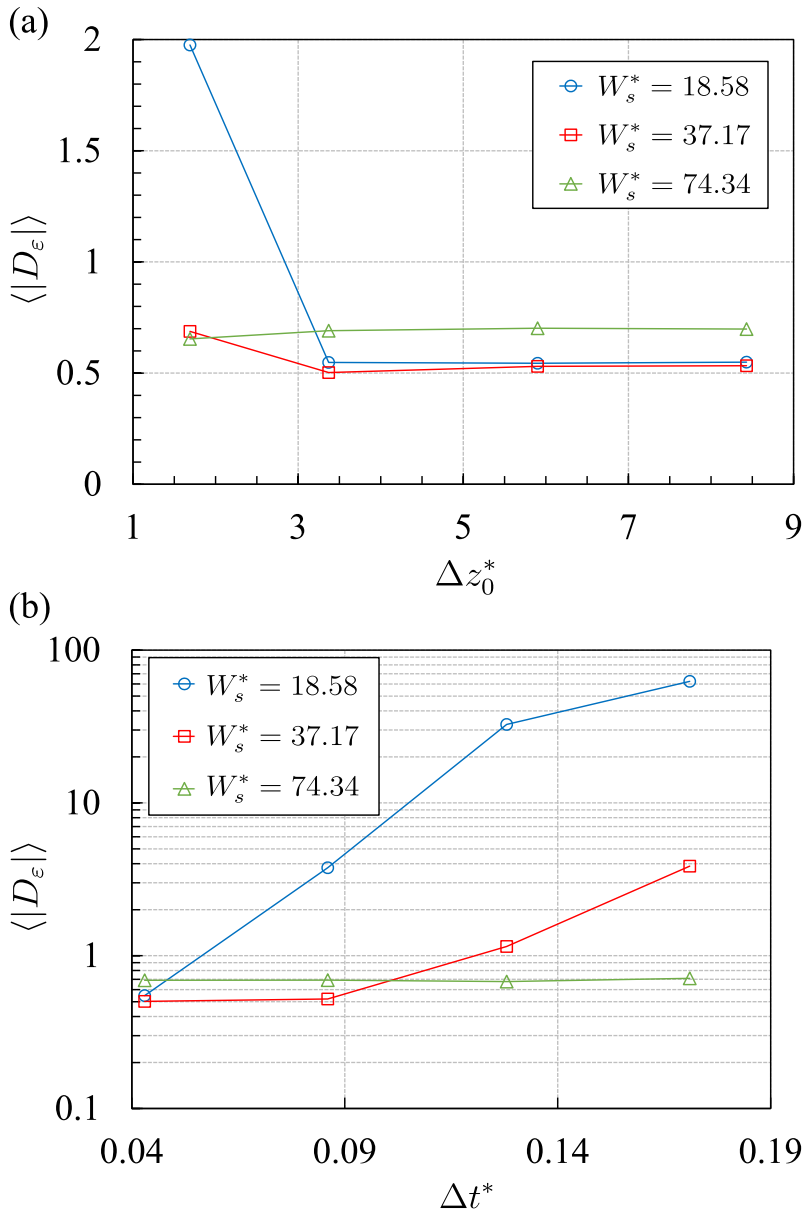

Fig. 3-13 Spatially averaged error of dissipation rate as a function of (a) laser sheet thickness and (b) camera interframe time.

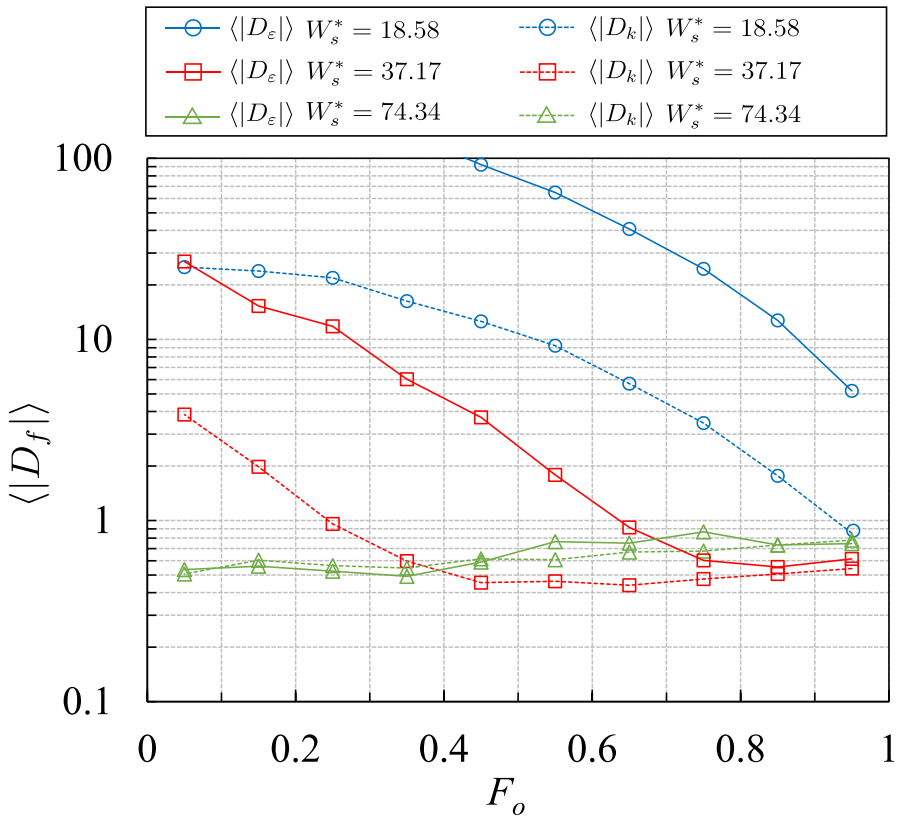

Fig. 3-14 Error of turbulence statistics as a function of F_o value. F on the y-axis refers to arbitrary turbulence statistics (TKE for dotted lines and dissipation rate for solid lines).

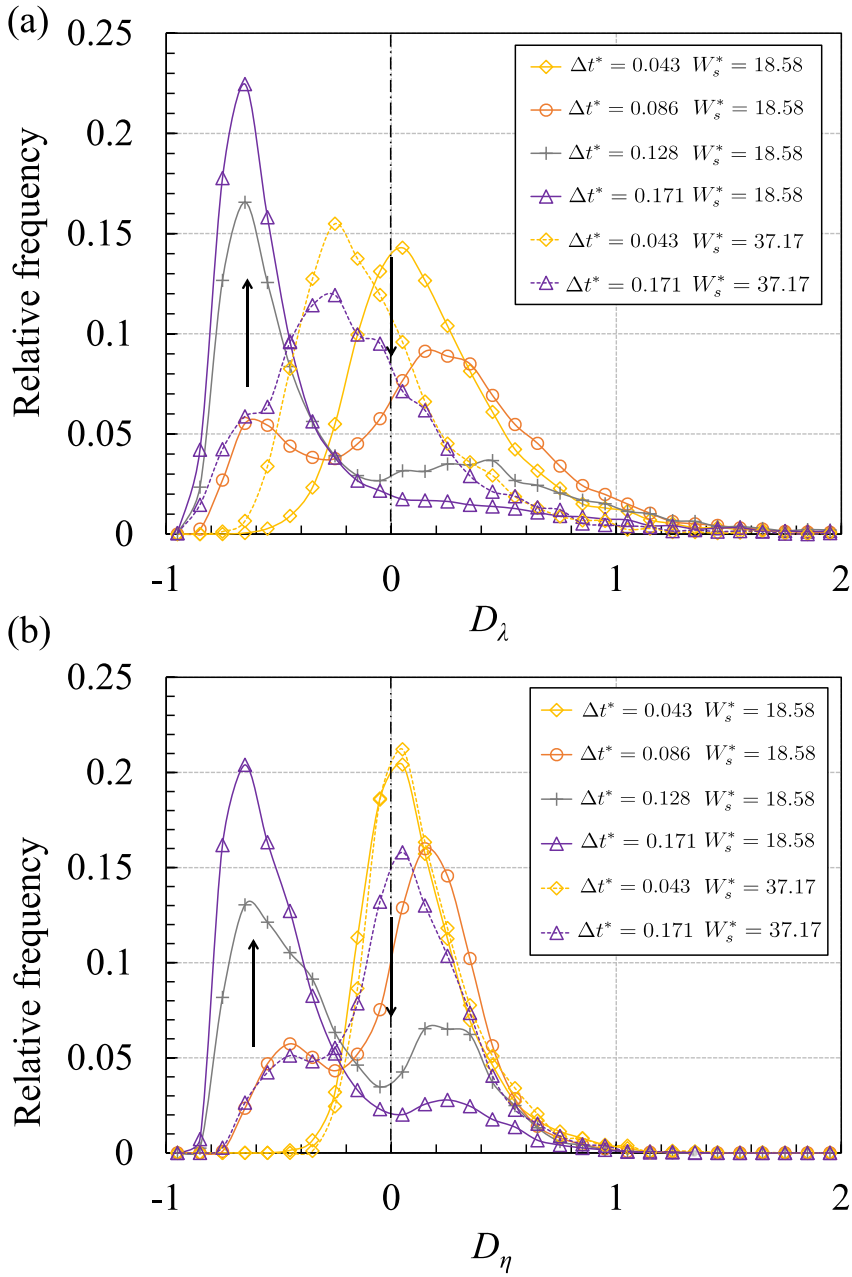

Fig. 3-15 (a) Relative frequency distribution of Taylor length scale error for various interframe time case when W_s^* is 18.58 (solid line) and 37.17 (dotted line). (b) Distribution of relative frequency of Kolmogorov length scale error.

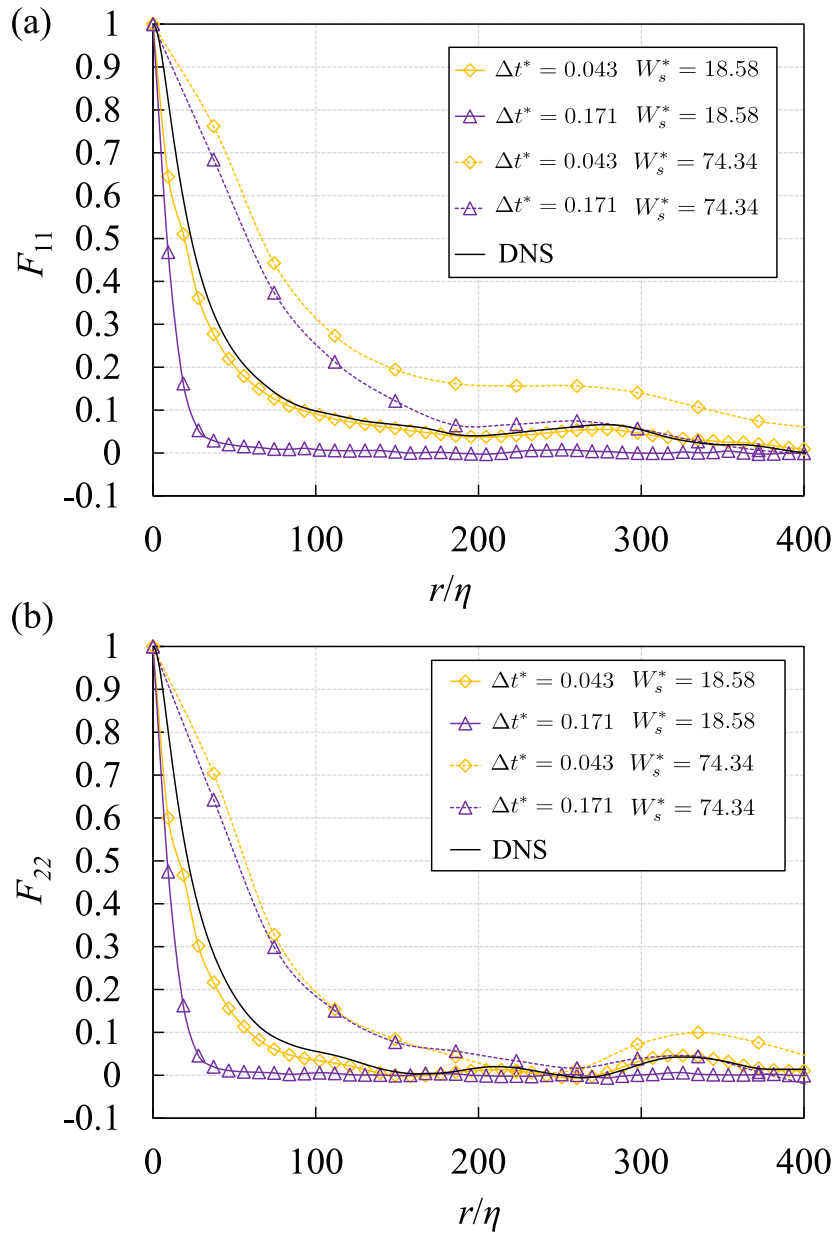

Fig. 3-16 Longitudinal velocity correlation coefficient (a) F_{11} and (b) F_{22}.

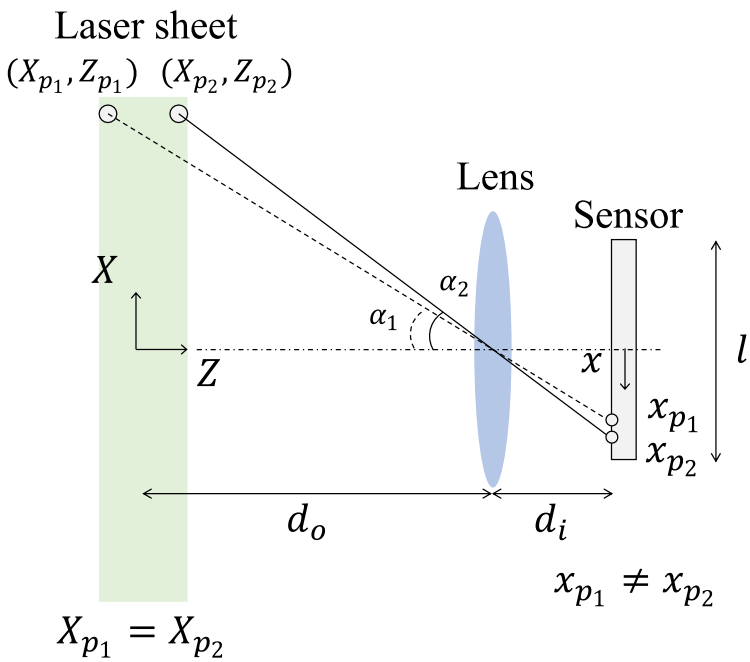

Fig. 3-17 Schematic of particle imaging system using a camera.

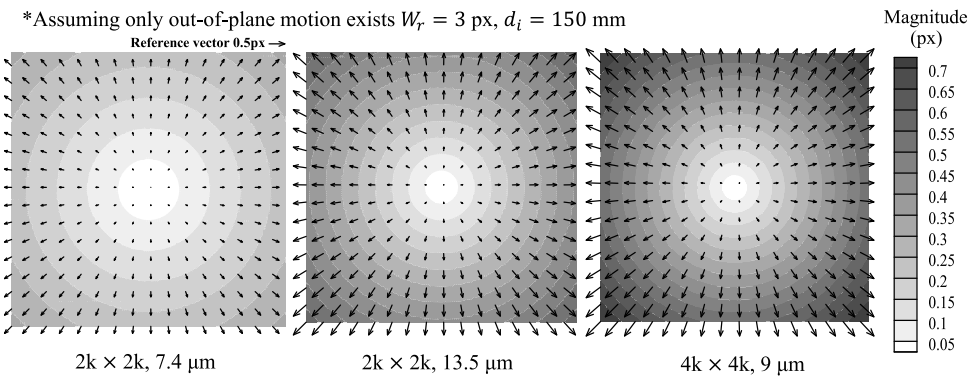

Fig. 3-18 Perspective error distribution for three types of cameras commonly used in PIV experiments.

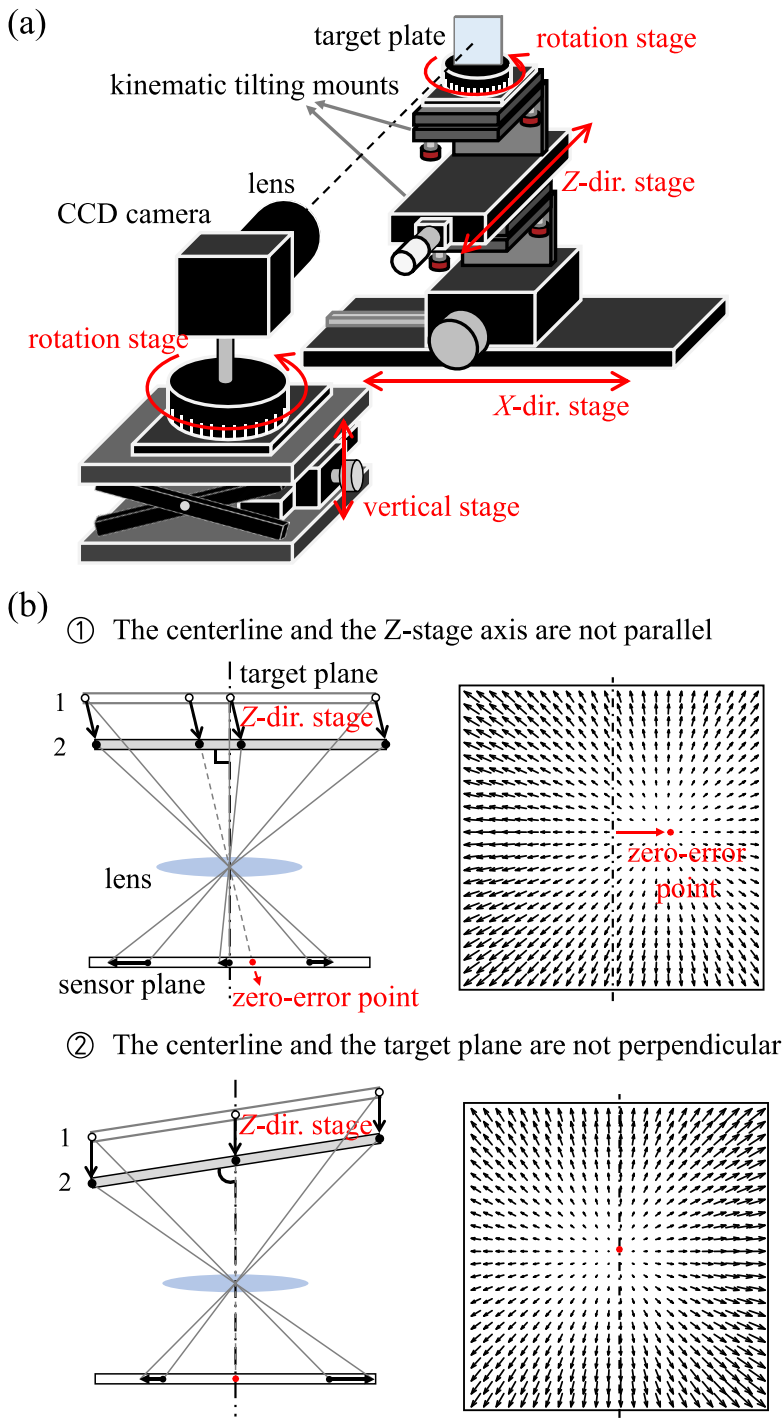

Fig. 3-19 (a) Experimental setup for validating the perspective error model equation, (b) examples of incorrect results caused by misalignment.

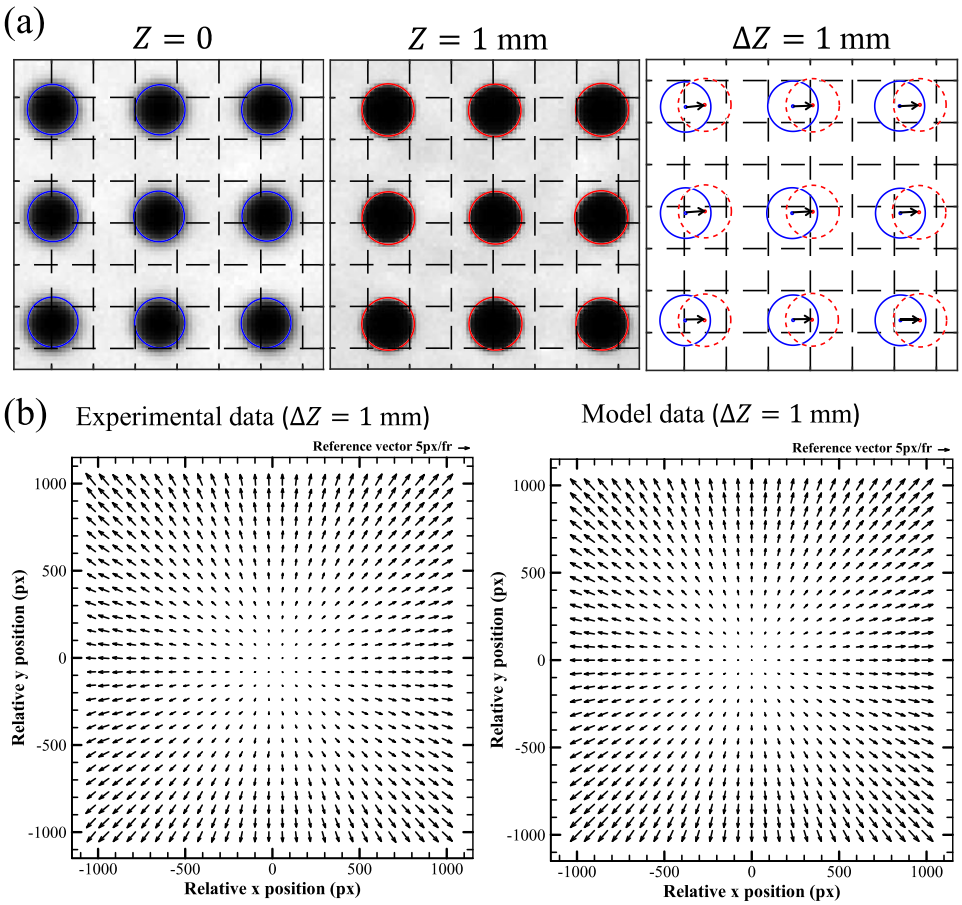

Fig. 3-20 (a) Zoomed-in images of the dotted target moving out of plane and resulting in-plane displacement vectors, (b) displacement vector fields obtained experimentally (left) and from the model (right).

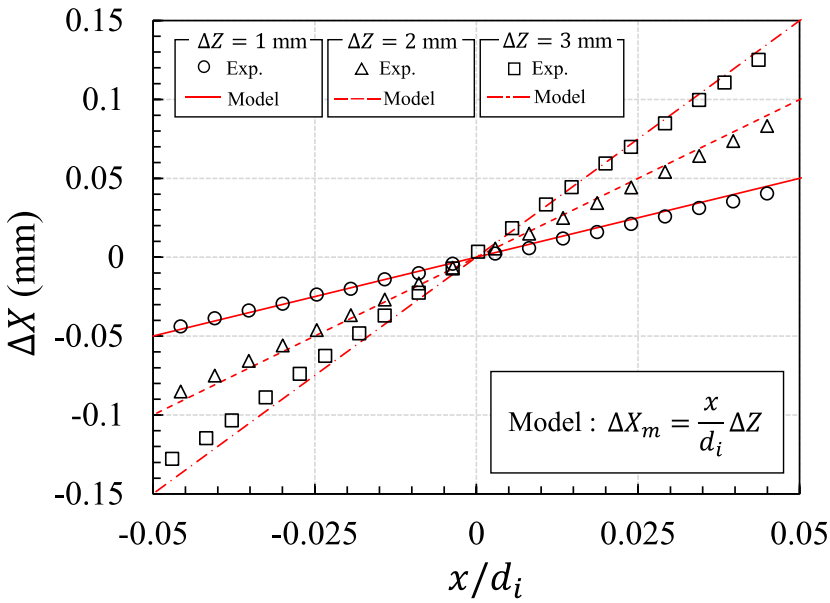

Fig. 3-21 Comparison of perspective error between the experimental data and model.

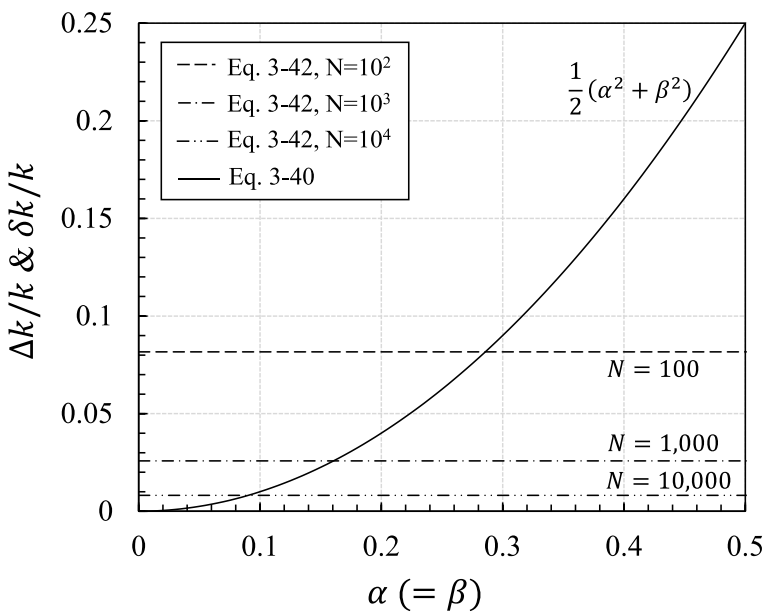

Fig. 3-22 Relative error obtained from PIV random error and perspective error.

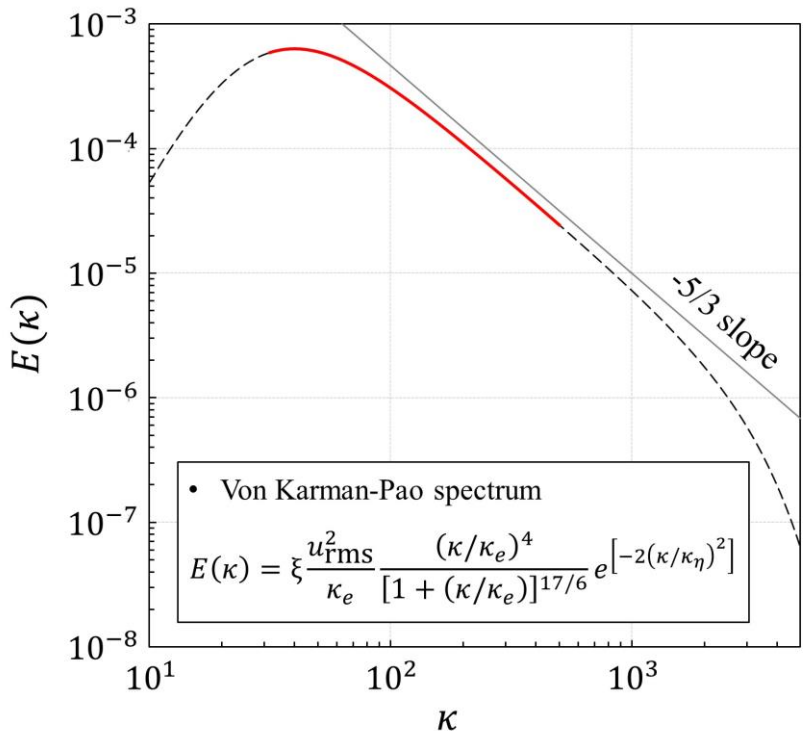

Fig. 3-23 Input spectrum used for the generation of synthetic turbulence. Red line indicates the resolved range.

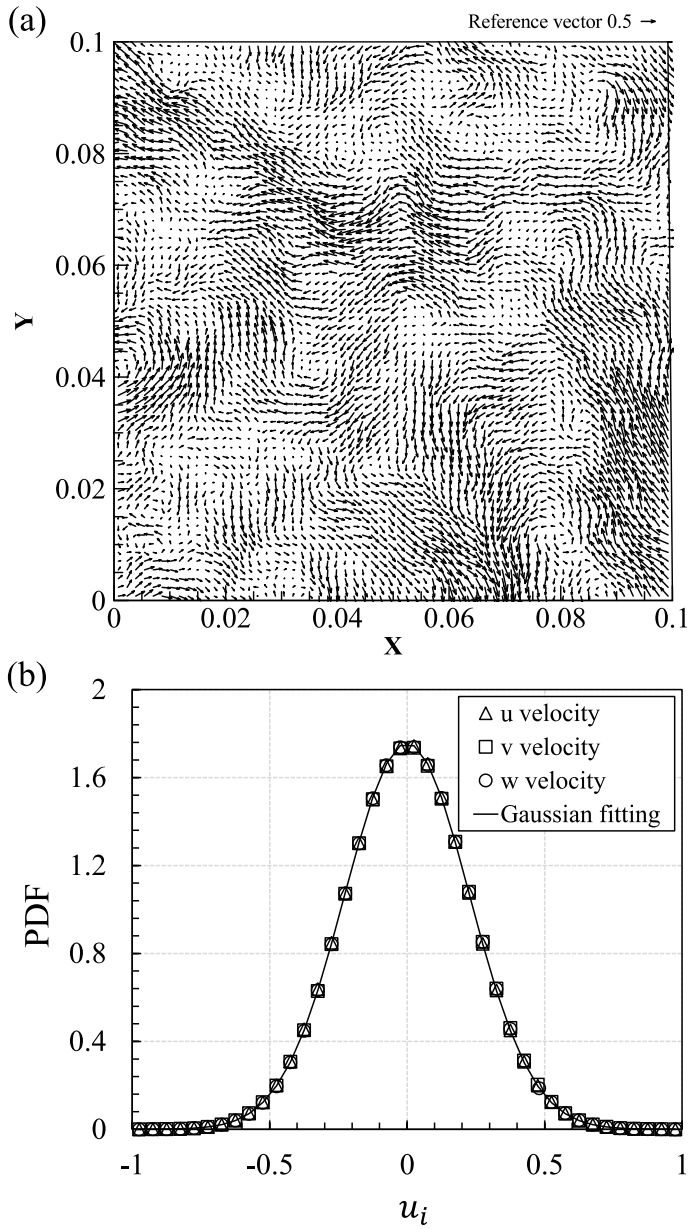

Fig. 3-24 (a) Flow field example of the generated turbulence and (b) velocity PDFs.

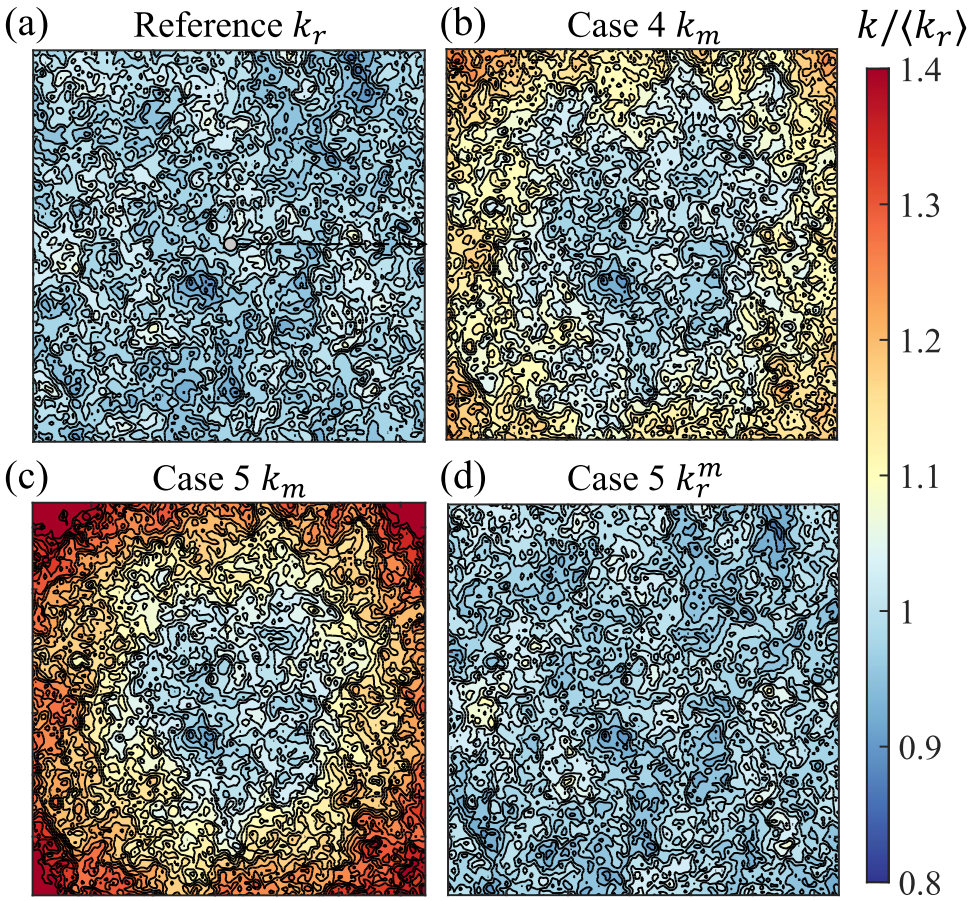

Fig. 3-25 Map of normalized TKE obtained from (a) error-free velocity data, (b) case 4 and (c) case 5 using measured data; (d) corrected value for case 5, calculated from Eq. (3-38).

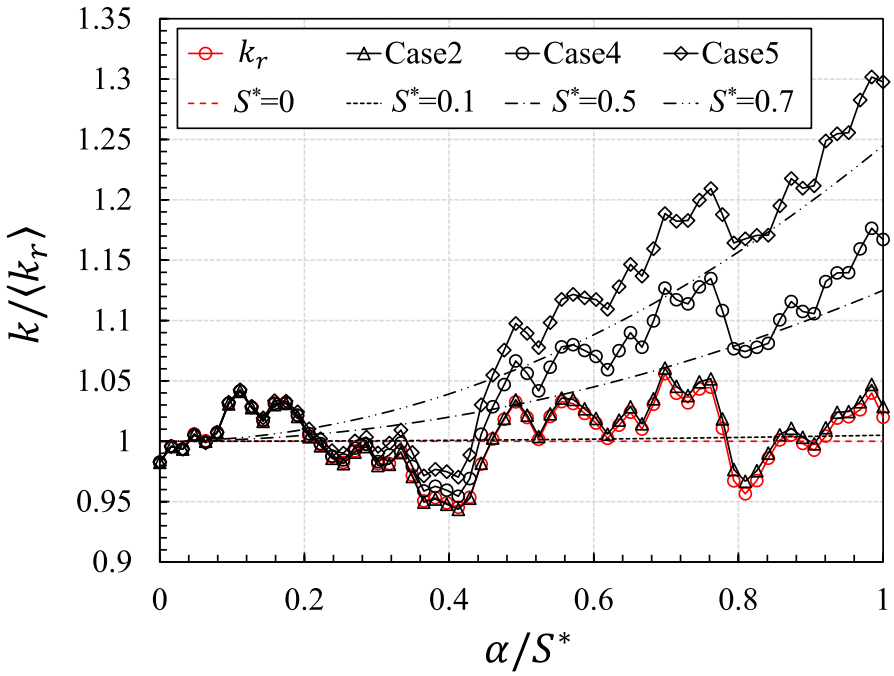

Fig. 3-26 Normalized TKE along the *x*-direction from the center of the image.

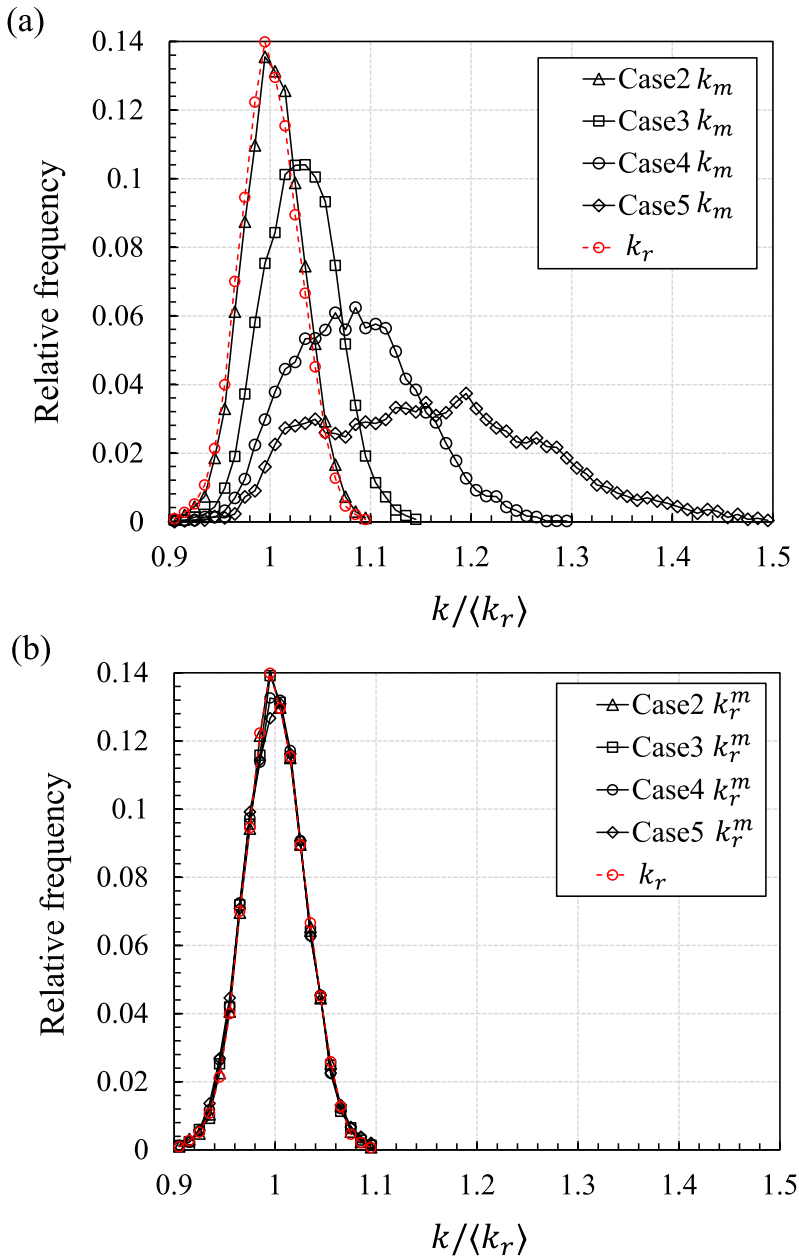

Fig. 3-27 Relative frequency distribution of normalized TKE calculated using (a) k_m and (b) k_r^m.

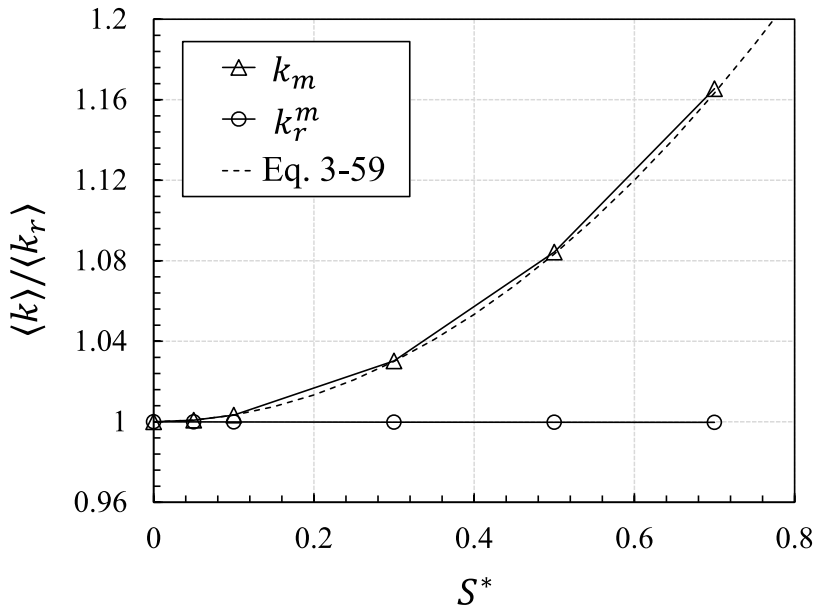

Fig. 3-28 Spatially averaged TKE with respect to S^*.

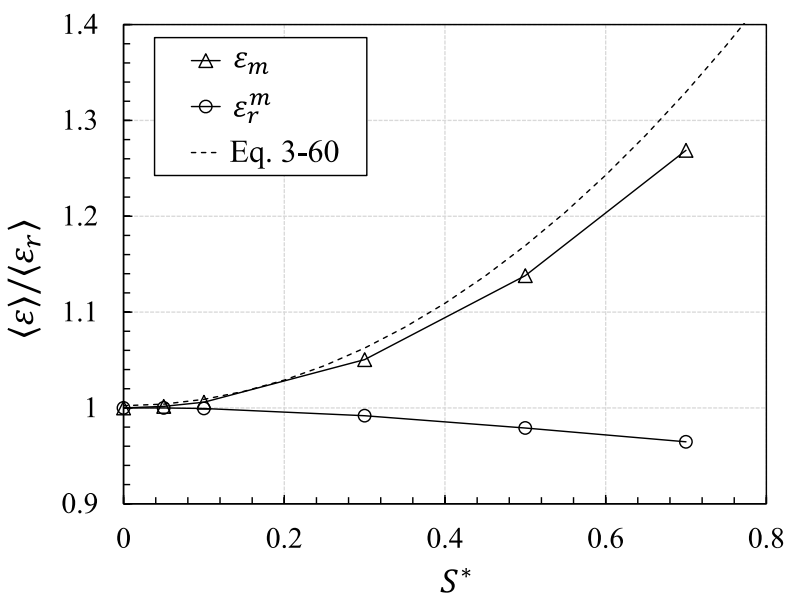

Fig. 3-29 Spatially averaged TKE dissipation rate with respect to S^*.

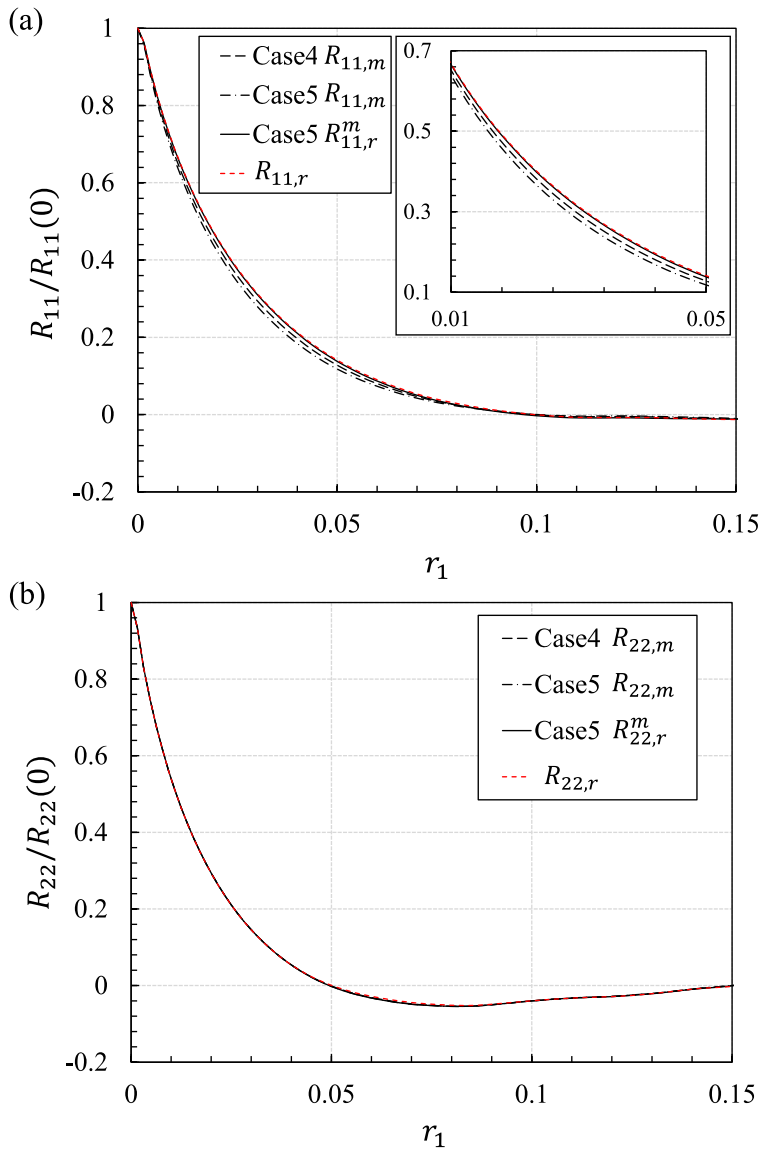

Fig. 3-30 Velocity correlation coefficient for (a) longitudinal and (b) transverse directions.

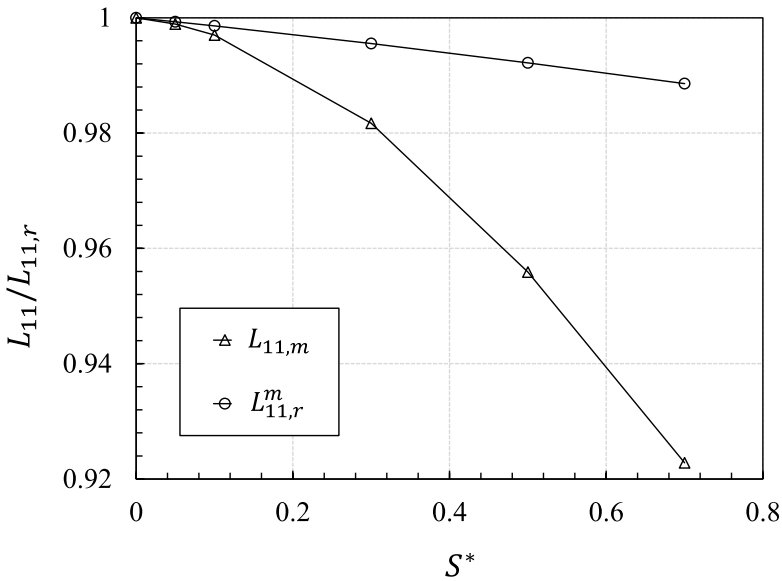

Fig. 3-31 Integral length scale obtained by integrating the longitudinal velocity correlation coefficient.

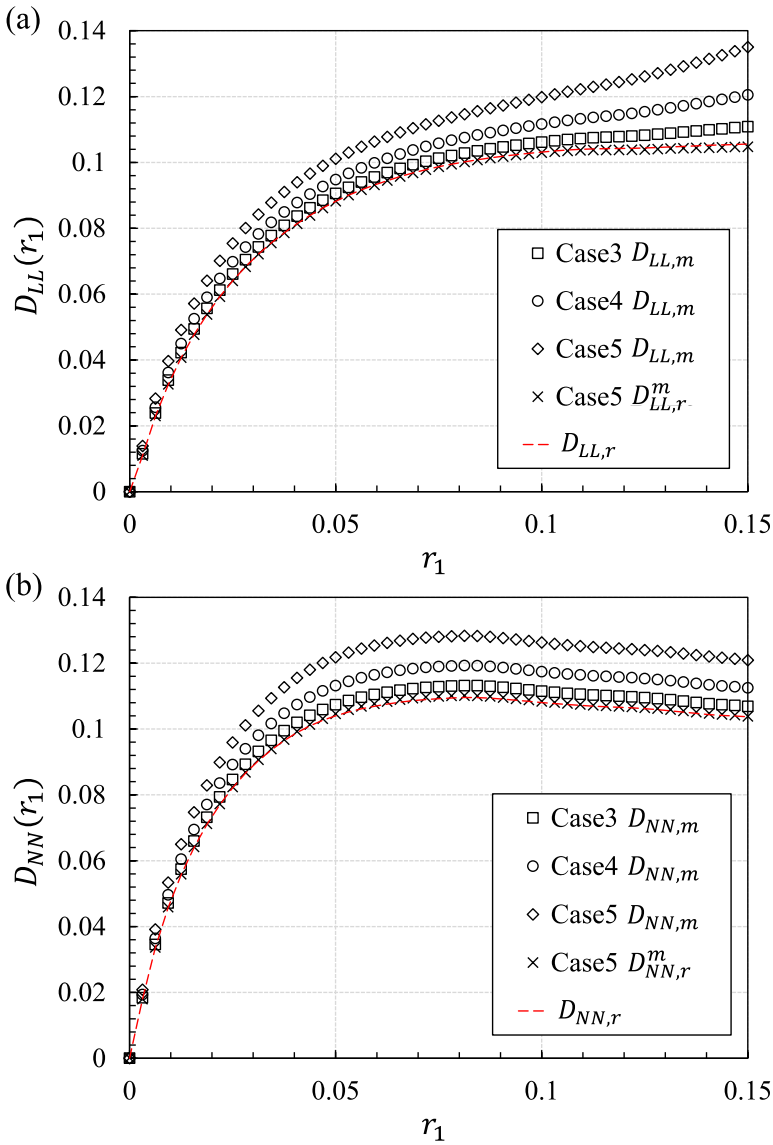

Fig. 3-32 Structure function for (a) longitudinal and (b) transverse directions.

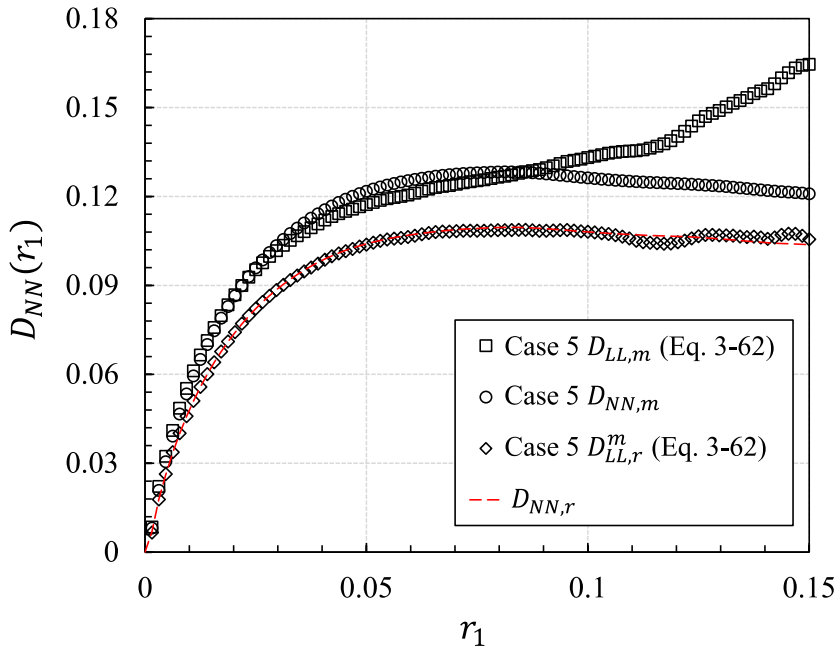

Fig. 3-33 D_{NN} calculated using Eq. (3-62) for case 5.

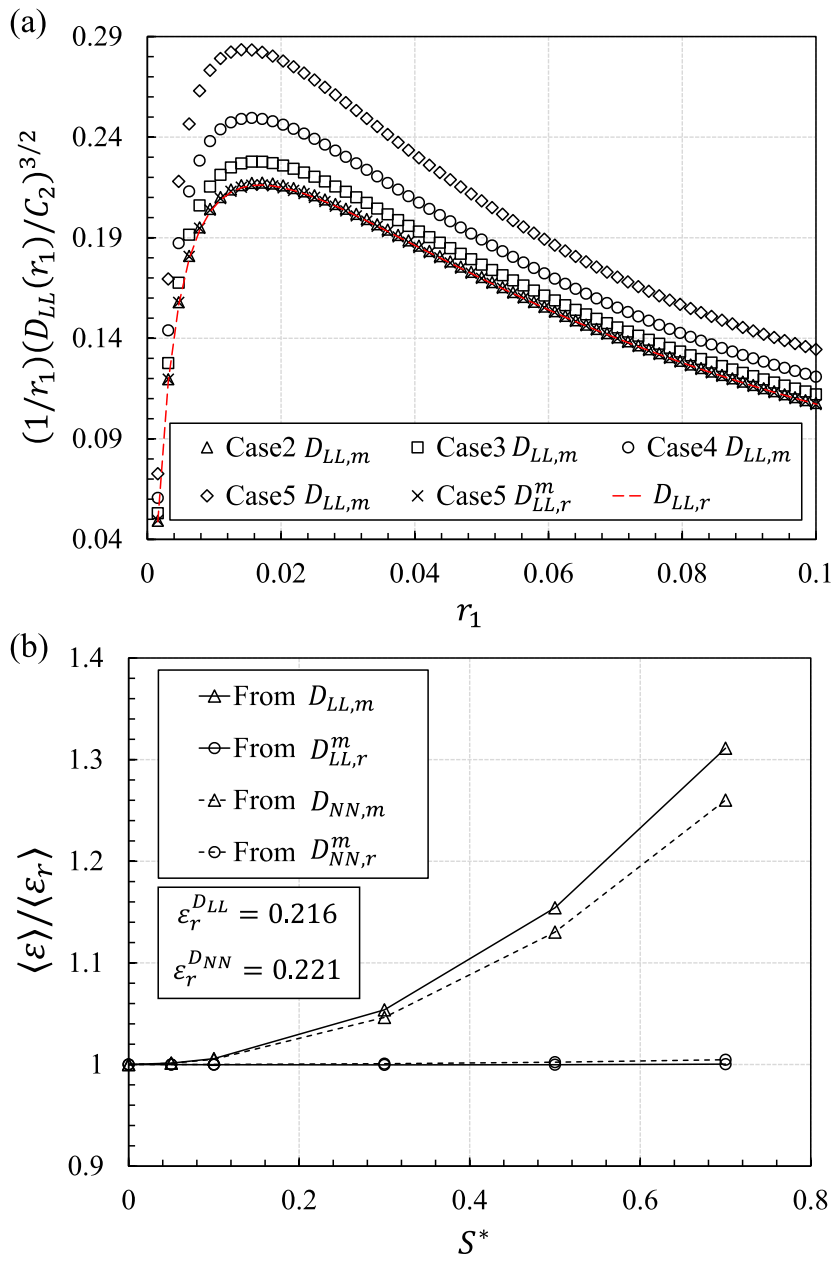

Fig. 3-34 (a) Calculation results of Eq. (3-64) using D_{LL}, (b) estimated dissipation rate using structure function.

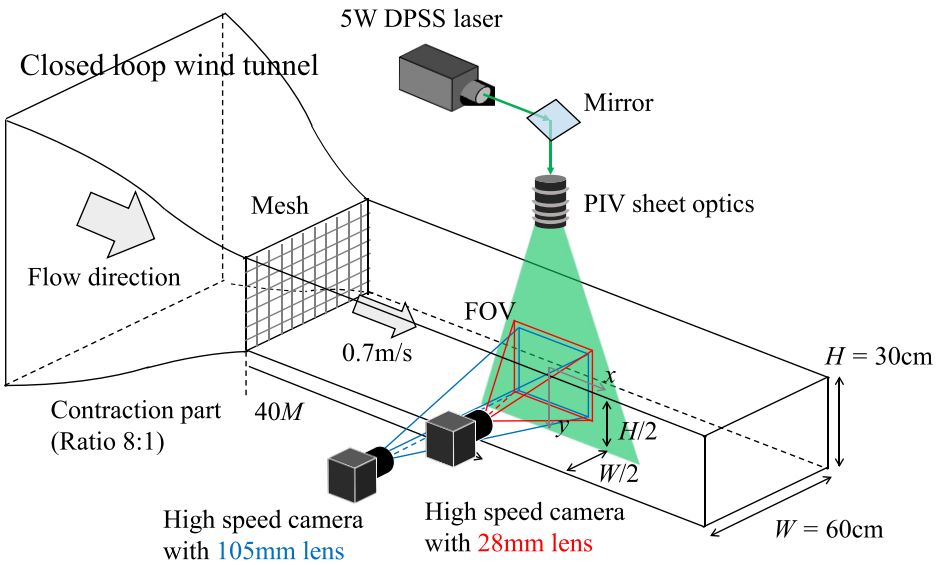

Fig. 3-35 Schematic of experimental setup for model validation.

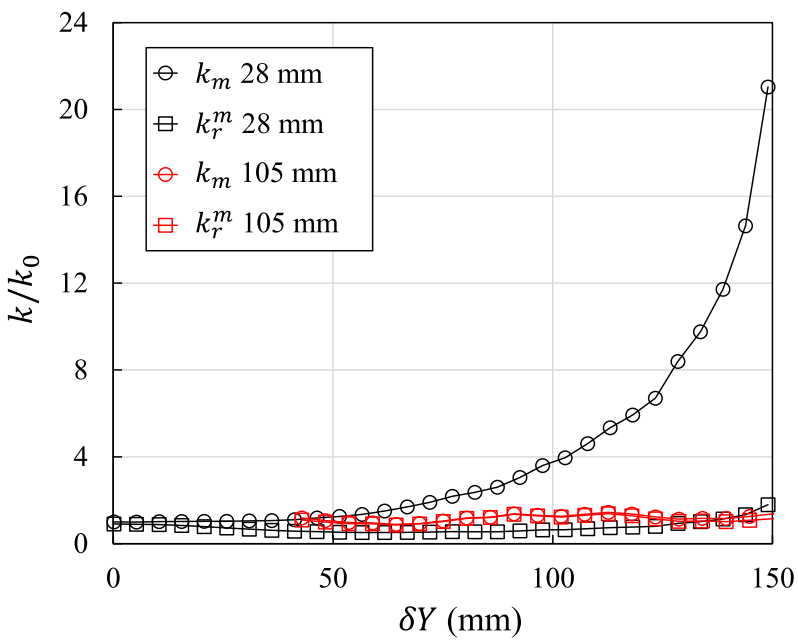

Fig. 3-36 Normalized TKE obtained from grid turbulence.

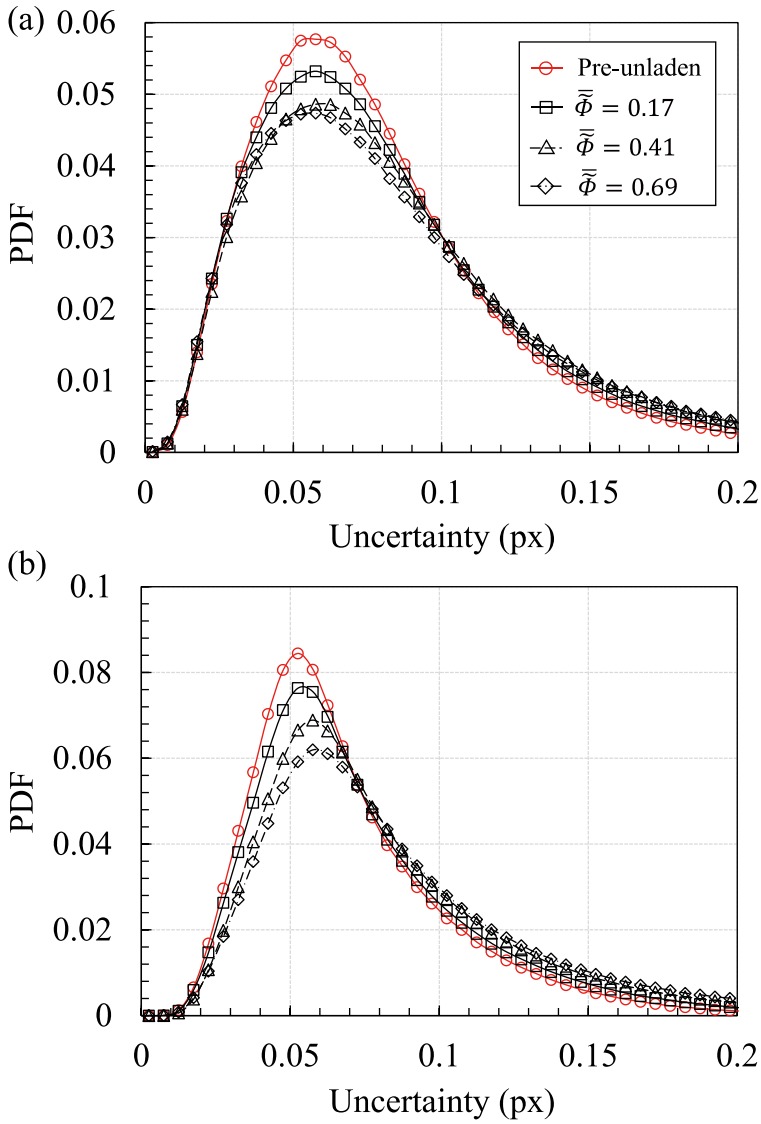

Fig. 3-37 PIV displacement uncertainty PDF estimated by (a) correlation statistics (CS) method, (b) particle disparity (PD) method.

Table 3-1 Simulation properties of the original JHTDB DNS data from Li et al. (2008), and the current study.

Parameter	Original data (Li et al.)	This study
Total simulation time ($t^*_{DNS,total}$)	0 to 2.048	0 to 0.408
Time interval between stored data sets (δt^*_{DNS})	0.002	0.008
Number of grid points (N)	1024^3	1024 × 1024 × 301
Total kinetic energy $E^* = \frac{1}{2}\overline{U_i^* U_i^*}$	0.695	0.5771
Mean dissipation rate $\varepsilon^* = 2\nu^* \overline{S_{ij}^* S_{ij}^*}$	0.0928	0.0561

Table 3-2 Synthetic image generation conditions, normalized by Kolmogorov scales, for various cases.

Case	$\Delta z_0^* = z_0/\eta$	$\Delta t^* = \Delta t/\tau_k$	$\langle F_o \rangle$	$W_s^* = W_s/\eta$
1	**1.69**	0.043	0.87	18.58, 37.17, 74.34
2	**3.37**	0.043	0.96	
3	**5.90**	0.043	0.99	
4	**8.43**	0.043	0.99	
5	3.37	**0.043**	0.96	18.58, 37.17, 74.34
6	3.37	**0.086**	0.87	
7	3.37	**0.128**	0.77	
8	3.37	**0.171**	0.66	

Table 3-3 Synthetic turbulence simulation condition.

Turbulence type	Isotropic turbulence
Velocity field resolution	128 × 128
Number of datasets	1,000
Input spectrum	von Kármán – Pao spectrum (5,000 modes)
Simulated S^* (= $\alpha_{max} = \beta_{max}$)	0.05 (Case 1) 0.1 (Case 2) 0.3 (Case 3) 0.5 (Case 4) 0.7 (Case 5)

Table 3-4 Experimental conditions.

Lens focal length (mm)	28	105
M_o	0.084	0.081
$d_i + d_o$	0.42	1.47
S^*	0.41	0.12
Number of ensembles (pairs)	2,500	3,000
Interrogation window (px)	64 (with 50% overlap)	

4. Particle pre-unladen HIT

In this chapter, we examine the validity of the HIT chamber and measurement system. To evaluate the turbulent flow generated in the HIT chamber, we first examined the overall flow fields. Fig. 4-1 (a) and (b) show the instantaneous and mean velocity fields, respectively. Coherent turbulent flow structure was observed in the instantaneous velocity field. In contrast, the mean velocity field was uniform. It should be noted that the size of the 1 m/s reference vector in the mean flow field is large compared with that in the instantaneous velocity field. Hence, the mean flow is relatively very small, and is attributed to the non-identical intensities of the eight woofer speakers and possible slight misalignment.

Next, we calculated turbulence statistics for the case of Taylor microscale Reynolds number (Re_λ) of 237. Homogeneity and isotropy are illustrated in Fig. 4-1 (c) and Fig. 4-1 (d), respectively. Homogeneity is defined by normalizing the TKE field with its spatially averaged value. The homogeneity was 0.89 – 1.08 within the ROI, i.e., close to unity. This value was similar to that of several previous studies that created HIT with synthetic jets or fans (Hwang and Eaton 2004; De Jong et al. 2009; Goepfert et al. 2010). Isotropy was calculated as the ratio of the RMS velocity in the x and y directions and ranged from 0.97 to 1.21, i.e., slightly larger than unity. This range has been reported in previous studies that had similar Reynolds numbers (Hoffman and Eaton 2021). From these results, we conclude that the chamber produces HIT with small mean flow.

The intensity of the woofer speaker was controlled using the amplifier, and the resulting turbulence was examined. Fig. 4-2 (a) shows the change in spatially averaged (denoted as $\langle \cdot \rangle$) RMS and mean velocity according to the changes in speaker intensity. As the speaker intensity is increased, the RMS velocity increased whereas the mean velocity remained small. The Re_λ of the turbulence increased to 271 and the RMS velocity reached roughly 1.2 m/s. Fig. 4-2 (b) shows the PDF of the fluctuation velocity. In all cases, the x- and y-direction velocity PDFs appear similar, and they have a Gaussian distribution. This implies that the generated turbulence is isotropic.

We now calculate TKE using the RMS velocity as follows:

$$k \equiv \frac{1}{2}\overline{u_i u_i} \approx \frac{3}{4}\overline{u_1^2 + u_2^2} \tag{4-1}$$

where u is the fluctuation velocity and the subscript i represents the i-direction component. The overbar represents an ensemble-averaging operator. In isotropic

turbulence, the equation $\overline{u_3^2} \approx 1/2\overline{(u_1^2 + u_2^2)}$ holds, which allows the approximation in Eq. (4-1). Fig. 4-3 shows the TKE obtained in this study, along with those from previous studies (Yang and Shy 2005; Hwang and Eaton 2006; De Jong et al. 2009; Goepfert et al. 2010; Tanaka and Eaton 2010; Lian et al. 2013; Dou et al. 2016; Carter and Coletti 2017; Hoffman and Eaton 2021). The subscript 0 on the *y*-axis represents a physical quantity in particle-free turbulence. Hwang and Eaton (2006), Tanaka and Eaton (2010), Lian et al. (2013) and De Jong et al. (2009) used a truncated cube-shaped chamber, as adopted in this study. A comparison of these four studies shows that our chamber could reach the highest Re_λ. In addition, it can be observed that the performance is similar to those of various other types of turbulence generators (Yang and Shy 2005; Goepfert et al. 2010; Hoffman and Eaton 2021).

The TKE dissipation rate was calculated as follows:

$$\varepsilon = 2\nu_f s_{ij} s_{ij} = \nu_f \left(\overline{\frac{\partial u_i}{\partial x_j}\frac{\partial u_i}{\partial x_j}} + \overline{\frac{\partial u_i}{\partial x_j}\frac{\partial u_j}{\partial x_i}} \right) \tag{4-2}$$

where s denotes the strain rate tensor. The subscripts i and j denote the i- and j-direction components, respectively. v is the kinematic viscosity and the subscript f denotes the fluid phase. We can directly calculate Eq. (4-2) using the velocity field obtained through PIV. However, because the PIV resolution is generally much larger than the Kolmogorov length scale, direct calculations may underestimate the dissipation rate (Sheng et al. 2000). Therefore, indirect methods are widely used to estimate the dissipation rate. De Jong et al. (2009) and Xu and Chen (2013) introduced different methods for indirectly calculating the dissipation rate in isotropic turbulence. Among these, the method employing the 2nd-order structure function has been widely used in several studies (Dou et al. 2016; Hoffman and Eaton 2021). The dissipation rate can be calculated using the longitudinal 2nd-order structure function (D_{LL}) as follows:

$$\varepsilon = 1/r_1 \left(D_{LL}(r_1)/C_2\right)^{3/2} \tag{4-3}$$

where r_1 is the distance between two vectors in the x-direction, and C_2 is a universal constant set to 2 or 2.12 (Sreenivasan 1995; Pope 2000).

Although the dissipation rate estimated using Eq. (4-3) is valid in particle-free turbulence, it may not be valid for the particle-laden state. In the two-way coupling regime, universality may be lost due to turbulence modulation. Therefore, in this study, the dissipation rate was calculated using the direct method, because the PIV spatial resolution was comparable to the Kolmogorov length scale. The velocity gradients in Eq. (4-2) were calculated using the central difference scheme, and the

correction method proposed by Tanaka and Eaton (2007) was applied to remove random error that is amplified due to the high spatial resolution.

Fig. 4-4 (a) shows the dissipation rate obtained by the direct method and structure function (with $C_2 = 2.12$). The direct method slightly underestimates the dissipation rate compared to the structure function approach. The red diamond symbol shows the percentage difference in the dissipation rate (ε_Δ) using the two methods. This difference reached 12% at the highest Reynolds number, likely due to the value of C_2, which is generally known to vary within approximately 15% (Pope 2000). Considering this point, the results obtained by the two methods are quite similar. Thus, we decided to calculate the dissipation rate using the direct method.

Based on this dissipation rate, we examined whether the Kolmogorov 4/5 law holds for our HIT. In the inertial subrange, where local isotropy is satisfied, the Kolmogorov equation can be simplified as follows (Pope 2000):

$$D_{LLL}(r_1) = -4/5\varepsilon r_1 \tag{4-4}$$

where D_{LLL} represents the 3rd-order structure function. Eq. (4-4) implies that $-D_{LLL}/(\varepsilon r)$ remains constant at 0.8 in the inertial subrange. Fig. 4-4 (b) shows the results of the calculation of $-D_{LLL}/(\varepsilon r)$. In the two cases where the Reynolds number was not sufficiently high, this value did not reach 0.8. However, when Re_λ was sufficiently high, (i.e., beyond 200), it reached a value slightly higher than 0.8, close to Kolmogorov theory. This trend is consistent with the results of previous studies (Yeung and Zhou 1997; Moisy et al. 1999; Antonia et al. 2019). Thus, we conclude that the direct calculation approach of the dissipation rate is valid, and that the generated turbulence satisfies well-known turbulence theory.

Finally, the turbulence energy spectra were calculated from the PIV data by referring to the study of Liu et al. (1994). The 1D energy spectra in the inertial subrange satisfy the following relationship with the 3D spectrum (Liu et al. 1994; Liu et al. 1999):

$$E^{3\mathrm{D}}(\kappa) = \frac{55}{18}E_{11}^{1D}(\kappa_1) = \frac{55}{24}E_{22}^{1D}(\kappa_1) \tag{4-5}$$

where $E^{3\mathrm{D}}$ and $E^{1\mathrm{D}}$ denote the three- and one-dimensional energy spectra, respectively. κ represents the wavenumber, and the subscripts 1 and 2 indicate the x- and y-directions, respectively. Thus, $E_{11}^{1D}(\kappa_1)$ and $E_{22}^{1D}(\kappa_1)$ are the 1D longitudinal and transverse spectra, respectively. If the energy spectrum in Eq. (4-5) is normalized by the fluid kinematic viscosity and dissipation rate, it can be arranged as follows:

$$\hat{E}^{3\mathrm{D}}(\kappa) = E^{3\mathrm{D}}(\kappa)(\nu_f^5\varepsilon)^{-1/4} = \begin{cases} E_{11}^{1\mathrm{D}}(\kappa_1)\dfrac{55}{18}(\nu_f^5\varepsilon)^{-1/4} = \hat{E}_{11}^{1\mathrm{D}}(\kappa_1) \\ E_{22}^{1\mathrm{D}}(\kappa_1)\dfrac{55}{24}(\nu_f^5\varepsilon)^{-1/4} = \hat{E}_{22}^{1\mathrm{D}}(\kappa_1) \end{cases} \tag{4-6}$$

where $\widehat{\ }$ represents a dimensionless value.

Fig. 4-5 shows the normalized energy spectra calculated from the experimental data. The model spectrum (Pope 2000) is plotted with a red dashed line, where C = 1.6 and β = 2.1 were used. As can be expected from Eq. (4-6), all spectral data collapsed fairly well. In the inertial subrange where $\kappa_1\eta$ is smaller than $2\pi/60$, the slope of the spectra was close to −5/3. However, the slope increased in the dissipation range where $\kappa_1\eta$ is greater than $2\pi/60$, consistent with the model. The deviation from the model at the highest wavenumbers is likely due to noise in the PIV data (Hwang and Eaton 2006). These overall observations support the fact that HIT was produced in the chamber.

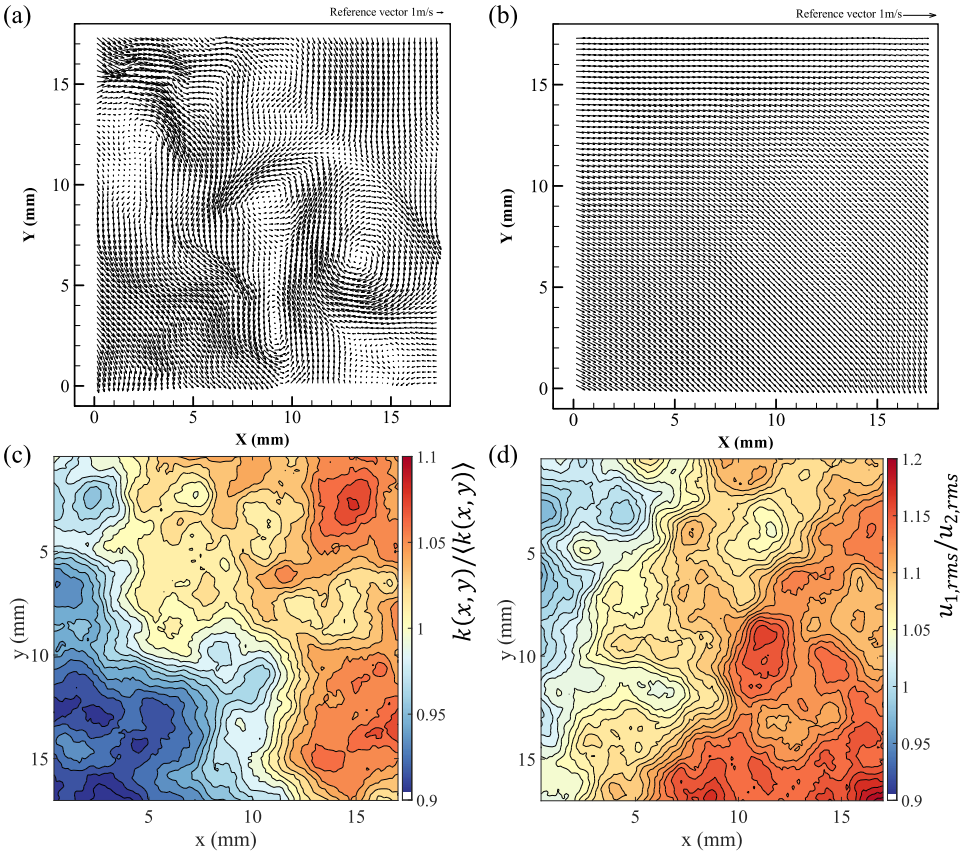

Fig. 4-1 (a) Instantaneous flow field, (b) mean flow field, (c) homogeneity, and (d) isotropy of HIT (Re_λ = 237).

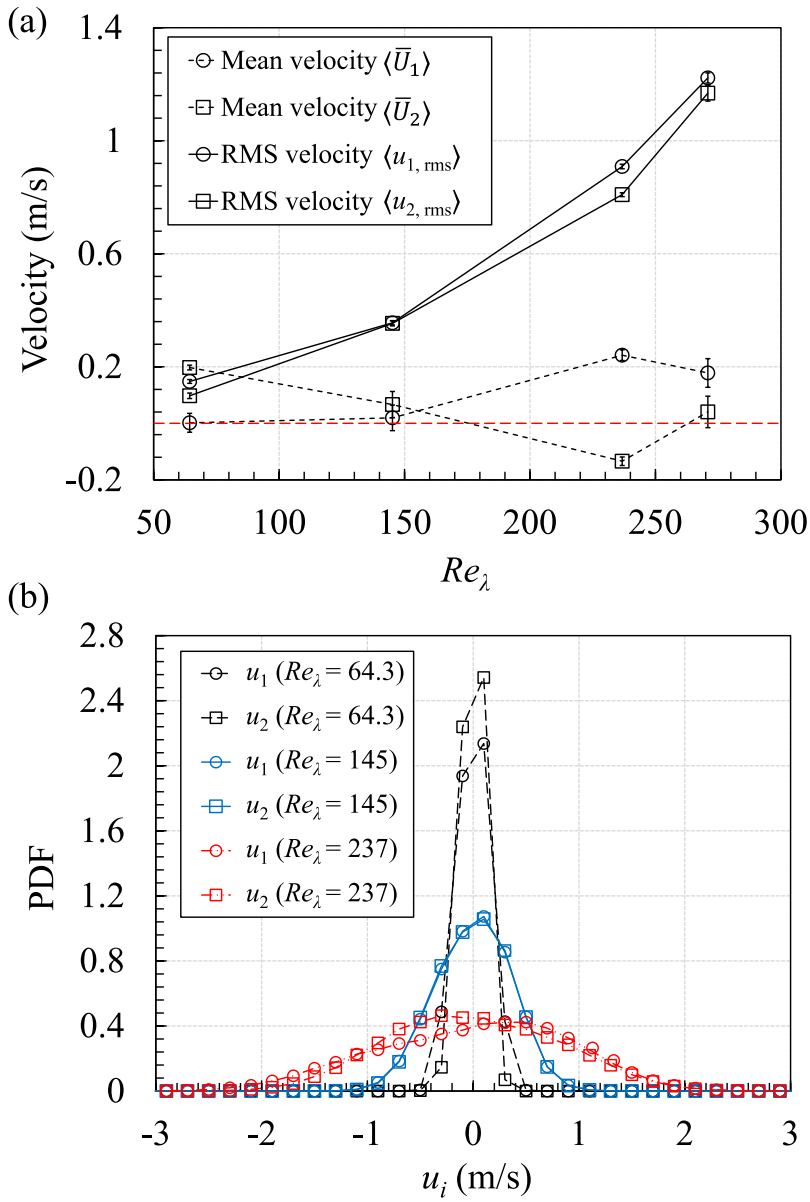

Fig. 4-2 (a) Changes in mean and RMS velocity according to speaker intensity, (b) fluctuation velocity PDFs.

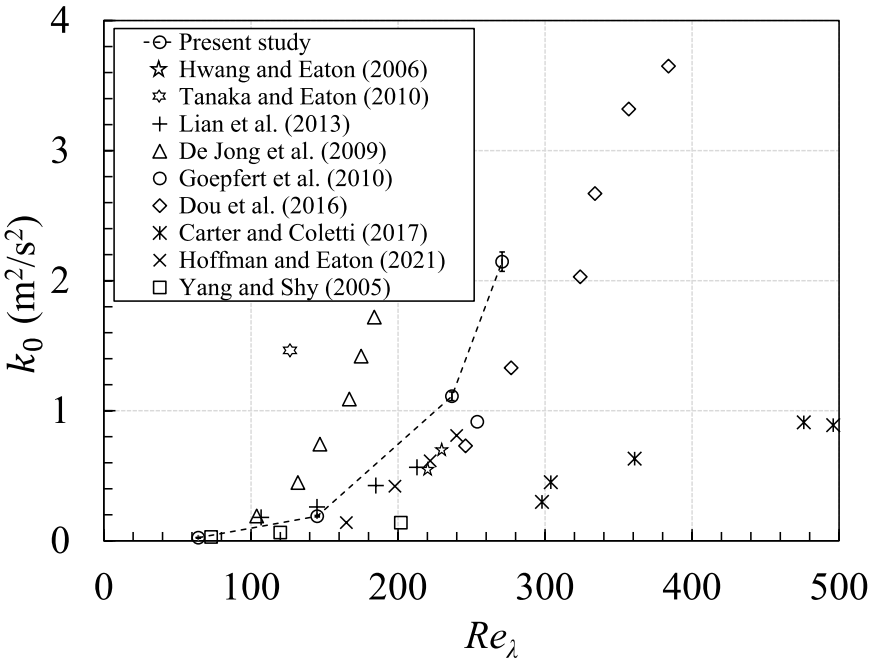

Fig. 4-3 Changes in TKE according to speaker intensity. Data obtained from previous HIT studies are also presented for comparison.

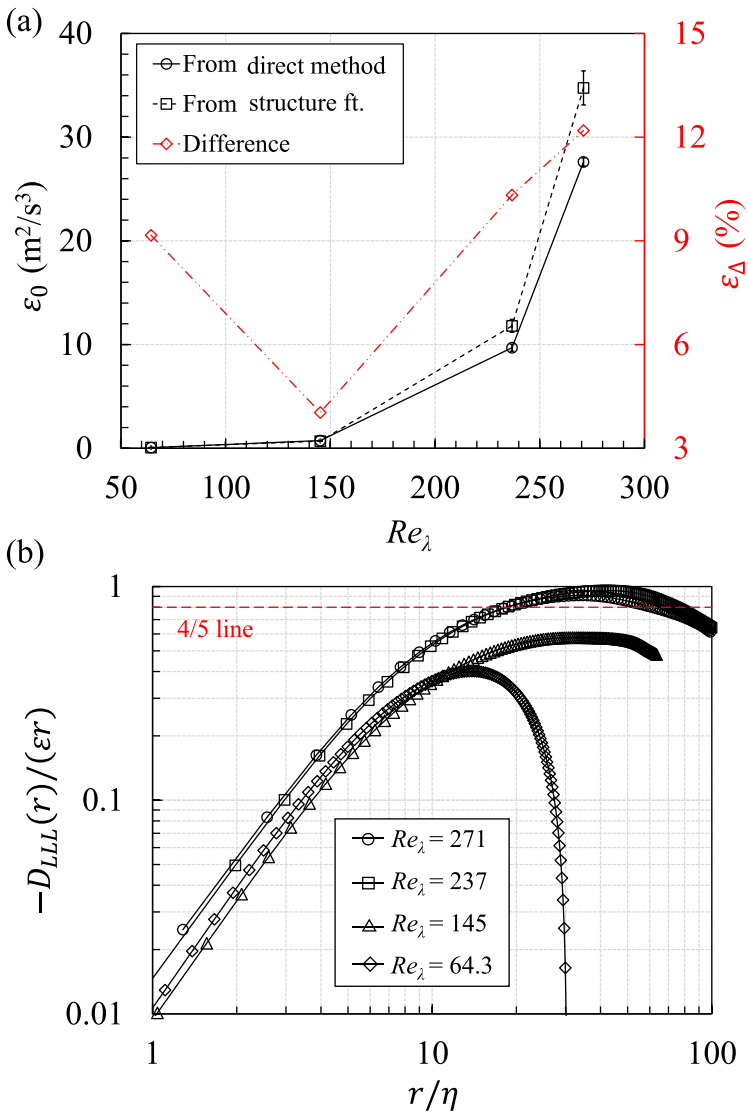

Fig. 4-4 (a) Dissipation rate obtained using the direct method and 2nd-order structure function, (b) 3rd-order structure function normalized by the directly calculated dissipation rate.

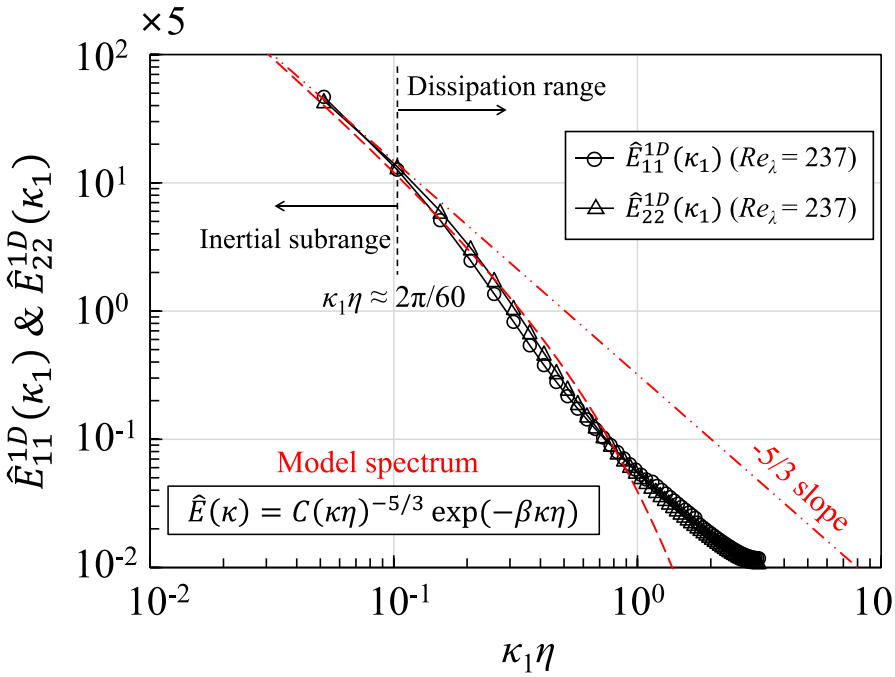

Fig. 4-5 Normalized 1D energy spectra.

5. Modulation of particle-laden HIT

5.1. Experimental results

We investigated turbulence modulation by injecting the glass particles into pre-unladen turbulence at $Re_\lambda = 237$. The particle relaxation timescale (τ_p) is defined as follows:

$$\tau_p = \frac{\rho_p d_p^2}{18\mu_f}\frac{C_{d,\,\mathrm{Stokes}}}{C_d} \approx \frac{\rho_p d_p^2}{18\mu_f}\frac{1}{1+0.15Re_p^{0.687}} \tag{5-1}$$

where ρ_p, d_p, and μ_f are the particle density, diameter, and fluid dynamic viscosity, respectively. Their values are 2500 kg/m^3, 164.4 μm, and 1.825×10^{-5} kg/(m·s), respectively. C_d denotes the drag coefficient for the sphere and $C_{d,\,Stokes}$ is the C_d for Stokes flow, defined as $24/Re_p$. Their ratio, i.e., the drag factor ($f = C_d/C_{d,\,Stokes}$), can be approximated as $1 + 0.15Re_p^{0.687}$ in the region where $2 < Re_p < 800$ (Goossens 2019), which allows the approximation in Eq. (5-1). Re_p is the particle Reynolds number, defined as Tanaka and Eaton (2010)

$$Re_p = \rho_f d_p |\vec{U} - \vec{V}|/\mu_f \tag{5-2}$$

where ρ_f is the fluid density, with the value of 1.204 kg/m^3 for air. U and V denote the fluid and particle velocities, respectively, such that $|\vec{U} - \vec{V}|$ represents the absolute slip velocity at the particle location. When the particle Stokes number (St_k) is sufficiently high ($St_k >> 1$), this slip velocity is often approximated as $\tau_p g$, where g is the gravitational acceleration 9.81 m/s^2. Using this approximation and substituting Eq. (5-2) into Eq. (5-1), τ_p can be obtained and Re_p can be subsequently calculated. Table 5-2 summarizes the experimental parameters. τ_{k0} and η_0 are the Kolmogorov timescale and length scale in pre-unladen turbulence, respectively. The data from several previous studies are also presented for comparison.

Experiments were conducted for three cases by setting the particle mass loading ($\bar{\bar{\Phi}}$), which represents the mass ratio between the particles and fluid present in a unit volume, to 0.17, 0.41, and 0.69. The experiment was carried out according to the following process. First, the woofer speakers were operated to measure the turbulence in the absence of particles (i.e., pre-unladen state turbulence). When the measurement was complete, the speakers were kept running, particles were introduced using the feeder, and particle-laden turbulence was then measured. In some cases, by turning off the feeder and measuring the turbulence in the post-unladen state, we examined whether the same result as that in the pre-unladen state

was obtained. This revealed whether the particles deposited on the floor affected the unladen turbulence (Hwang and Eaton 2006). As can be seen in Fig. 5-1, the physical quantities in the pre-unladen and post-unladen phases were similar to each other; thus, the effect of the accumulated particles was deemed negligible.

Qualitative flow fields modified by the particles are illustrated in Fig. 5-2, which shows the instantaneous and mean velocity fields of the particle-laden HIT under the highest mass loading condition. In the instantaneous velocity field, the position and velocity of the glass particles are also shown. Because the density and hence St_k of the particles are very large, it can be seen that most of them do not follow the flow exactly and fall down in the vertical direction. In addition, compared with the particle-free turbulence as illustrated in Fig. 4-1 (a), large vortical structures in the flow were noticeably reduced. This was likely because of the "screen effect" proposed by Hwang and Eaton (2006), in which the settling particles act like a screen mesh in breaking up large energetic flow structures.

Fig. 5-2 (b) shows the mean flow field of the particle-laden turbulence. Compared with the pre-unladen turbulence in Fig. 4-1 (b), the mean flow was relatively large in the downward direction. As the particles were heavy, they settle rapidly in the fluid due to gravity and experience a viscous drag force from the fluid in the upward $+y$ direction. In reaction to this, the fluid receives a downward force in the $-y$ direction from the particle. Because the particles fall uniformly through the previously homogeneous pre-unladen turbulence, the flow appears to be homogeneous even in the particle-laden state.

For quantitative analysis of turbulence modulation, we calculated TKE and dissipation rate. Fig. 5-3 shows how TKE ($\tilde{k}$) and dissipation rate ($\tilde{\varepsilon}$), normalized by their pre-unladen state value, change according to mass loading. For comparison, data from the previous studies listed in Table 5-2 are also plotted. As can be seen in the figure, the experimental results of this study showed that both TKE and dissipation rate tend to decrease with mass loading. This trend was similar to most of the data from the previous studies. In particular, the experimental results of Hwang and Eaton (2006) were most similar to those of this study, as the particle and flow types used in the experiments were essentially the same. The slight difference might be due to the difference in Re_λ of the pre-unladen turbulence.

In Fig. 5-3, only the T&E2 case initially exhibited slight turbulence augmentation, likely due to the large size of the particles. A large particle has a large terminal velocity, resulting in a high particle Reynolds number. In T&E2, Re_p was greater than

100, which can create a vertical wake behind a falling particle (Vallée et al. 2018). This wake is known to be a representative mechanism for turbulence augmentation (Balachandar and Eaton 2010). Therefore, only T&E2 with a very large Re_p showed turbulence augmentation, while the other studies with a relatively small Re_p did not display this phenomenon. It should be noted that this augmentation was quite small, possibly within the range of experimental uncertainty, and later transitioned to attenuation at the highest mass loading. It is also interesting to note that the dissipation rate initially decreased with mass loading, but then increased at the highest mass loading.

In the turbulent channel flow study conducted by Paris (2001), attenuation of TKE and dissipation rate was much larger than that in this study. This is because the modulation mechanism differs according to the flow type. In a pipe or channel flow, turbulence attenuation is more prominent than in HIT owing to the additional effect of the inhomogeneity of the mean particle force (Vreman 2007; Vreman 2015). Thus, despite P2 conditions being relatively similar to those applied in this study, the turbulence was further attenuated in P2.

Next, we compared the modulated TKE and dissipation rate from our experiments with those from physical models proposed in previous studies. Table 5-3 summarizes the relationships between the modulated TKE and dissipation rate. l_h in the model by Crowe (2000) denotes a hybrid length scale, and it physically represents a dissipative length scale in particle-laden turbulence. α_p and α_f are the volume fractions of the particle and fluid phases, respectively. l_e, $\tilde{T}$, and t_f in the models proposed by Mandø et al. (2009) and Saito et al. (2019) are the integral length scale, large-eddy turnover time, and fluid relaxation time, respectively. The fluid relaxation time is defined as $\tau_p/\bar{\bar{\Phi}}$.

$\tilde{k}$ was obtained by substituting $\tilde{\varepsilon}$ obtained from our experiments into each model equation, and is shown in Fig. 5-4. It should be noted that although the particle used in the experiment is a poly-dispersed with a standard deviation of about 12%, for simplicity, mono-disperse particle with mean diameter was assumed when calculating the model. The models proposed by Crowe (2000), Mandø et al. (2009), and Hwang and Eaton (2006) incorrectly predicted augmentation of turbulence, which is significantly different from our experimental results. However, the models presented by Tanaka and Eaton (2010), Saito et al. (2019), and Lee and Hwang (2022) predicted our experimental results well.

Among the three models with relatively good performance, we focus on the

model recently proposed by Lee and Hwang (2022). This model can predict the modulated TKE and dissipation rate using only the pre-unladen turbulence state and particle properties. Therefore, an in-depth analysis of this model can play an important role in improving the prediction of turbulence modulation. We discuss the theoretical model in the next section. In Section 5.2.1, the model of Lee and Hwang (2022) is discussed in detail. In Section 5.2.2, We used our experimental data to assess whether the assumptions used to derive this model are valid or not. In Section 5.2.3, the limitations of this model and points for improvement are discussed below.

5.2. Theoretical model

5.2.1. Point particle approach

In this section, a theoretical model using the point particle approach is derived. This has been previously published by Lee and Hwang (2022)[③]

The model development starts with the Navier–Stokes equation,

$$\rho_f \frac{DU_i}{Dt} = -\frac{\partial P}{\partial x_i} + \mu_f \frac{\partial U_i}{\partial x_j \partial x_j} \tag{5-3}$$

where ρ and μ are the density and dynamic viscosity, respectively, and subscript f indicates the fluid phase. Subscript i and j indicate i-th and j-th direction, respectively. As particles are added to the flow, momentum exchange occurs between the two phases and the above equation is transformed as follows:

$$\rho_f \frac{D\tilde{U}_i}{Dt} = -\frac{\partial \tilde{P}}{\partial x_i} + \mu_f \frac{\partial \tilde{U}_i}{\partial x_j \partial x_j} - \tilde{f}_i \tag{5-4}$$

where ~ refers to a physical quantity of the particle-laden state. The term $\tilde{f}_i$ refers to the force per unit volume that a fluid gives to (or receives from) the particles. In this study, particle-particle interactions occurring in the three- or four-way coupling regime are not considered, and the focus is only the dilute regime in which two-way coupling occurs.

The expression of $\tilde{f}_i$ can be obtained through the particle dynamic equation of motion. Particles in a flow are subjected to various types of forces, and the particle dynamic equation taking them all into account is expressed as (Maxey and Riley 1983; Kuerten 2016):

$$m_p \frac{d\tilde{V}_i}{dt} = F_{i,D} + F_{i,B} + F_{i,PG} + F_{i,AM} + F_{i,BH} \tag{5-5}$$

where subscript p and i denote particle and the i-direction component, respectively. m_p represents the mass of the particle. $F_{i,D}$, $F_{i,B}$, $F_{i,PG}$, $F_{i,AM}$, and $F_{i,BH}$ are drag force, body force, pressure gradient force, added mass force, and Basset history force acting in the i-direction, respectively. Each force term can be expressed as follows (Maxey

---

③ Lee H, Hwang W, "Prediction of homogeneous isotropic turbulence modulation by small and heavy particles". Physics of Fluids, 2022, © AIP Publishing

and Riley 1983; Elghobashi and Truesdell 1992; Elghobashi and Truesdell 1993; Balachandar and Eaton 2010; Kuerten 2016):

$$m_p \frac{d\tilde{V}_i}{dt} = \frac{m_p}{\tau_p}\left(\tilde{U}_i - \tilde{V}_i\right) + \left(\rho_p - \rho_f\right)\mathcal{V}_p g_i + m_f \frac{D\tilde{U}_i}{Dt} + \frac{1}{2}\rho_f \mathcal{V}_p \left(\frac{D\tilde{U}_i}{Dt} - \frac{D\tilde{V}_i}{Dt}\right) + \frac{3}{2}\sqrt{\pi \rho_f \mu_f} d_p^2 \int_0^t \frac{d}{d\tau}\frac{\left(\tilde{U}_i - \tilde{V}_i\right)}{(t-\tau)^{1/2}} d\tau \tag{5-6}$$

where $\mathcal{V}$, g, ρ, τ_p, and d_p are volume, gravitational acceleration, density, particle timescale, and particle diameter, respectively. D/Dt is the material derivative. m_f is the mass of the fluid occupying the same volume as the particle. Therefore, m_p and m_f can be expressed as $\rho_p \mathcal{V}_p$ and $\rho_f \mathcal{V}_p$, respectively, and using this fact, the right-hand side can be transformed as follows.

$$m_p \frac{d\tilde{V}_i}{dt} = \rho_p \mathcal{V}_p \left[\begin{array}{c} \frac{1}{\tau_p}\left(\tilde{U}_i - \tilde{V}_i\right) + \left(1 - \frac{\rho_f}{\rho_p}\right) g_i + \frac{\rho_f}{\rho_p}\frac{D\tilde{U}_i}{D\tilde{t}} \\ + \frac{1}{2}\frac{\rho_f}{\rho_p}\left(\frac{D\tilde{U}_i}{Dt} - \frac{D\tilde{V}_i}{Dt}\right) + \frac{3}{2}\sqrt{\frac{\pi \rho_f \mu_f}{\rho_p^2}}\frac{d_p^2}{\mathcal{V}_p}\int_0^t \frac{d}{d\tau}\frac{\left(\tilde{U}_i - \tilde{V}_i\right)}{(t-\tau)^{1/2}} d\tau \end{array} \right] \tag{5-7}$$

In the case of a neutrally-buoyant particle, all terms in Eq. (5-7) must be considered because the particle density is smaller or comparable to the fluid density. However, in the case of heavy particles ($\rho_p >> \rho_f$) that we assume in this study, the pressure gradient force, the added mass force, and the Basset history force are very small compared to the drag and gravity force. Olivieri (2013) simulated the contribution of each force term using DNS for particles with various Stokes numbers and density ratios in HIT. The results of this study showed that Stokes drag was dominant compared to pressure gradient, added mass, and Basset history force when the Stokes number was 10 and the density ratio was 10^3. This fact supports assumption of ignoring other terms except for Stokes drag. Several other previous studies have also used this assumption (Elghobashi and Truesdell 1992; Elghobashi and Truesdell 1993; Armenio and Fiorotto 2001; Balachandar and Eaton 2010; Kuerten 2016). Although heavy particle condition constraints the applications that can be applied, this condition is ubiquitous in natural and engineering applications. Volcanic ash particles generated from volcanic eruptions range in diameter from tens to hundreds of micrometers, and the density of these particles is known to be about 10^2 – 10^3 kg/m^3. Therefore, these particles will satisfy the heavy particle condition. In addition, the behavior of aluminum oxide particles generated in a combustor using solid fuel and sand particles introduced into a turbine engine also meet these conditions. In addition, aluminum oxide particles generated from combustors using solid fuels and sand particles introduced into turbine engines also have a much higher

density than the working fluid, so the Stokes drag is dominant in the particle behavior. Thus, under the heavy particle assumption, the particle momentum equation can finally be expressed as

$$m_p \frac{d\tilde{V}_i}{dt} = \underbrace{\frac{m_p}{\tau_p}\left(\tilde{U}_i - \tilde{V}_i\right)}_{\text{Drag force}} + \underbrace{m_p g_i}_{\text{Body force}} \tag{5-8}$$

In the case of the body force, it corresponds to Earth-particle interaction, and the drag force is fluid-particle interaction. Considering the interaction between particles and fluid, the fluid receives a force equal in magnitude and opposite in direction to the particle as a reaction force of the drag force that the particle receives from the fluid. Therefore, if the Stokes drag force is exerted on N mono-dispersed particles with diameter d_p in a fluid cell with volume V_f, $\tilde{f}_i$ can be expressed as follows (Tanaka and Eaton 2008):

$$\tilde{f}_i = \frac{N}{V_f}\underbrace{3\pi\mu_f d_p\left(\tilde{U}_i - \tilde{V}_i\right)}_{\text{Stokes drag}} = \frac{\rho_f \tilde{\Phi}}{\tau_p}\left(\tilde{U}_i - \tilde{V}_i\right) \tag{5-9}$$

where $\tilde{V}_i$ and $\tilde{\Phi}$ represent the particle velocity and mass loading (i.e., ratio of the total mass of particles to the mass of fluid in a unit volume), respectively, and τ_p is the particle relaxation time defined as $\rho_p d_p^2/(18\mu_f)$. If the particle Reynolds number ($Re_p \equiv \rho_f d_p|\tilde{U}_i - \tilde{V}_i|/\mu_f$) is finite, τ_p can be written as $\rho_p d_p^2/(18\mu_f\varphi)$ (Hwang and Eaton 2006; Tanaka and Eaton 2010), where φ is $1 + 0.15Re_p^{0.687}$. It should be noted that heavy particles in reality have high settling velocities within the flow, which can create wakes or vortex shedding behind the particles. Although this study excludes this effect by utilizing the small particle assumption, it is not unrealistic. According to Vallée et al. (2018), the recirculation zone behind the particle begins to develop when Re_p reaches 10. In the experimental conditions of Kulick et al. (1994) and Hwang and Eaton (2006), where solid particles were falling through air, the Re_p appears to be smaller than 10. Therefore, even if the above approximation is invoked, it can be considered to be somewhat close to the actual situation.

Although Eq. (5-9) is the result derived by assuming a mono-dispersed particle for simplicity, it can also be derived by considering the particle size distribution. If there are N poly-disperse particles in a unit volume V_f, the expression is as follows:

$$\tilde{f}_i^{poly} = \frac{\sum_{n=1}^{N} m_p^{(n)}(\tilde{U}_i - \tilde{V}_i)/\tau_p^{(n)}}{V_f} \tag{5-10}$$

where superscript (n) means n-th particle. If the particle density is the same for all particles and using the fact that $V_f = m_f/\rho_f$ and $\tilde{\Phi} = \sum_{n=1}^{N} m_p^{(n)} / m_f$, Eq. (5-10) is transformed as follows:

$$\tilde{f}_i^{poly} = \rho_f \tilde{\Phi} \frac{\sum_{n=1}^{N} \left({d_p^{(n)}}^3 / \tau_p^{(n)} \right)}{\sum_{n=1}^{N} {d_p^{(n)}}^3} (\tilde{U}_i - \tilde{V}_i) \tag{5-11}$$

By comparing Eq. (5-11) with Eq. (5-9) which is the equation for mono-disperse particles, the equivalent particle timescale τ_p^{eq} can be obtained.

$$\tau_p^{eq} = \frac{\sum_{n=1}^{N} {d_p^{(n)}}^3}{\sum_{n=1}^{N} {d_p^{(n)}}^3 / \tau_p^{(n)}} \tag{5-12}$$

When considering the size distribution of particles, we can simply calculate using τ_p^{eq} instead of τ_p included in Eq. (5-9).

The equation for the TKE of particle-laden turbulence, $\tilde{k}\ (\equiv 1/2\overline{\tilde{u}_i \tilde{u}_i})$, can be obtained from Eq. (5-4). By substituting Eq. (5-9) into Eq. (5-4),

$$\rho_f \frac{D\tilde{U}_i}{Dt} = -\frac{\partial \tilde{P}}{\partial x_i} + \mu_f \frac{\partial \tilde{U}_i}{\partial x_j \partial x_j} - \frac{\rho_f \tilde{\Phi}}{\tau_p} \left(\tilde{U}_i - \tilde{V}_i \right) \tag{5-13}$$

The following Reynolds decomposition can be applied for velocity, pressure and mass loading:

$$\tilde{U}_i = \bar{\tilde{U}}_i + \tilde{u}_i \quad \tilde{V}_i = \bar{\tilde{V}}_i + \tilde{v}_i \quad \tilde{P} = \bar{\tilde{P}} + \tilde{p} \quad \tilde{\Phi} = \bar{\tilde{\Phi}} + \tilde{\phi} \tag{5-14}$$

The overbar represents the average operator. Applying Eq. (5-14) to (5-13) and averaging, we obtain

$$\rho_f \frac{\partial \bar{\tilde{U}}_i}{\partial t} + \rho_f \frac{\partial \left(\bar{\tilde{U}}_i \bar{\tilde{U}}_j + \overline{\tilde{u}_i \tilde{u}_j} \right)}{\partial x_j} = -\frac{\partial \bar{\tilde{P}}}{\partial x_i} + \frac{\partial \bar{\tilde{\tau}}_{ij}}{\partial x_j} - \frac{\bar{\tilde{\Phi}}}{\tau_p} \left(\bar{\tilde{U}}_i - \bar{\tilde{V}}_i \right) \tag{5-15}$$

where $\tilde{\tau}_{ij}$ is the shear stress tensor defined as $\mu_f \left(\frac{\partial \tilde{U}_i}{\partial x_j} + \frac{\partial \tilde{U}_j}{\partial x_i} \right)$. This can be decomposed as $\tilde{\tau}_{ij} = \bar{\tilde{\tau}}_{ij} + \tilde{\tau}'_{ij}$, where $\tilde{\tau}'_{ij} = \mu_f \left(\frac{\partial \tilde{u}_i}{\partial x_j} + \frac{\partial \tilde{u}_j}{\partial x_i} \right)$. By subtracting Eq. (5-15) from Eq. (5-13), we obtain the following equation.

$$\rho_f \frac{\partial \tilde{u}_i}{\partial t} + \rho_f \tilde{u}_j \frac{\partial \bar{\tilde{U}}_i}{\partial x_j} + \rho_f \bar{\tilde{U}}_j \frac{\partial \tilde{u}_i}{\partial x_j} + \rho_f \frac{\partial \left(\tilde{u}_i \tilde{u}_j\right)}{\partial x_j}$$
$$= \begin{bmatrix} -\frac{\partial \tilde{p}}{\partial x_i} + \frac{\partial}{\partial x_j}\left(\rho_f \overline{\tilde{u}_i \tilde{u}_j} + \tilde{\tau}'_{ij}\right) - \frac{\rho_f \bar{\tilde{\Phi}}}{\tau_p}\left(\tilde{u}_i - \tilde{u}_j\right) \\ -\frac{\rho_f \tilde{\phi}}{\tau_p}\left(\bar{\tilde{U}}_i + \tilde{u}_i - \bar{\tilde{V}}_i - \tilde{v}_i\right) - \frac{\rho_f}{\tau_p}\left(-\overline{\tilde{u}_i \tilde{\phi}} + \overline{\tilde{v}_i \tilde{\phi}}\right) \end{bmatrix} \tag{5-16}$$

Assuming that the entire Eq. (5-16) is $\tilde{\mathcal{K}}_i$, calculating $\overline{2\tilde{u}_i \tilde{\mathcal{K}}_i}$ yields the final TKE transport equation

$$\frac{\partial(\rho_f \tilde{k})}{\partial t} + \bar{\tilde{U}}_i \frac{\partial(\rho_f \tilde{k})}{\partial x_i} = \underbrace{-\rho_f \overline{\tilde{u}_i \tilde{u}_j} \frac{\partial \bar{\tilde{U}}_i}{\partial x_j}}_{=\tilde{\mathcal{P}}} - \underbrace{\overline{\tilde{\tau}'_{ij} \frac{\partial \tilde{u}_i}{\partial x_j}}}_{=\rho_f \tilde{\varepsilon}}$$
$$\underbrace{+\frac{\partial}{\partial x_j} \overline{\tilde{u}_i \tilde{\tau}'_{ij}} - \frac{1}{2}\frac{\partial}{\partial x_j} \rho_f \overline{\tilde{u}_i \tilde{u}_i \tilde{u}_j} - \frac{\partial}{\partial x_i} \overline{\tilde{u}_i \tilde{p}}}_{\nabla \cdot \tilde{J}}$$
$$\underbrace{-\frac{\rho_f \bar{\tilde{\Phi}}}{\tau_p}\left(\overline{\tilde{u}_i \tilde{u}_i} - \overline{\tilde{u}_i \tilde{v}_i}\right) - \frac{\rho_f}{\tau_p}\left(\overline{\tilde{\phi} \tilde{u}_i \tilde{u}_i} - \overline{\tilde{\phi} \tilde{u}_i \tilde{v}_i}\right) - \frac{\rho_f}{\tau_p} \overline{\tilde{u}_i \tilde{\phi}}\left(\bar{\tilde{U}}_i - \bar{\tilde{V}}_i\right)}_{\text{Particle coupling terms}} \tag{5-17}$$

This equation can be simply expressed as:

$$\rho_f \left(\frac{\partial \tilde{k}}{\partial t} + \bar{\tilde{U}}_i \frac{\partial \tilde{k}}{\partial x_i}\right) = \tilde{\mathcal{P}} - \rho_f \tilde{\varepsilon} + \nabla \cdot \tilde{J} - \frac{\rho_f \bar{\tilde{\Phi}}}{\tau_p}\left(\overline{\tilde{u}_i \tilde{u}_i} - \overline{\tilde{u}_i \tilde{v}_i}\right)$$
$$-\frac{\rho_f}{\tau_p}\left(\overline{\tilde{\phi} \tilde{u}_i \tilde{u}_i} - \overline{\tilde{\phi} \tilde{u}_i \tilde{v}_i}\right) - \frac{\rho_f}{\tau_p} \overline{\tilde{\phi} \tilde{u}_i}\left(\bar{\tilde{U}}_i - \bar{\tilde{V}}_i\right) \tag{5-18}$$

Where $\tilde{\mathcal{P}}$ $(\equiv -\rho_f \overline{\tilde{u}_i \tilde{u}_j} \partial \bar{\tilde{U}}_i / \partial x_j)$, $\tilde{\varepsilon}$, and $\nabla \cdot \tilde{J}$ are the production, TKE dissipation rate, and transport terms, respectively. The overbar represents the Reynolds average and u, v, and ϕ are the fluctuation components of U, V, and Φ, respectively. Subscript i denotes the i-direction component, and thus u_i and v_i are fluid and particle fluctuation velocity components in the i-direction, respectively. In isotropic turbulence laden with heavy particles, this equation can be further simplified. In this case the Stokes number ($St \equiv \tau_p / \tau_f$, where τ_f is the flow timescale) is much larger than 1, and the particles are uniformly distributed in the flow, unaffected by turbulent fluctuation (Wood et al. 2005). Thus, the last two terms including the correlation between the fluctuation of fluid velocity and mass loading in Eq. (5-18) are negligible (Balachandar and Eaton 2010). It should be noted that this process is only possible with heavy particles. For light neutrally buoyant particles, the spatial distribution is determined by the fluctuations of the flow, so this correlation term cannot be ignored. Additionally, in statistically homogeneous flow, the production and transport terms on the right-hand side and the advection term on the left-hand

side are close to zero due to small spatial gradients (Pope 2000). It should be noted that in this case, only the sink of TKE remains and therefore the turbulence is in a state of decay. In the case of experiments, additional momentum can be added by using a mechanical device such as a fan or synthetic jet actuator, such that the turbulence does not decay (Hwang and Eaton 2006; Tanaka and Eaton 2010). On the other hand, in the case of numerical simulation, steady-state turbulence is achieved by applying a spatially non-uniform and time-dependent body force at a low wave number (i.e. large scale of turbulence) of the velocity field. The energy generated by this artificially applied body force compensates for the inevitable turbulence kinetic energy dissipation in homogeneous turbulence, enabling a steady state (Squires and Eaton 1990; Boivin et al. 1998; Abdelsamie and Lee 2012). If the energy injected from the external source is defined as P_k, considering the aforementioned conditions, the following equation is obtained:

$$P_k - \tilde{\varepsilon} - \frac{\bar{\tilde{\Phi}}}{\tau_p}\left(\overline{\tilde{u}_i\tilde{u}_i} - \overline{\tilde{u}_i\tilde{v}_i}\right) = 0 \tag{5-19}$$

The dissipation rate $\tilde{\varepsilon}\left(\equiv \nu\overline{\left(\frac{\partial \tilde{u}_i}{\partial x_j}\frac{\partial \tilde{u}_j}{\partial x_i}\right)}\right)$ transport equation can be derived from Eq. (5-4). However, because the dissipation rate equation is much more complicated than that of the TKE, the modelled equation is often used (Elghobashi and Abou-Arab 1983; Chen and Wood 1984; Schwarzkopf et al. 2009). Therefore herein, the modelled dissipation rate transport equation was used and many terms, including mass loading fluctuations, were eliminated to arrive at the following simplified equation:

$$\frac{D\tilde{\varepsilon}}{Dt} = \frac{\partial}{\partial x_i}\left(\frac{\tilde{\nu}_T}{\tilde{\sigma}_\varepsilon}\frac{\partial \tilde{\varepsilon}}{\partial x_i}\right) + \tilde{C}_{\varepsilon_1}\frac{\tilde{\mathcal{P}}\tilde{\varepsilon}}{\tilde{k}} - \tilde{C}_{\varepsilon_2}\frac{\tilde{\varepsilon}^2}{\tilde{k}} + \frac{2\bar{\tilde{\Phi}}}{\tau_p}\left(\nu\overline{\frac{\partial \tilde{u}_i}{\partial x_j}\left(\frac{\partial \tilde{v}_i}{\partial x_j} - \frac{\partial \tilde{u}_i}{\partial x_j}\right)}\right) \tag{5-20}$$

where $\tilde{C}_{\varepsilon_1}$, $\tilde{C}_{\varepsilon_2}$, and $\tilde{\sigma}_\varepsilon$ are model coefficients and $\tilde{\nu}_T$ is the eddy viscosity. The left-hand side of the modelled equation (Eq. (5-20)) includes the rate of change of dissipation rate with respect to time and transport by advection. The first to third terms on the right-hand side represent diffusion, generation, and destruction of the dissipation rate, respectively, and the last term represents the effect of particles. Similar to the TKE equation, the first two terms on the right-hand side can be eliminated due to small spatial gradients in a statistically homogeneous flow. The equation can then be rearranged as follows:

$$P_\varepsilon - \tilde{C}_{\varepsilon_2}\frac{\tilde{\varepsilon}^2}{\tilde{k}} + \frac{2\bar{\tilde{\Phi}}}{\tau_p}\left(\nu\overline{\frac{\partial \tilde{u}_i}{\partial x_j}\left(\frac{\partial \tilde{v}_i}{\partial x_j} - \frac{\partial \tilde{u}_i}{\partial x_j}\right)}\right) = 0 \tag{5-21}$$

where P_ε is an extra source of dissipation production due to the external force.

In Eqs. (5-19) and (5-21), the effect of the particles is expressed using two terms: fluid–fluid correlation ($\overline{\tilde{u}_i\tilde{u}_i}$, $\nu\overline{\frac{\partial\tilde{u}_i}{\partial x_j}\frac{\partial\tilde{u}_i}{\partial x_j}}$) and fluid–particle correlation ($\overline{\tilde{u}_i\tilde{v}_i}$, $\nu\overline{\frac{\partial\tilde{u}_i}{\partial x_j}\frac{\partial\tilde{v}_i}{\partial x_j}}$). The first fluid–fluid correlation term ($\overline{\tilde{u}_i\tilde{u}_i}$) can be substituted with $2\tilde{k}$ in Eq. (5-19) and the second term ($\nu\overline{\frac{\partial\tilde{u}_i}{\partial x_j}\frac{\partial\tilde{u}_i}{\partial x_j}}$) with $\tilde{\varepsilon}$ in Eq. (5-21) (Danon et al. 1977; Chen and Wood 1984; Chen and Wood 1985). The fluid–particle correlation values are determined according to the dependency of the fluid and particle fluctuation velocity. In real experiments, the main force acting on heavy particles, other than drag, is gravity. If the time scale for the particle to pass through the turbulence eddy at the settling velocity is sufficiently shorter than the timescale for the particle to respond to drag, τ_p, it can be assumed that the fluctuation velocities of the particle and fluid are uncoupled. This is still valid even if the turbulence changes as the mass loading of particles increases. Even if the turbulence is greatly attenuated by the particles, the Kolmogorov lengthscale has $O(10^2 - 10^3$ μm), whereas the terminal velocity of heavy particles has O(1 m/s). Therefore, since the timescale for interaction between particles and eddy is O(0.1–1 ms), it is smaller than the timescale of heavy particles, which is ~$O(10^2$ms). In this case, the gradients of the particle and fluid fluctuation velocities are also independent of each other (Chen and Wood 1985). Then, Eqs. (5-19) and (5-21) can be expressed as follows.

$$P_k - \tilde{\varepsilon} - 2\tilde{k}\frac{\bar{\tilde{\Phi}}}{\tau_p} = 0 \tag{5-22}$$

$$P_\varepsilon - \tilde{C}_{\varepsilon_2}\frac{\tilde{\varepsilon}^2}{\tilde{k}} - 2\tilde{\varepsilon}\frac{\bar{\tilde{\Phi}}}{\tau_p} = 0 \tag{5-23}$$

We can derive a similar equation for the particle-free pre-unladen turbulence state. Starting from Eq. (5-3), using the Navier–Stokes equation in the absence of particles and applying the same method to derive Eqs. (5-22) and (5-23), the following equations are obtained:

$$P_k - \varepsilon_0 = 0 \tag{5-24}$$

$$P_\varepsilon - C_{\varepsilon_2}\frac{\varepsilon_0^2}{k_0} = 0 \tag{5-25}$$

where subscript 0 indicates the physical quantity of the particle-free state, C_{ε_2} is the model coefficient for turbulent flow without particles, and P_k and P_ε have the same values as in Eqs. (5-22) and (5-23) because the energy supplied before and after particle addition remains the same for both experiments and simulations.

Thus, we have obtained four equations, Eqs. (5-22) – (5-25), wherein ρ_f, τ_p, and $\bar{\bar{\Phi}}$ are determined by the working fluid, particle, and number of injected particles, respectively. If the initial turbulence characteristics and the physical properties of the particle are known, the equation contains a total of six unknown parameters (P_k, P_ε, $\tilde{C}_{\varepsilon_2}$, C_{ε_2}, $\tilde{k}$, $\tilde{\varepsilon}$), which results in a closure problem. To close the equation, we need more information about two of these. A commonly used value for C_{ε_2} in Eq. (5-25) is 1.92, and some studies have used the same value for $\tilde{C}_{\varepsilon_2}$ in Eq. (5-23) (Chen and Wood 1984; Chen and Wood 1985; Lightstone and Hodgson 2004). However, other studies have argued that $\tilde{C}_{\varepsilon_2}$ changes with particle mass loading and τ_p (Squires and Eaton 1994). Herein, $\tilde{C}_{\varepsilon_2} = C_{\varepsilon_2} = 1.92$ was used and the details are discussed later. Since we now have four equations with four unknown parameters (P_k, P_ε, $\tilde{k}$, $\tilde{\varepsilon}$), we can solve the problem.

P_k and P_ε in Eqs. (5-22) and (5-23) can be replaced with ε_0 and $C_{\varepsilon_2}\varepsilon_0^2/k_0$, respectively, using Eqs. (5-24) and (5-25). Thus, Eqs. (5-22) and (5-23) can be rearranged as follows:

$$\varepsilon_0 - \tilde{\varepsilon} - C_0\tilde{k} = 0 \tag{5-26}$$

$$C_{\varepsilon_2}\frac{\varepsilon_0^2}{k_0} - \tilde{C}_{\varepsilon_2}\frac{\tilde{\varepsilon}^2}{\tilde{k}} - C_0\tilde{\varepsilon} = 0 \tag{5-27}$$

where C_0 is defined as $2\bar{\bar{\Phi}}/\tau_p$. Under the conditions that $\tilde{k} \neq 0$ and $C_{\varepsilon_2}\varepsilon_0^2/k_0 - C_0\tilde{\varepsilon} \neq 0$, Eq (5-27) can be transformed as follows:

$$\tilde{k} = \tilde{C}_{\varepsilon_2}\tilde{\varepsilon}^2/(C_{\varepsilon_2}\varepsilon_0^2/k_0 - C_0\tilde{\varepsilon}) \tag{5-28}$$

In this equation, if no particles are laid in turbulence, $C_0 = 0$, and $\tilde{C}_{\varepsilon_2} \to C_{\varepsilon_2}$ are satisfied, then $\tilde{k} = k_0$, which is physically reasonable.

Next, (5-28) was substituted into Eq. (5-26) to obtain a solution for the dissipation rate.

$$C_0(1 - \tilde{C}_{\varepsilon_2})\tilde{\varepsilon}^2 - (C_{\varepsilon_2}\varepsilon_0^2/k_0 + C_0\varepsilon_0)\tilde{\varepsilon} + C_{\varepsilon_2}\varepsilon_0^3/k_0 = 0 \tag{5-29}$$

If $C_0\left(1 - \tilde{C}_{\varepsilon_2}\right) \neq 0$, the above equation becomes a quadratic equation for $\tilde{\varepsilon}$. Therefore, $\tilde{\varepsilon}$ can be calculated as follows:

$$\tilde{\varepsilon} = \frac{(C_{\varepsilon_2}\varepsilon_0^2/k_0 + \varepsilon_0 C_0) \pm \sqrt{(C_{\varepsilon_2}\varepsilon_0^2/k_0 + \varepsilon_0 C_0)^2 - 4(1 - \tilde{C}_{\varepsilon_2})C_0 C_{\varepsilon_2}\varepsilon_0^3/k_0}}{2(1 - \tilde{C}_{\varepsilon_2})C_0} \tag{5-30}$$

If $\tilde{C}_{\varepsilon_2} \approx C_{\varepsilon_2} = 1.92$, the denominator is always negative. Because the first term of

the numerator, $\left(C_{\varepsilon_2}\varepsilon_0^2/k_0 + \varepsilon_0 C_0\right)$, is always positive, the ± sign of the numerator must be changed to negative for $\tilde{\varepsilon}$ to be positive. For the particle-free condition, $\tilde{\varepsilon} = \varepsilon_0$ can be obtained by substituting $C_0 = 0$ into Eq. (5-29).

In summary, the dissipation rate and TKE are expressed as follows, respectively:

$$\tilde{\varepsilon} = \frac{(C_{\varepsilon_2}\varepsilon_0^2/k_0 + \varepsilon_0 C_0) - \sqrt{(C_{\varepsilon_2}\varepsilon_0^2/k_0 + \varepsilon_0 C_0)^2 - 4(1-\tilde{C}_{\varepsilon_2})C_0 C_{\varepsilon_2}\varepsilon_0^3/k_0}}{2(1-\tilde{C}_{\varepsilon_2})C_0} \quad \text{for} \quad (1-\tilde{C}_{\varepsilon_2})C_0 \neq 0 \tag{5-31}$$

$$\tilde{k} = \frac{\tilde{C}_{\varepsilon_2}\tilde{\varepsilon}^2}{(C_{\varepsilon_2}\varepsilon_0^2/k_0 - C_0\tilde{\varepsilon})} \tag{5-32}$$

where C_0 is defined as $2\bar{\bar{\Phi}}/\tau_p$. These equations only contain information regarding the initial turbulence state (k_0, ε_0) and the dispersed phase ($\bar{\bar{\Phi}}$, τ_p). Therefore, the modified turbulence characteristics can be predicted from the initial turbulence state and particle properties, unlike previous models which could not properly predict the turbulence modulation.

This equation can also be transformed into a form that includes the Stokes number, which is known to be an important parameter in particle-laden turbulence. Dividing both sides of Eq. (5-30) by ε_0 transforms the equation into:

$$\tilde{\varepsilon}/\varepsilon_0 = \frac{(C_{\varepsilon_2}\varepsilon_0/k_0 + C_0) - \sqrt{(C_{\varepsilon_2}\varepsilon_0/k_0 + C_0)^2 - 4(1-\tilde{C}_{\varepsilon_2})C_0 C_{\varepsilon_2}\varepsilon_0/k_0}}{2(1-\tilde{C}_{\varepsilon_2})C_0} \tag{5-33}$$

Here, using the turbulence Reynolds number for particle pre-unladen turbulence, $Re_L = k_0^2/(\varepsilon_0 \nu)$, ε_0/k_0 included in the above equation can be re-expressed as:

$$\varepsilon_0/k_0 = \frac{1}{Re_L}\left(\frac{\varepsilon_0}{\nu}\right)^{1/2} = \frac{1}{Re_L}\frac{1}{\tau_\eta} \tag{5-34}$$

where τ_η is Kolmogorov timescale. After substituting Eq. (5-34) into Eq. (5-33) and multiplying the numerator and denominator by τ_p, we can get the following equation.

$$\tilde{\varepsilon}/\varepsilon_0 = \frac{(C_{\varepsilon_2}St_k/Re_L + 2\bar{\bar{\Phi}}) - \sqrt{(C_{\varepsilon_2}St_k/Re_L + 2\bar{\bar{\Phi}})^2 - 8\bar{\bar{\Phi}}(1-\tilde{C}_{\varepsilon_2})C_{\varepsilon_2}St_k/Re_L}}{4\bar{\bar{\Phi}}(1-\tilde{C}_{\varepsilon_2})} \tag{5-35}$$

This equation only contains three dimensionless numbers: pre-unladen turbulence Reynolds number, particle mass loading, and Stokes number.

Using the model equation derived so far, it can be useful to find the critical mass loading where modulation of the turbulence caused by the particles is beyond a negligible level (e.g. whether the particle/turbulence interaction is one- or two-way coupling). Assuming that the threshold for 'negligible' modulation is defined by the

amount of change in the dissipation rate and if this value is T (i.e. $\tilde{\varepsilon}/\varepsilon_0 = T$), it can be calculated using Eq. (5-31) as follows:

$$\tilde{\varepsilon}/\varepsilon_0 = \frac{(C_{\varepsilon_2}\varepsilon_0/k_0 + C_0) - \sqrt{(C_{\varepsilon_2}\varepsilon_0/k_0 + C_0)^2 - 4(1-\tilde{C}_{\varepsilon_2})C_0 C_{\varepsilon_2}\varepsilon_0/k_0}}{2(1-\tilde{C}_{\varepsilon_2})C_0} = T \qquad (5\text{-}36)$$

Using the fact that $C_0 = 2\bar{\bar{\Phi}}/\tau_p$, we can rearrange the above expression for critical mass loading $\bar{\bar{\Phi}}_T$,

$$\bar{\bar{\Phi}}_T = \frac{\tau_p}{2}\left(1 - \frac{1}{T}\right)\frac{C_{\varepsilon_2}\varepsilon_0/k_0}{T(1-\tilde{C}_{\varepsilon_2}) - 1} \qquad (5\text{-}37)$$

If $T = 1$, the mass loading calculated by Eq. (5-37) is 0, and thus it is physically reasonable. We can also calculate the critical mass loading for real experimental data. By substituting the conditions of the HE1 experiment into Eq. (5-37) and using $T = 0.99$ and $\tilde{C}_{\varepsilon_2} \approx C_{\varepsilon_2} = 1.92$ (this is reasonable as it is near the critical point of turbulence modulation), the critical mass loading becomes 0.003. Converting this to a volume fraction, it is about 1.6×10^{-6}, which is similar to the threshold level for dividing one- and two-way coupling (1.0×10^{-6}) proposed by Elghobashi (1994); (2006)

It should be noted that Eq. (5-31) and (5-32) are derived under conditions of a dilute system with small and heavy particles. In dense flow, the dynamics are more complicated because particle-particle collisions or contact becomes dominant, and the prediction model cannot be expressed in a simplified way. We used small and heavy assumptions to simplify the equations in the above derivation process. Here, 'small' particle means that the particle diameter is comparable to or smaller than the Kolmogorov length scale. A heavy particle has a Stokes number of about 10 or more to be uniformly distributed in space, and the settling parameter of the particle (i.e. ratio of particle terminal velocity to fluid fluctuation velocity) is 5 or more, which corresponds to a particle that settles down fairly quickly. Although the applicable range of the model is somewhat limited, these conditions can be easily found in natural or engineering applications (Hwang and Eaton 2006). Therefore, many simulations and experimental studies have previously been conducted within this scope, and this study is an extension of those studies.

Experimental data obtained in isotropic turbulence were used to validate the model. Three previous studies were considered and their experimental conditions are summarized in Table 5-1. In this table, η_0 is the Kolmogorov length scale in particle-free turbulence. $\bar{\bar{\Phi}}_{\max}$ and $\mathcal{C}_{\max}$ represent the maximum mass and volumetric

loading used in experiments, respectively. Hwang and Eaton (2006) and Tanaka and Eaton (2010) utilized isotropic turbulence generated by synthetic jets in a confined chamber, while varying the glass particle size and initial turbulence intensity. The rms velocity generated by their equipment is fairly small compared to the speed of sound, and thus the model equation derived under incompressible flow conditions can be applied. Poelma et al. (2007) injected ceramic particles into decaying turbulence using a water tunnel. Using these experimental data, Eqs. (5-31) and (5-32) can be used to confirm whether an accurate prediction is possible depending on the initial turbulence state and particle conditions.

Fig. 5-5 shows the experimental results of the previous studies and the theoretical results calculated using Eqs. (5-31) and (5-32). Fig. 5-5 (a) shows the change in dissipation rate normalized to the pre-unladen quantities of each test. The data from Poelma et al. (2007) was excluded because they did not report the dissipation rate of the corresponding experimental case. The results calculated using Eq. (5-31) showed that the HE1 case decreased slightly less than the HE2 case as the particle mass loading increased, similar in trend to the experimental results.

In the T&E study, the intensity of the initial turbulence is much higher and the particles are larger than those of the H&E study. Differences in experimental conditions caused the dissipation rate to decrease less in the TE cases, compared to the HE cases. This trend is also clearly reflected in the proposed model which predicts the overall attenuation trend in the experimental data quite well, except for the outlying largest mass loading case of TE2 which showed augmentation. The augmentation of dissipation rate for this case is not predicted well due to the underlying assumptions of the model. The augmentation of dissipation rate is likely due to the high shear of tangential velocity that occurs at the particle surface, and the effect greatly increases as the number of particles in the flow increases (Burton and Eaton 2005; Vreman 2016). Because Tanaka and Eaton (2010) measured particle-turbulence interactions with sub-Kolmogorov scale resolution, their data could possibly observe this effect. However, the point particle approach used to derive our model cannot consider microscale effects such as no-slip at the particle surface.

Fig. 5-5(b) shows the change in normalized TKE according to particle mass loading. Although there are some differences in absolute TKE value between the model and experimental results, the model is useful for predicting trends. The difference is notable in the cases of HE2 and TE2, especially at the highest mass loading of HE2. However, this data point could possibly have some experimental error, considering the sudden crossover in trends with the HE1 case. In the case of

TE2, some of the experimental data display slight turbulence augmentation, whereas the model decreases monotonically. One of the reasons turbulence enhancement might be occurring is the wake and vortex shedding behind the particles (Balachandar and Eaton 2010). The size of the large particles used in TE2 is about 4.5 times larger than that of the Kolmogorov length scale, and the particle Reynolds number reaches up to 134. These conditions are sufficient for a wake to develop around the particle (Bagchi and Balachandar 2004). However, the underlying small and heavy particle assumption in the current model does not reflect this effect, which is likely the cause of the difference between the experiment. In the case of PW&O, where the experiment was performed in a water tunnel, the TKE decreased very rapidly at low mass loading. Although the turbulence decays downstream in the water tunnel and there is only one data point to compare with, the model properly captures this and alludes to additional strong modulation at low mass loading.

To figure out the reason for the deviation between the experimental results and model, it is necessary to reexamine Eqs. (5-22) – (5-25) used to derive Eqs. (5-31) and (5-32). Instead of solving the four equations at once, we can solve each transport equation separately. By combining the pre-unladen and particle-laden states of the TKE transport equations, Eqs. (5-22) and (5-24), and dissipation rate equation, Eqs. (5-23) and (5-25), respectively, we obtain Eqs. (5-38) and (5-39):

$$\tilde{\varepsilon} = -2\tilde{k}\,\bar{\tilde{\Phi}}/\tau_p + \varepsilon_0 \tag{5-38}$$

$$\tilde{\varepsilon} = \frac{-\bar{\tilde{\Phi}} + \sqrt{\bar{\tilde{\Phi}}^2 + C_{\varepsilon_2}\tilde{C}_{\varepsilon_2}\tau_p^2\varepsilon_0^2/(k_0\tilde{k})}}{\tau_p\tilde{C}_{\varepsilon_2}}\tilde{k} \tag{5-39}$$

These equations show the relationship between the modulated dissipation rate and TKE. By comparing the trends of these two equations with the experimental results, it is possible to determine which equation is more accurate.

Fig. 5-6 (a) shows the results obtained by applying Eqs. (5-38) and (5-39) to HE1. The results for the other cases (Fig. 5-7) have similar trends. For comparison, we plotted trends from models proposed by Kulick et al. (1994) (KF&E) and Tanaka and Eaton (2010) (TE). Using the KF&E and TE models, the dissipation rate was underestimated when compared with the experimental results. The results calculated using Eqs. (5-38) and (5-39) show higher accuracy than the previous models. Comparing the two equations, the result calculated by Eq. (5-38) is more accurate than that of Eq. (5-39) because Eq. (5-39) is obtained using the dissipation rate transport equation. Unlike the TKE transport equation, the equation for the dissipation rate was derived using a modelled form. If the two model coefficients,

C_{ε_2} and $\tilde{C}_{\varepsilon_2}$, are set incorrectly, the result can be somewhat erroneous.

Herein, we used $C_{\varepsilon_2} = \tilde{C}_{\varepsilon_2} = 1.92$ when calculating the model equation. However, as mentioned above, Squires and Eaton (1994) showed that the model coefficient changes for turbulent flow in the presence of particles. Unfortunately, the conditions in their simulations (e.g., absence of gravitational force and low Stokes number) were very different to those of the previous experiments. Therefore, it is difficult to apply a correction for $\tilde{C}_{\varepsilon_2}$ based on their data. Instead, we show that the performance of the proposed model can be improved by adjusting $\tilde{C}_{\varepsilon_2}$ as follows.

We assume that $\tilde{C}_{\varepsilon_2}$ has a linearly proportional relationship with mass loading ($\tilde{C}_{\varepsilon_2} = C\bar{\bar{\Phi}} + C_{\varepsilon_2}$), based on the study of Squires and Eaton (1994). Although the simulation conditions are different from those of H&E, $\tilde{C}_{\varepsilon_2}$ was shown to have a roughly linear relation with mass loading for different particle timescales. In order to reach a clear conclusion whether this coefficient is linear with mass loading under experimental conditions of H&E, simulations under a wide range of conditions should be conducted in future studies. Because this section intends to demonstrate that the prediction accuracy of TKE or dissipation rate can be improved by changing $\tilde{C}_{\varepsilon_2}$, a linear correlation assumption is used. Because $\tilde{C}_{\varepsilon_2}$ is affected by τ_p, the same corrected $\tilde{C}_{\varepsilon_2}$ was applied to the data from HE1 and HE2, which used the same particle. Fig. 5-6 (b) shows the experimental results and model calculated from Eqs. (5-31) and (5-32) when $C = 3$. Note that this value was arbitrarily chosen to show the effect of the coefficient. Comparing with the case where $C = 0$ (i.e., $\tilde{C}_{\varepsilon_2} = C_{\varepsilon_2}$), see Fig. 5-5 (b), it can be seen that the model prediction becomes more accurate for both experimental cases except for the highest mass loading of HE2. As mentioned above, this value can possibly contain some error considering the crossover in trends with the HE1 case. In any case, it is clear that more experimental data on isotropic turbulence are needed to make clear conclusions about the validity and accuracy of the various assumptions used in this model.

In summary, we present a model for predicting particle-induced turbulence attenuation in isotropic turbulence. Developing such a model is important in providing clues on factors affecting particle–turbulence interactions that have not yet been fully elucidated. The model obtained by combining the TKE and dissipation rate transport equations for the pre-unladen and particle-laden states can predict the modulated TKE and dissipation rate using the initial turbulence state and particle properties. When the proposed models were applied to previous experiments

performed in stationary and decaying isotropic turbulence, the modification trend is predicted considerably well. The discrepancies between the model and experimental data most likely arise from the modelled dissipation rate transport equation. To improve the performance of the prediction model, more information on the model coefficients is required. Accordingly, additional experiments on particle-laden isotropic turbulence should be conducted in the future to provide further validation of the model.

5.2.2. Experimental verification

In this section, the various assumptions used when deriving the model in Section 5.2.1 are validated with experimental data. The model presented by Lee and Hwang (2022) begins with the TKE and dissipation rate transport equations. These equations can be derived by adding a particle-fluid momentum exchange term to the Navier–Stokes equation. In particle-laden turbulence, the two transport equations are expressed as

$$\begin{aligned}\rho_f\left(\frac{\partial\tilde{k}}{\partial t}+\bar{\tilde{U}}_i\frac{\partial\tilde{k}}{\partial x_i}\right)&=-\rho_f\overline{\tilde{u}_i\tilde{u}_j}\frac{\partial\bar{\tilde{U}}_i}{\partial x_j}-\rho_f\tilde{\varepsilon}\\&+\frac{\partial}{\partial x_j}\overline{\tilde{u}_i\tilde{\tau}'_{ij}}-\frac{1}{2}\frac{\partial}{\partial x_j}\rho_f\overline{\tilde{u}_i\tilde{u}_i\tilde{u}_j}-\frac{\partial}{\partial x_i}\overline{\tilde{u}_i\tilde{p}}\\-\frac{\rho_f\bar{\tilde{\Phi}}}{\tau_p}\left(\overline{\tilde{u}_i\tilde{u}_i}-\overline{\tilde{u}_i\tilde{v}_i}\right)&-\frac{\rho_f}{\tau_p}\left(\overline{\tilde{\phi}\tilde{u}_i\tilde{u}_i}-\overline{\tilde{\phi}\tilde{u}_i\tilde{v}_i}\right)-\frac{\rho_f}{\tau_p}\overline{\tilde{u}_i\tilde{\phi}}\left(\bar{\tilde{U}}_i-\bar{\tilde{V}}_i\right)+P_k\end{aligned}\tag{5-40}$$

$$\begin{aligned}\frac{\partial\tilde{\varepsilon}}{\partial t}+\bar{\tilde{U}}_i\frac{\partial\tilde{\varepsilon}}{\partial x_i}&=\frac{\partial}{\partial x_i}\left(\frac{\tilde{\nu}_T}{\tilde{\sigma}_\varepsilon}\frac{\partial\tilde{\varepsilon}}{\partial x_i}\right)-\tilde{C}_{\varepsilon_1}\overline{\tilde{u}_i\tilde{u}_j}\frac{\partial\bar{\tilde{U}}_i}{\partial x_j}\frac{\tilde{\varepsilon}}{\tilde{k}}-\tilde{C}_{\varepsilon_2}\frac{\tilde{\varepsilon}^2}{\tilde{k}}\\+\frac{2\nu_f}{\tau_p}&\left(\overline{\frac{\partial\tilde{u}_i}{\partial x_j}\frac{\partial\bar{\tilde{\Phi}}}{\partial x_j}(\tilde{u}_i-\tilde{v}_i)}+\bar{\tilde{\Phi}}\,\overline{\frac{\partial\tilde{u}_i}{\partial x_j}\left(\frac{\partial\tilde{v}_i}{\partial x_j}-\frac{\partial\tilde{u}_i}{\partial x_j}\right)}\right)+\mathfrak{F}(\tilde{\phi})+P_\varepsilon\end{aligned}\tag{5-41}$$

where $\sim$ denotes physical quantities in particle-laden turbulence, and the overbar denotes the Reynolds average. u, v, p, τ', and ϕ are fluctuation components of the fluid and particle velocities, pressure, shear stress, and mass loading, respectively. The subscripts i and j denote the i- and j-direction components, respectively. Eq. (5-41) is a model form of the dissipation rate transport equation. This model equation is often used because the full equation is very complex for particle-laden turbulence (Chen and Wood 1984; Chen and Wood 1985; Kulick et al. 1994; Lee and Hwang 2022). In this equation, $\tilde{\nu}_T$ denotes the eddy viscosity, and $\tilde{\sigma}_\varepsilon$, $\tilde{C}_{\varepsilon_1}$, and $\tilde{C}_{\varepsilon_2}$ are model coefficients. $\mathfrak{F}(\tilde{\phi})$ represents a correlation term that includes mass loading fluctuations. $\mathcal{P}_k$ and $\mathcal{P}_\varepsilon$, the last terms in Eqs. (5-40) and (5-41), denote the

production of TKE and dissipation rate injected from the external momentum source (i.e., the woofer speaker in this study). Lee and Hwang (2022) obtained these values from the transport equations for pre-unladen turbulence and calculated them as $\rho_f \varepsilon_0$ and $C_{\varepsilon_2}\varepsilon_0^2/k_0$, respectively. Here, C_{ε_2} is a model coefficient for pre-unladen turbulence, and has been assigned the value of 1.92, following previous studies (Pope 2000).

This dissipation rate transport equation can be simplified under specific conditions. Kulick et al. (1994) and Balachandar and Eaton (2010) argued that the correlation term $\mathfrak{F}(\tilde{\phi})$, which includes the mass loading fluctuation ($\tilde{\phi}$), is negligible for large Stokes numbers where the spatial distribution of particles is uniform (Wood et al. 2005). This is because heavy particles with a large Stokes number do not follow the surrounding flow and settle down while maintaining a uniform distribution, as shown in Fig. 5-8 (a). In this case, within the ROI represented by the dotted red box, the concentration of particles with time does not change significantly and remains almost constant. Thus, the particle mass loading fluctuation appears small. On the other hand, as shown in Fig. 5-8 (b), in the case of a low Stokes number, the spatial distribution of particles reacts sensitively to turbulent eddies and shows a preferential concentration. This results in a significant increase in $\tilde{\phi}$ and $\overline{\tilde{\phi}\tilde{u}_i}$ within the region of interest.

The particles used in this study had a large Stokes number based on the Kolmogorov time scale (St_k) of ~$O(10)$. Thus, it is expected to have a uniform distribution in space. We quantified the particle spatial distribution using the box-counting method and Voronoi analysis. First, box-counting method was applied. This method divides the ROI into certain size boxes, counts the number of particles contained in each box, and expresses it as a distribution (Monchaux et al. 2012). When the spatial distribution of the particles is uniform, it follows a Poisson distribution (Wood et al. 2005; Monchaux et al. 2012). Fig. 5-9 shows the distribution obtained by this method for the three mass-loading cases of our experiment. For comparison, the corresponding Poisson distributions are also shown in the graph. The experimental data matched the Poisson distribution fairly well in all three cases.

Next, we also performed an analysis using the Voronoi diagram. Monchaux et al. (2012) pointed out that it is difficult to identify or characterize clusters and voids of particles with the box-counting method, and showed that better analysis is possible through Voronoi diagrams. Fig. 5-10 (a) is an example of applying the Voronoi

diagram to the highest mass loading experiment case. In the figure, a black dot represents the center point of a particle, and colored hollow circles represent each vertex of a Voronoi cell. For comparison, Fig. 5-10 (b) shows the results of application to synthetic data which randomly distributed same number of particles in image. It can be confirmed that these two appear similar in visual inspection. For quantitative analysis, the PDF of the area of each Voronoi cell is shown in Fig. 5-11. Compared to the random Poisson process (RPP) case, in which the particles are randomly distributed in space, the experiment and RPP results appear almost collapsed. That is, in the experiment, it can be inferred that the particles are uniformly distributed in the space. Based on these facts, the terms containing $\tilde{\phi}$ in Eqs. (5-40) and (5-41) are deemed to have a negligible effect.

It should be noted that the second last term on the right-hand side of Eq. (5-40) is not the particle potential energy transfer. The terms related to particle potential energy (PPE) can be found in the mean kinetic energy (MKE) transport equation. MKE equation can be obtained by multiplying Eq. (5-15) by the fluid mean velocity:

$$\frac{\rho_f}{2}\left(\frac{\partial \bar{\tilde{U}}_i^2}{\partial t}+\bar{\tilde{U}}_j\frac{\partial \bar{\tilde{U}}_i^2}{\partial x_j}\right)=\rho_f\overline{\tilde{u}_i\tilde{u}_j}\frac{\partial \bar{\tilde{U}}_i}{\partial x_j}-\bar{\tilde{\tau}}_{ij}\frac{\partial \bar{\tilde{U}}_i}{\partial x_j}-\frac{\partial(\bar{\tilde{U}}_i\bar{\tilde{P}})}{\partial x_i}+\frac{\partial(\bar{\tilde{U}}_i\bar{\tilde{\tau}}_{ij})}{\partial x_j}-\rho_f\frac{\partial(\bar{\tilde{U}}_i\overline{\tilde{u}_i\tilde{u}_j})}{\partial x_j}$$
$$\underbrace{-\frac{\rho_f}{\tau_p}\bar{\tilde{U}}_i\bar{\tilde{\Phi}}(\bar{\tilde{U}}_i-\bar{\tilde{V}}_i)}_{particle\ potential\ energy}-\frac{\rho_f}{\tau_p}\bar{\tilde{U}}_i\left(\overline{\tilde{u}_i\tilde{\phi}}-\overline{\tilde{v}_i\tilde{\phi}}\right) \tag{5-42}$$

The second term from the right-hand side of this equation is the term related to the potential energy of particles. Part of this energy term is transferred through the wake to the turbulence kinetic energy (TKE), which is discussed in detail in Section 5.2.3

Equations (5-40) and (5-41) can be further simplified assuming homogeneity and steady-state conditions. In this experiment, uniformly distributed particles were injected into the homogeneous turbulence. The modulated turbulence is also expected to be homogeneous. The mean flow of the particle-laden turbulence appears to be almost uniform within the ROI, as shown in Fig. 5-2 (b), suggesting that the flow is relatively homogeneous. This homogeneity causes spatial gradients of statistical values to become small, allowing us to neglect such terms. In addition, during the experiment, the speaker supplies constant energy to the turbulent flow while maintaining the intensity, and the mass loading of the particles is also kept constant. Under these conditions, the flow can be considered at steady state, allowing us to eliminate the unsteady terms. Therefore, under the conditions of uniform particle distribution, homogeneity, and steady-state flow, Eqs. (5-40) and (5-41) can be simplified as follows:

$$-\tilde{\varepsilon} - \frac{\bar{\tilde{\Phi}}}{\tau_p}(\overline{\tilde{u}_i\tilde{u}_i} - \overline{\tilde{u}_i\tilde{v}_i}) + \varepsilon_0 = 0 \tag{5-43}$$

$$-\tilde{C}_{\varepsilon_2}\frac{\tilde{\varepsilon}^2}{\tilde{k}} + \frac{2\bar{\tilde{\Phi}}\nu_f}{\tau_p}\left(\overline{\frac{\partial\tilde{u}_i}{\partial x_j}\left(\frac{\partial\tilde{v}_i}{\partial x_j} - \frac{\partial\tilde{u}_i}{\partial x_j}\right)}\right) + C_{\varepsilon_2}\varepsilon_0^2/k_0 = 0 \tag{5-44}$$

Eqs. (5-43) and (5-44) include the correlation of the fluctuation velocities (or their gradients). Kulick et al. (1994) and Hwang and Eaton (2006) assumed that the fluid–particle correlation ($\overline{\tilde{u}_i\tilde{v}_i}$) would be small because particles with high St_k cannot respond to the flow. Using their assumption, Lee and Hwang (2022) simplified Eqs. (5-43) and (5-44) as follows:

$$-\tilde{\varepsilon} - \frac{2\tilde{k}\bar{\tilde{\Phi}}}{\tau_p} + \varepsilon_0 = 0 \tag{5-45}$$

$$-\tilde{C}_{\varepsilon_2}\frac{\tilde{\varepsilon}^2}{\tilde{k}} - \frac{2\bar{\tilde{\Phi}}\tilde{\varepsilon}}{\tau_p} + C_{\varepsilon_2}\varepsilon_0^2/k_0 = 0 \tag{5-46}$$

To validate this assumption, we calculated the angle between the fluctuation velocities of the particle and fluid. If the two velocity vectors are independent of each other, as assumed in previous studies, the angle between them will be random. Fig. 5-12 shows the PDF of the calculated angle. The probability was highest when the vectors were aligned and decreased as they became misaligned. There was little difference between the three mass loadings. Thus, the fluid–particle correlation term may have a considerably greater effect than expected in previous studies.

To estimate the effect of this fluid–particle correlation term, we compared it with the fluid–fluid correlation ($\overline{\tilde{u}_i\tilde{u}_i}$). Fig. 5-13 (a) shows the two correlation terms according to mass loading. In all cases, the magnitude of $\overline{\tilde{u}_i\tilde{v}_i}$ was approximately 25% of that of $\overline{\tilde{u}_i\tilde{u}_i}$. Hence, although $\overline{\tilde{u}_i\tilde{v}_i}$ is relatively small, it cannot be neglected. Various previous studies have expressed the correlation terms in Eqs. (5-43) and (5-44) as a model, as illustrated in Table 5-4. Each model utilizes different physical scales. We compared the ratio between fluid–particle correlation and fluid-fluid correlation from these models with our experimental results, as shown in Fig. 5-13 (b). The constants in the model were obtained from the relevant studies, except for the case of Danon et al. (1977), where the constant values were not specified and hence were excluded from the plot. The model proposed by Mostafa and Mongia (1988) is closest to our results. Therefore, by substituting their model into Eqs. (5-43) and (5-44), we obtain the following:

$$-\tilde{\varepsilon} - \frac{2\tilde{k}\bar{\tilde{\Phi}}}{\tau_p}\left(1 - \frac{0.35\tilde{k}/\tilde{\varepsilon}}{0.35\tilde{k}/\tilde{\varepsilon} + \tau_p}\right) + \varepsilon_0 = 0 \tag{5-47}$$

$$-\tilde{C}_{\varepsilon_2}\frac{\tilde{\varepsilon}^2}{\tilde{k}} - \frac{2\bar{\tilde{\Phi}}\tilde{\varepsilon}}{\tau_p}\left(1 - \frac{0.35\tilde{k}/\tilde{\varepsilon}}{0.35\tilde{k}/\tilde{\varepsilon} + \tau_p}\right) + C_{\varepsilon_2}\varepsilon_0^2/k_0 = 0 \tag{5-48}$$

5.2.3. Finite-size particle effect

Eqs. (5-47) and (5-48) are more comprehensive than Eqs. (5-45) and (5-46), as they additionally consider the effect of the fluid–particle correlation term. However, these equations still have some limitations. They were developed from transport equations using the point-particle approach, which assumes that turbulent wakes and no-slip boundary conditions at the particle surface can be neglected. Particle-induced wakes are considered the main reason for turbulence augmentation, and the flow distortion near the surface due to no-slip conditions is known to generate large additional dissipation (Balachandar and Eaton 2010). These can affect turbulence modulation considerably, and therefore should be additionally considered in the model.

A model that included particle-induced wakes was proposed by Yokomine and Shimizu (1995). They decomposed the source term in the particle-laden MKE equation into two parts—the energy dissipated as heat and the energy transferred to the turbulence by the wake. Using the fact that a wake behind the particle occurs only in a non-Stokes flow, they calculated the energy transferred from the MKE to TKE as follows:

$$\mathcal{P}_w = \left|\bar{\tilde{U}}\,\bar{\tilde{\Phi}}(\bar{\tilde{U}} - \bar{\tilde{V}})(f-1)/\tau_p\right| \approx \left|\bar{\tilde{U}}\,\bar{\tilde{\Phi}}g(f-1)\right| \tag{5-49}$$

This approach was used in several subsequent studies (Yokomine et al. 2002; Yan et al. 2007). The approximation in Eq. (5-49) is due to the assumption $|\bar{\tilde{U}} - \bar{\tilde{V}}| \approx \tau_p g$.

Next, additional dissipation due to the no-slip boundary condition on the particle surface should be considered. Vreman (2016) and Burton and Eaton (2005) studied turbulence modulation by fixed particles in isotropic turbulence through PR-DNS. Both studies reported a rapid increase in the TKE dissipation rate at the particle surface owing to the no-slip boundary condition. This phenomenon has been observed not only in simulations but also in experiments. Tanaka and Eaton (2010) showed that the dissipation rate increased more than threefold around finite-size particles using PIV with sub-Kolmogorov resolution. A perfect model for the additional dissipation near the particle surface is not available yet. Hence, we employed the rough estimation of Vreman (2016) as follows:

$$\varepsilon_b(r_p) = 6\nu_f(fU_\infty/d_p)^2 \tag{5-50}$$

where r_p denotes the radius of the particle, ε_b is the additional dissipation caused by the boundary effect, and U_∞ is the free-stream velocity. In this study, it is reasonable to approximate U_∞ as the mean relative velocity of the particle and fluid ($U_\infty \approx \left|\overline{\tilde{U}} - \overline{\tilde{V}}\right|$) because the particles rapidly settle due to gravity. In addition, $\left|\overline{\tilde{U}} - \overline{\tilde{V}}\right|$ can be approximated with $\tau_p g$, and hence U_∞ can be substituted with $\tau_p g$. We also introduce the assumption that the dissipation rate decreases exponentially with distance from the particle surface. Thus, the dissipation rate surrounding a particle can be expressed as follows:

$$\varepsilon_b(r_p) = 6\nu_f (f\tau_p g/d_p)^2 \, e^{-d(r/r_p - 1)} \tag{5-51}$$

where d is a constant that determines the spatial decay of the dissipation rate. If $r = r_p$, this equation becomes Eq. (5-50), and if $r \to \infty$, it becomes zero. Using Eq. (5-51), the additional dissipation caused by N_p particles per unit volume ($\mathcal{V}_f$) can be calculated as follows:

$$\mathcal{D}_b = \frac{N_p}{\mathcal{V}_f} \int_{r_p}^{\infty} 4\pi^2 \varepsilon_b(r) dr = f\tau_p \bar{\tilde{\Phi}} g^2 \frac{d(d+2)+2}{d^3} \tag{5-52}$$

By adding the values of $\mathcal{P}_w$ and $\mathcal{D}_b$ obtained from Eqs. (5-49) and (5-52) into Eq. (5-47), the final TKE equation can be obtained (in implicit form) which considers wakes and additional dissipation caused by the particles:

$$-\tilde{\varepsilon} + \varepsilon_0 - \frac{2\tilde{k}\bar{\tilde{\Phi}}}{\tau_p}\left(1 - \frac{0.35\tilde{k}/\tilde{\varepsilon}}{0.35\tilde{k}/\tilde{\varepsilon} + \tau_p}\right) + |\bar{\tilde{U}}\bar{\tilde{\Phi}} g(f-1)| - f\tau_p \bar{\tilde{\Phi}} g^2 \frac{d(d+2)+2}{d^3} = 0 \tag{5-53}$$

Unfortunately, it is difficult to add the terms that consider these effects to the dissipation rate transport equation. The term representing the destruction of dissipation owing to wakes or particle surface boundary effects has not been studied before; therefore, a simple model such as Eq. (5-50) does not exist. Hence, in this study, only the TKE transport equation was considered.

The model equations obtained thus far included several constants. To compute the equations, two constants must be determined: $\tilde{C}_{\varepsilon_2}$ and d. First, $\tilde{C}_{\varepsilon_2}$ from Eqs. (5-44) and (5-46) were considered. This is the modulated model coefficient for particle-laden turbulence. In several previous studies, $\tilde{C}_{\varepsilon_2}$ was assigned the value of 1.92, similar to C_{ε_2} (Chen and Wood 1984; Chen and Wood 1985). In contrast, Squires and Eaton (1994) showed that $\tilde{C}_{\varepsilon_2}$ can change with τ_p and mass loading. Therefore, the model coefficient may change under experimental conditions and can be examined using our data. In pre-unladen turbulence, the model coefficient has the following relation (Bernard and Wallace 2002):

$$C_{\varepsilon_2} = G_0 - S_0 R_{T_0}^{1/2} \tag{5-54}$$

where G_0, S_0, and R_{T0} are defined as (Bernard and Wallace 2002)

$$G_0 = \frac{7\overline{u^2}}{15} \frac{\overline{(\partial^2 u/\partial x^2)^2}}{\overline{(\partial u/\partial x)^2}^2} \tag{5-55}$$

$$S_0 = -\frac{7}{3\sqrt{15}} \frac{\overline{(\partial u/\partial x)^3}}{\overline{(\partial u/\partial x)^2}^{3/2}} \tag{5-56}$$

$$R_{T_0} = \frac{k^2}{\nu_f \varepsilon} \tag{5-57}$$

In the case of particle-laden turbulence, these parameters ($\tilde{G}$, $\tilde{S}$, and $\tilde{R}_T$) are calculated in the same way as in the above equation but by using the modulated physical quantities. We inferred the change in the model coefficient by comparing the parameters in the pre-unladen and particle-laden states.

Fig. 5-14 shows $\tilde{G}$, $\tilde{S}$, and $\tilde{R}_T$ normalized by their corresponding parameters in the pre-unladen state. In the case of $\tilde{G}$, the value was higher than that of G_0 when particles were added. However, $\tilde{S}$ and $\tilde{R}_T$ decreased significantly with an increase in the mass loading. Because these three parameters are all positive real numbers, it can be inferred from Eq. (5-54) that $\tilde{C}_{\varepsilon_2}$ is greater than C_{ε_2}. It should be noted that Eq. (5-55) includes the square of the 2nd derivative of velocity. Thus, when calculating this term using vector fields obtained from PIV, a large random error may be introduced. Therefore, in this study, we focused on estimating qualitative changes in the model coefficient rather than calculating the exact $\tilde{C}_{\varepsilon_2}$. To obtain guidelines for accurate estimation of $\tilde{C}_{\varepsilon_2}$, further research should be conducted using simulations performed under various conditions. In this study, we used the rough linear approximation of $\tilde{C}_{\varepsilon_2} = C\overline{\tilde{\Phi}} + C_{\varepsilon_2}$. Lee and Hwang (2022) also employed this approximation by referring to the study of Squires and Eaton (1994), and used the constant $C = 3$.

Next, the coefficient d in Eq. (5-53) was determined. Vreman (2016) demonstrated how the dissipation rate changes according to the distance from the particle surface using PR-DNS. Although the study used fixed particles, the flow type and Re_p were similar to those in our experiment. It was shown that the dissipation rate at a point approximately $1.5r_p$ away from the particle surface was reduced by approximately 1/10 when compared with that at the surface ($r = r_p$). Therefore, $d \approx 4.5$ can be obtained by exponentially fitting the data between r_p and $1.5r_p$. Although this approach can be considered somewhat rudimentary, it should be noted that previous studies have neglected most of these effects, and this is the first

study to include all of them in a model. To obtain a more accurate coefficient d, further investigation needs to be conducted in the future, as in the case of $\tilde{C}_{\varepsilon_2}$.

The model performance can be assessed using the coefficients obtained above. Results calculated using Eqs. (5-45) and (5-46), as proposed by Lee and Hwang (2022), are shown in Fig. 5-15 (a). The black and red lines correspond to Eqs. (5-45) and (5-46), respectively. Different line types represent particle mass loading cases. The point where these two lines intersect represents the model prediction, and is denoted by a square symbol. It can be seen that the simplified dissipation rate transport equation Eq. (5-46) agrees with the experimental data fairly well, but the simplified TKE transport equation Eq. (5-45) causes the slight difference. To compare Eq. (5-45) with the improved TKE transport equation Eq. (5-53), they are shown together in Fig. 5-15 (b). In the case of Eq. (5-45), TKE and dissipation rate have a linear relationship, whereas it has a curved form in the case of Eq. (5-53). By comparing the experimental results, it can be seen that Eq. (5-53) fits the data points slightly better. Although Eq. (5-53) contains some rudimentary approximations and roughly estimated coefficients, it shows promise in analyzing the experimental results. It would be interesting to see how an improved dissipation rate equation would intersect the lines of Eq. (5-53). The robustness of the model can be improved in the future by conducting further experiments and simulations for various cases.

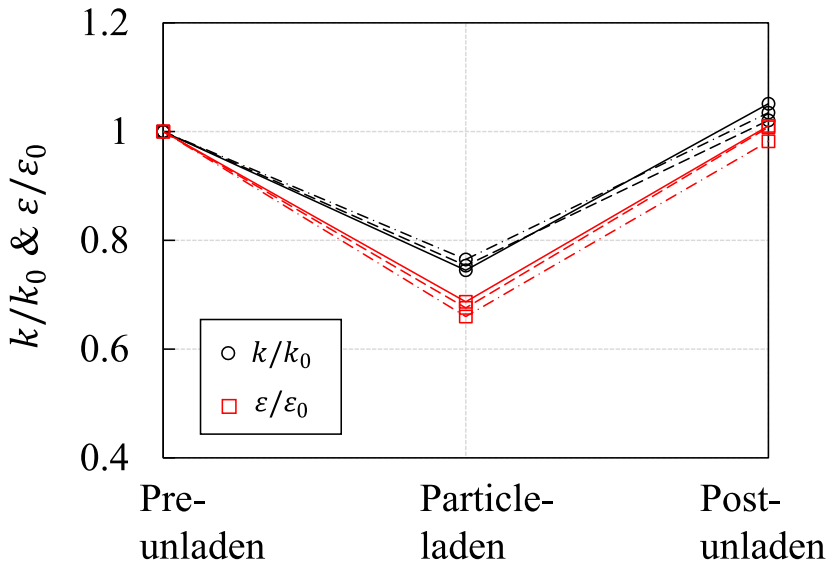

Fig. 5-1 Changes in TKE and dissipation rate for pre-unladen, laden ($\bar{\tilde{\Phi}} = 0.17$), and post-unladen states of turbulence.

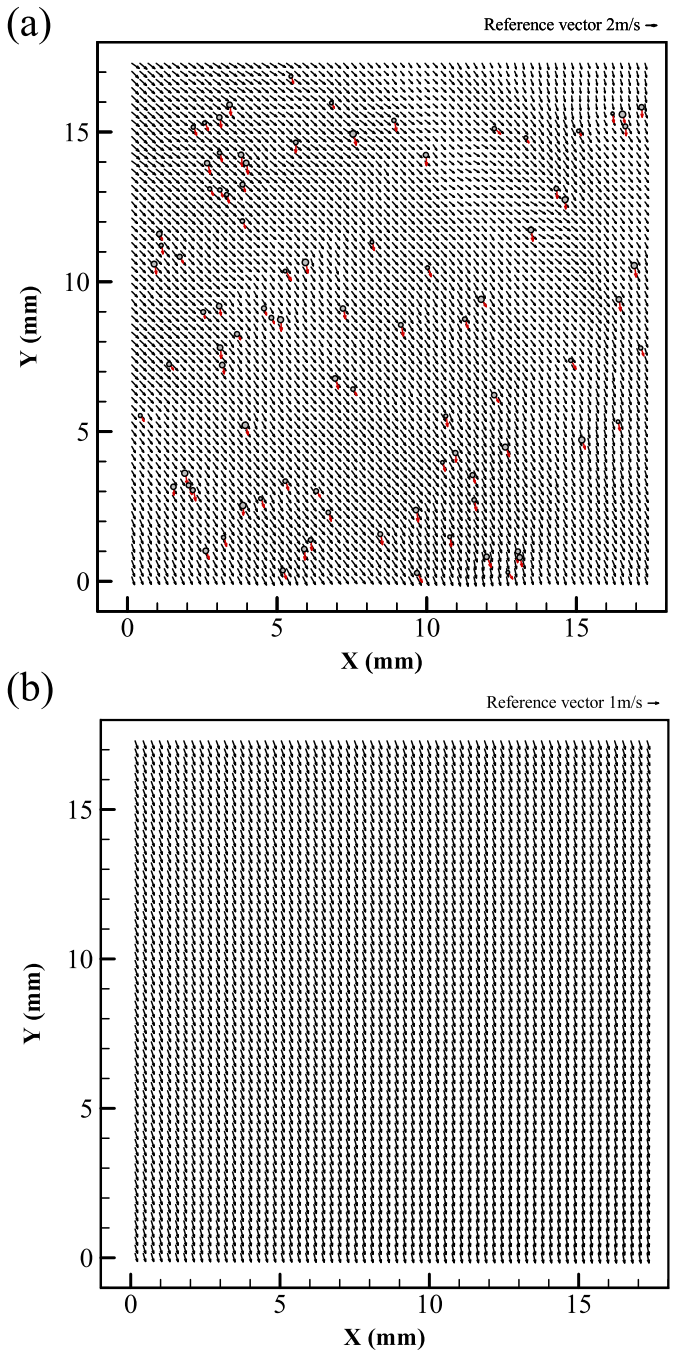

Fig. 5-2 (a) Instantaneous and (b) mean velocity field of particle-laden turbulence for the highest mass loading case ($\overline{\widetilde{\Phi}} = 0.69$).

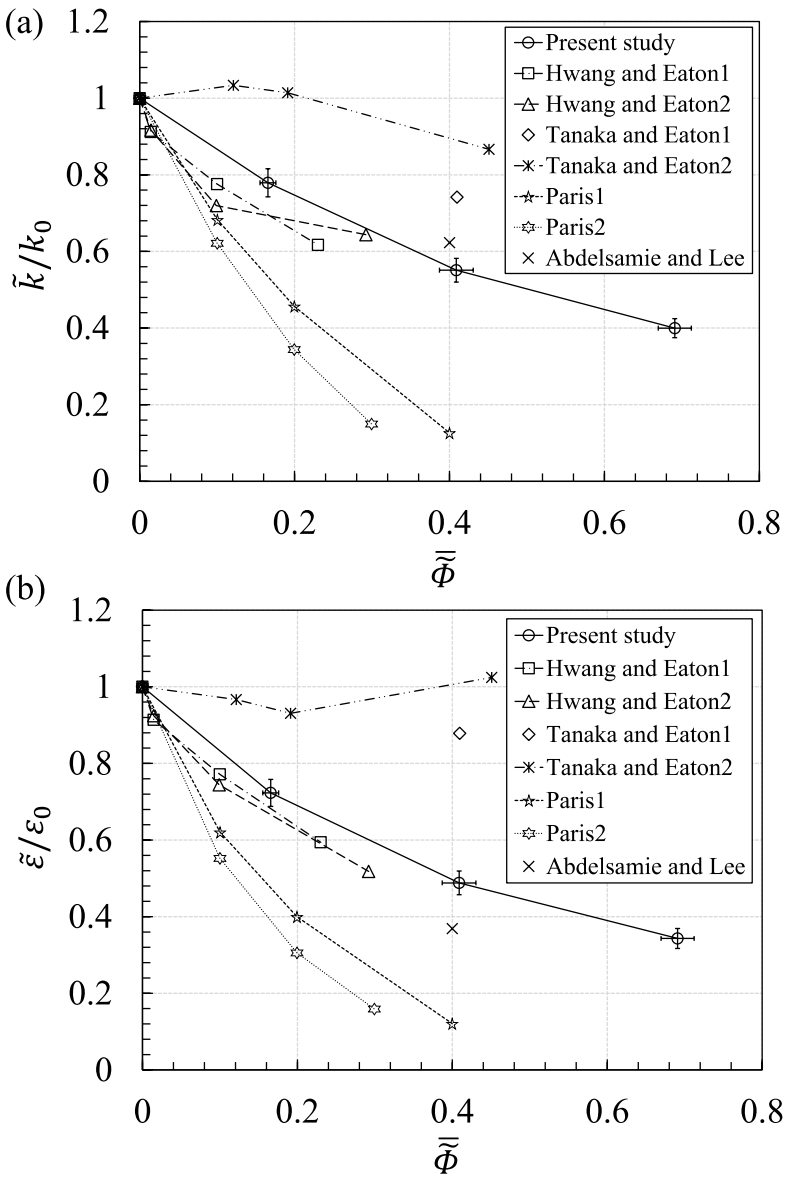

Fig. 5-3 Changes in (a) TKE and (b) dissipation rate according to particle mass loading.

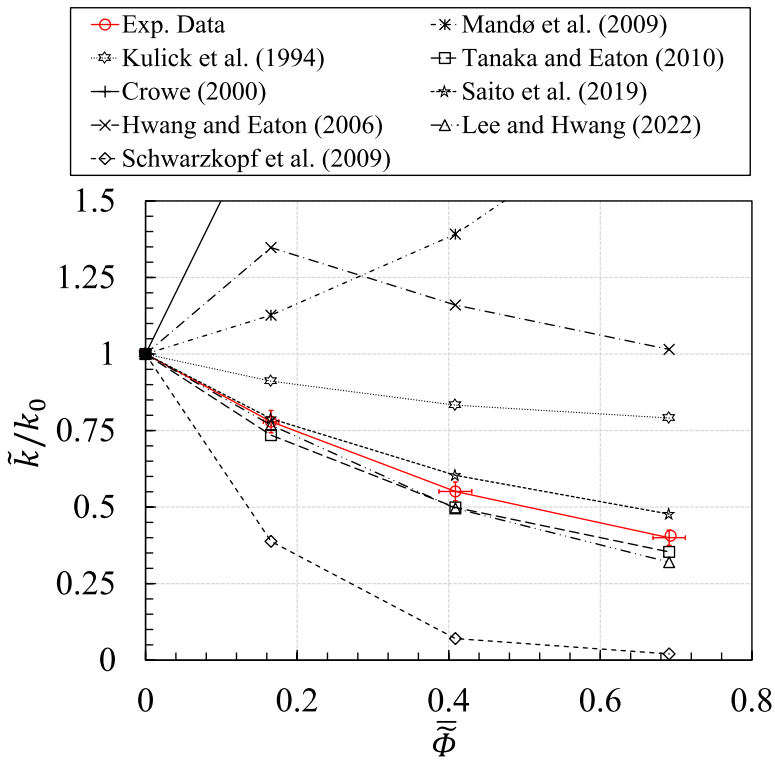

Fig. 5-4 Comparison of modulated TKE calculated using various theoretical models and our experimental dissipation rate data.

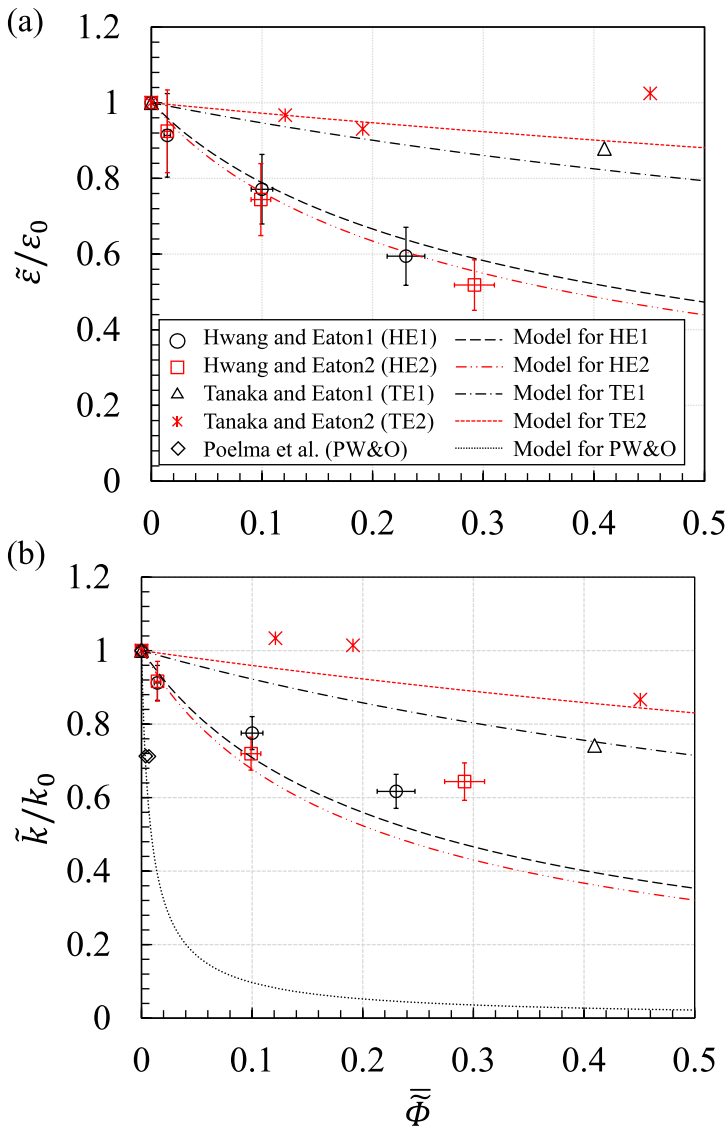

Fig. 5-5 Changes in (a) dissipation rate and (b) TKE according to particle mass loading in particle-laden isotropic turbulence. Symbols are data from previous studies, and lines are results predicted by Eqs. (5-31) and (5-32).

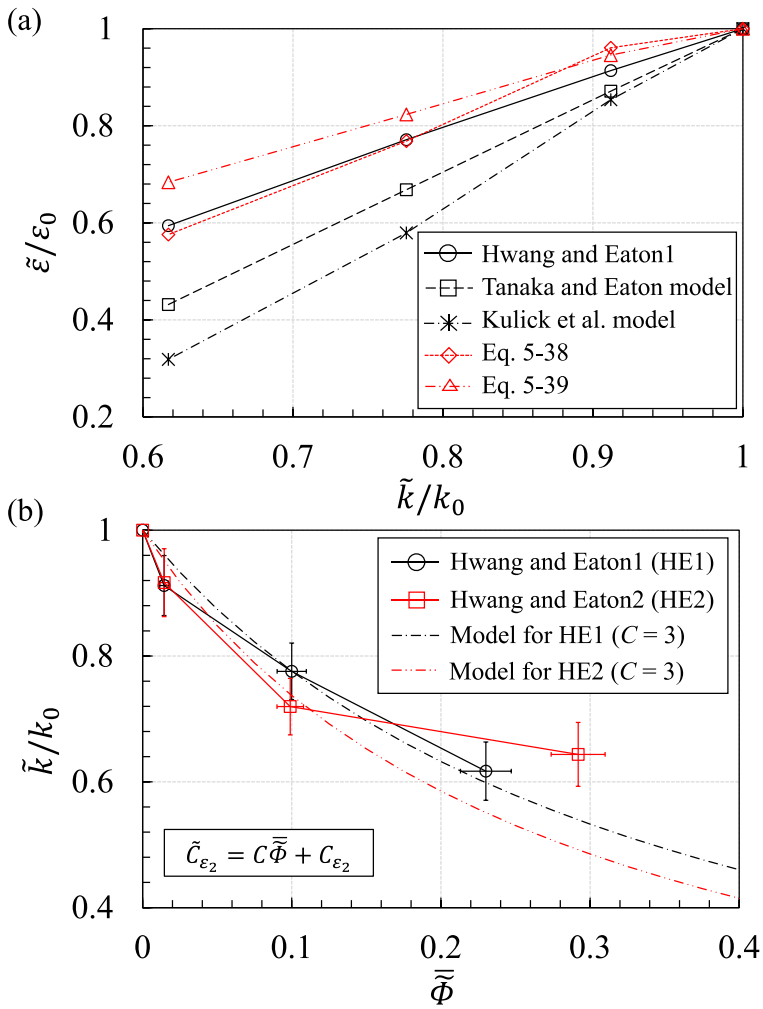

Fig. 5-6 (a) Modulated TKE and dissipation rate obtained from previous experimental data (Hwang and Eaton 2006), previous models (Kulick et al. 1994; Tanaka and Eaton 2010), and Eqs. (5-38) - (5-39). (b) Change of prediction using modified model coefficient (C = 3).

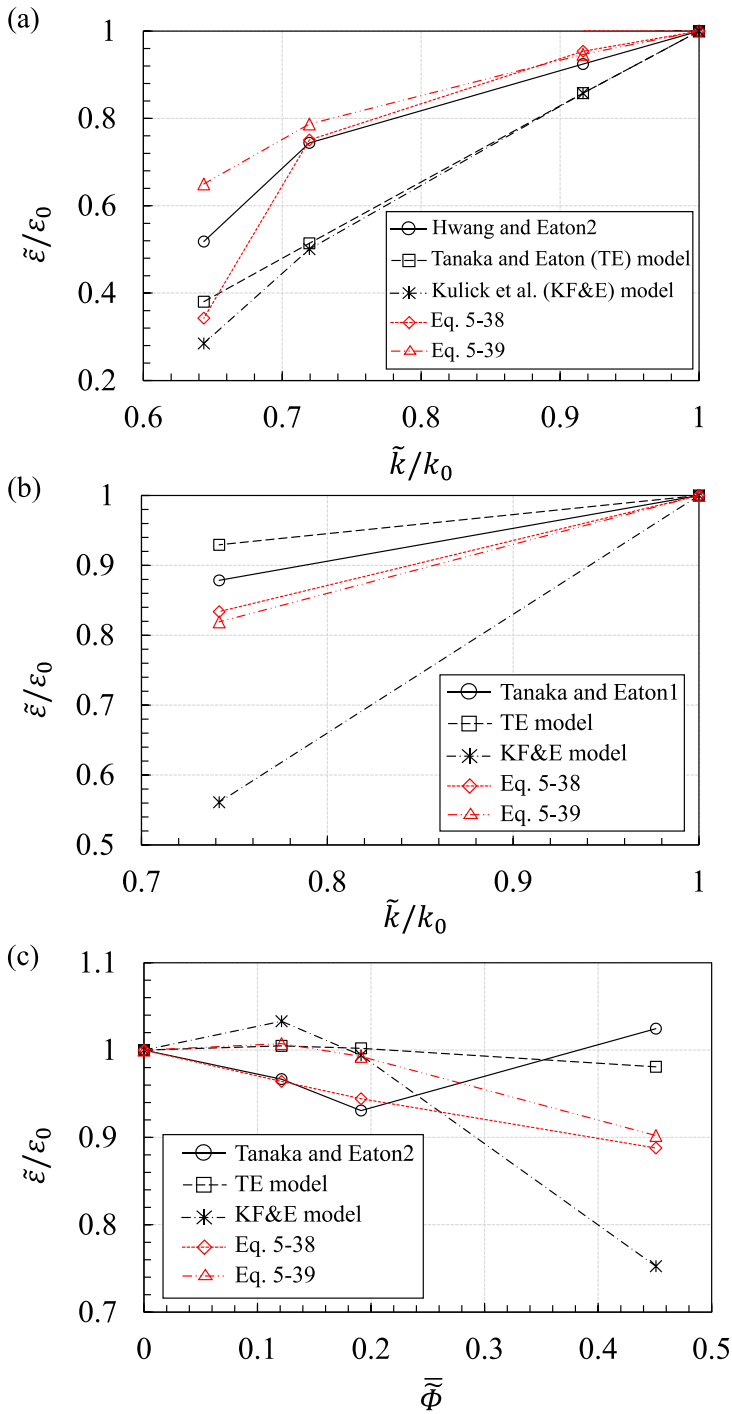

Fig. 5-7 Modulated TKE and dissipation rate obtained from previous experimental data, previous model, and Eqs. (5-38) - (5-39). Experimental data obtained from (a) HE2, (b) TE1, and (c) TE2.

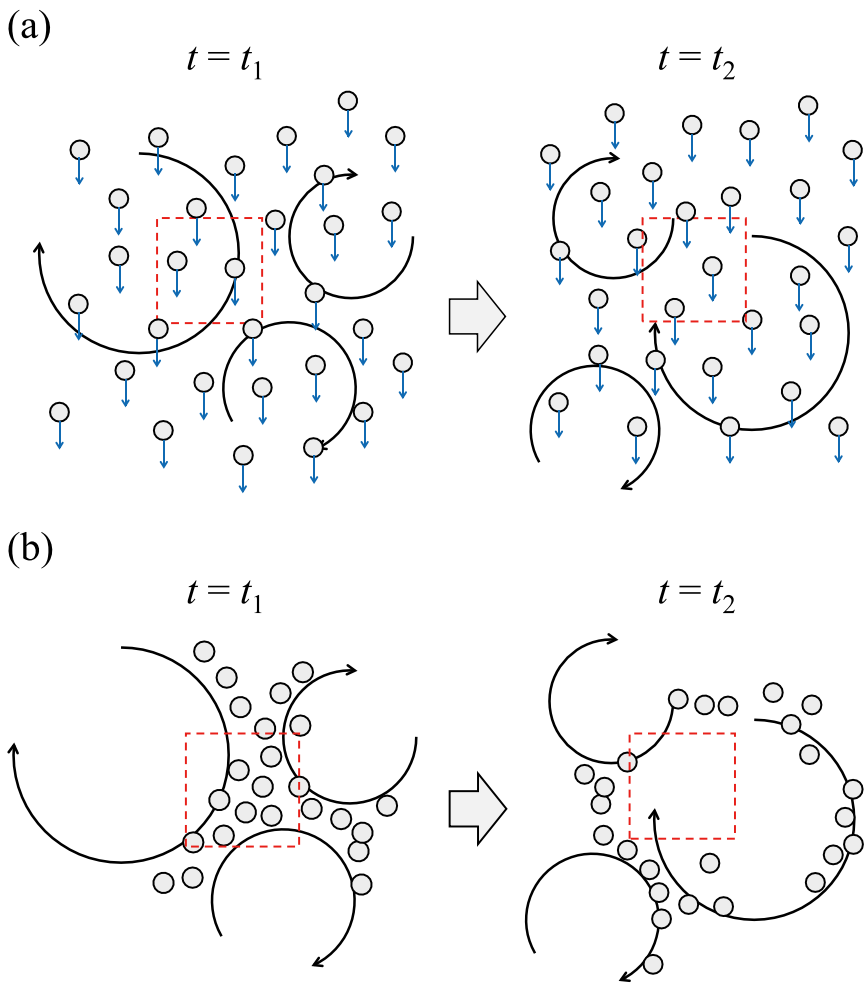

Fig. 5-8 Schematic of the distribution of particles in a turbulent flow (a) for heavy and high Stokes number particles (b) for low Stokes number particles.

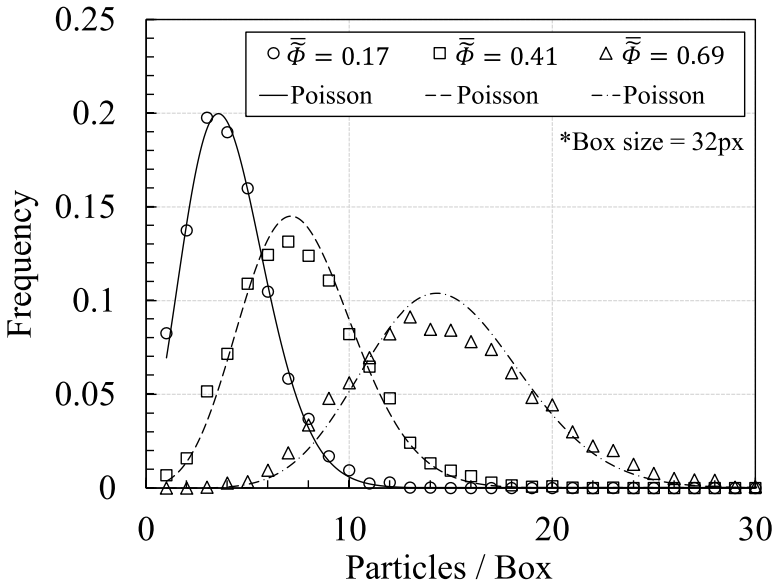

Fig. 5-9 Distribution of number of particles in each box.

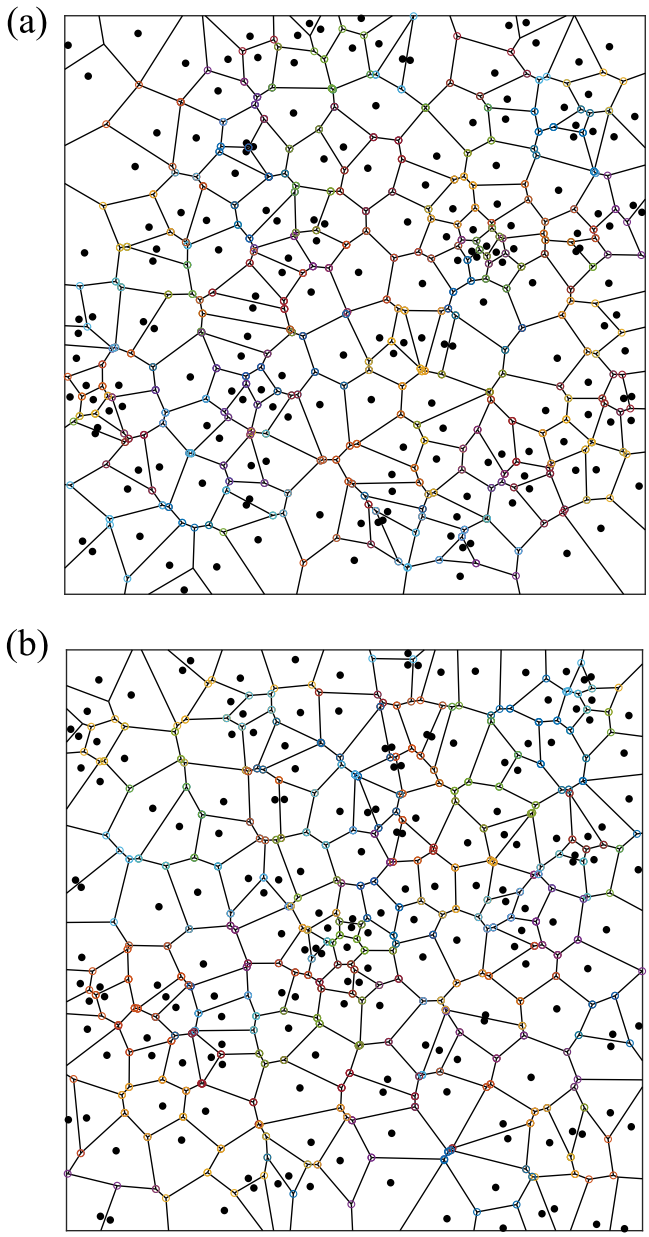

Fig. 5-10 Voronoi diagrams applied to (a) the highest mass loading ($\bar{\bar{\tilde{\Phi}}} = 0.69$) case and (b) synthetic data assuming random Poisson process.

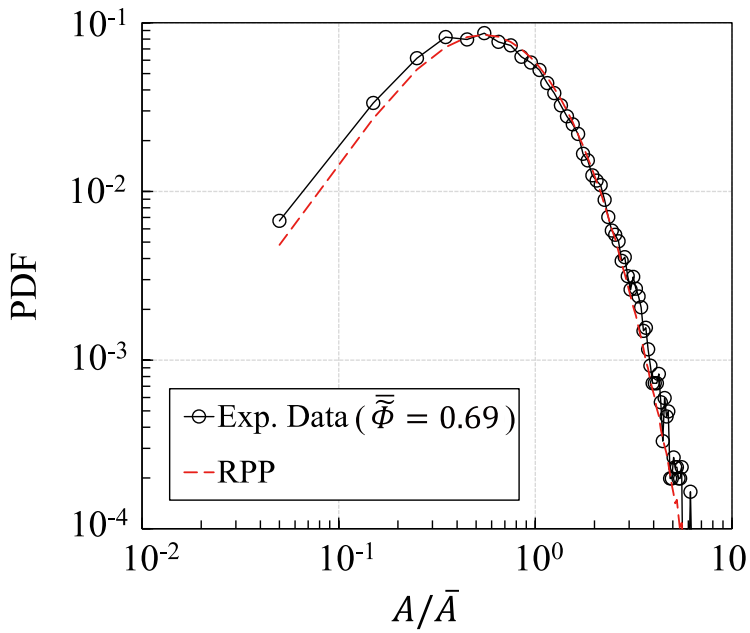

Fig. 5-11 PDF of Voronoi cell area

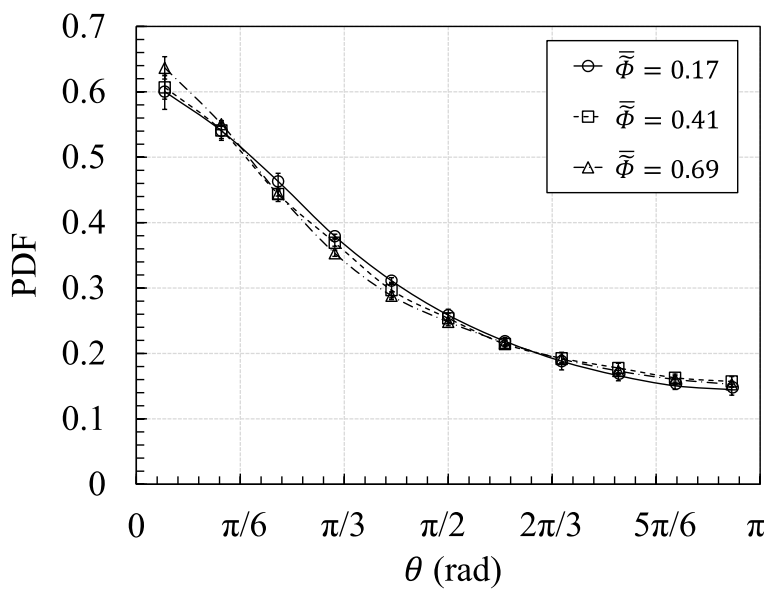

Fig. 5-12 PDF of the angle between the fluid and particle fluctuation velocity.

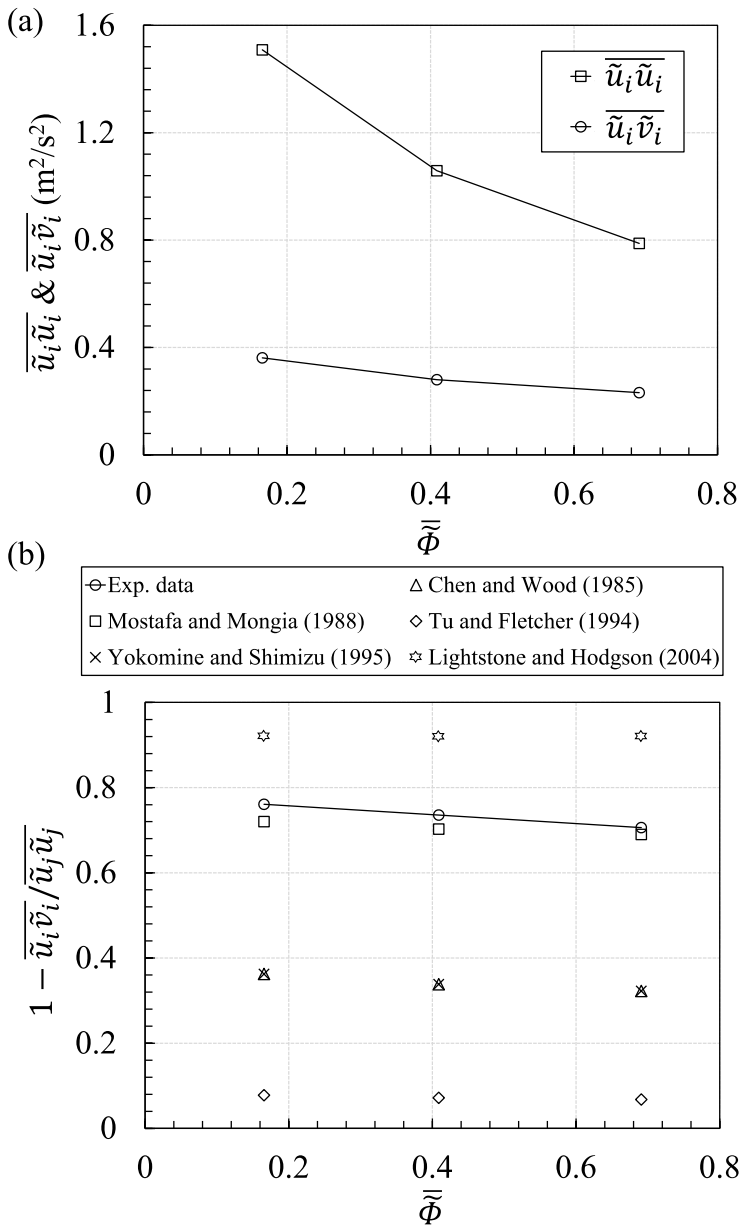

Fig. 5-13 (a) Fluid–fluid and fluid–particle correlation terms with mass loading. (b) Ratio between these correlation terms obtained from our experiments and previous models.

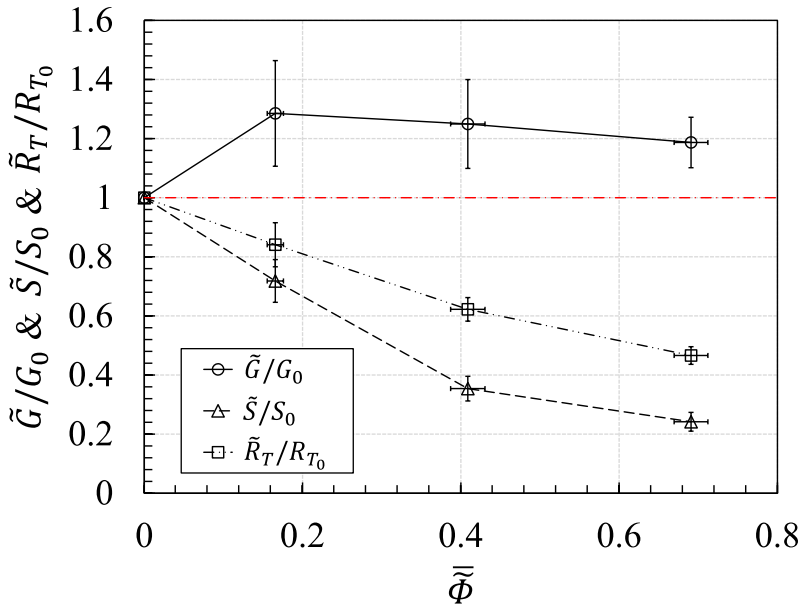

Fig. 5-14 Changes in normalized parameters according to mass loading.

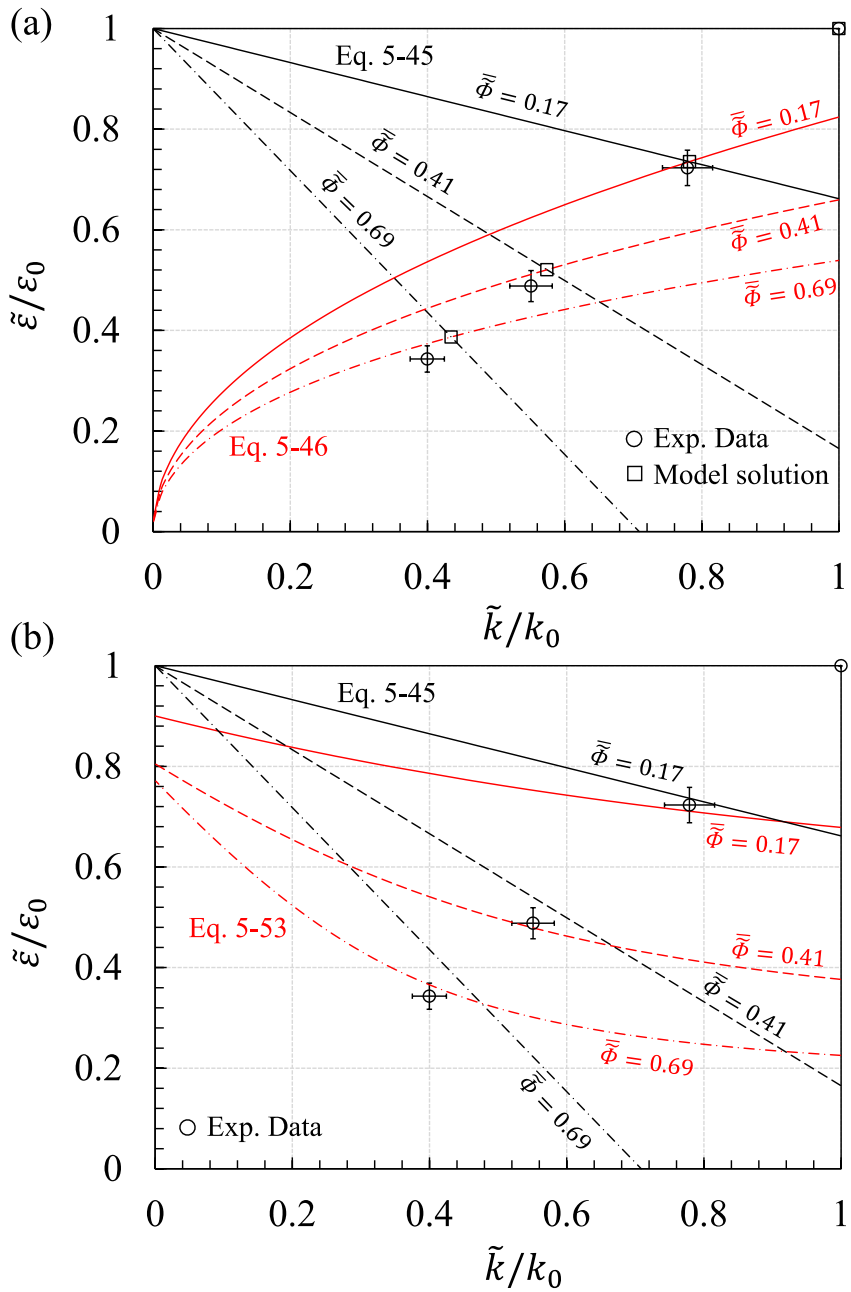

Fig. 5-15 (a) Comparison of experimental data and model predictions, (b) comparison of TKE transport Eqs. (5-45) and (5-53).

Table 5-1 Experimental conditions of previous studies for particle-laden isotropic turbulence.

Ref.	Hwang and Eaton (2006)		Tanaka and Eaton (2010)		Poelma et al. (2007)
Case	HE1	HE2	TE1	TE2	PW&O
Flow	Stationary turbulence		Stationary turbulence		Decaying turbulence
Fluid	Air		Air		Water
Particle	Glass		Glass		Ceramic
$\bar{\bar{\Phi}}_{\max}$	0.23	0.29	0.45	0.41	0.0067
$\mathcal{C}_{\max}$ ($\times 10^{-3}$)	0.11	0.14	0.22	0.20	1.76
ρ_p/ρ_f	2083		2083		3.8
d_p (μm)	165		250	500	280
d_p/η_0	0.97	0.87	2.3	4.5	1.0
k_0 (m^2/s^2)	0.7	0.55	1.46		11.4×10^{-5}
ε_0 (m^2/s^3)	4.07	2.73	28.2		22.3×10^{-5}

Table 5-2 Parameters for particle-laden turbulence.

Study	Case	Flow	τ_p/τ_{k0} (St_k)	d_p/η_0	ρ_p/ρ_f	Re_p
Present study	-	HIT (exp.)	90	1.19	2080	12.0
Hwang and Eaton (2006)	H&E1	HIT (exp.)	59	0.96	2080	7
	H&E2		48	0.87	2080	7
Tanaka and Eaton (2010)	T&E1	HIT (exp.)	274	2.3	2080	33
	T&E2		550	4.5	2080	134
Paris (2001)	P1	Channel (exp.)	47	0.41	7310	8
	P2		49	0.88	2080	18.8
Abdelsamie and Lee (2012)	A&L	HIT (simulation)	5	0.33	800	-

Table 5-3 Models describing the relationship between modulated TKE and dissipation rate.

Previous study	Applied flow type	Model equation
Kulick et al. (1994)	Channel flow	$\left(\tilde{k}/k_0\right)^3 - (\tilde{\varepsilon}/\varepsilon_0)^2 - 2\bar{\bar{\Phi}}\tilde{k}\tilde{\varepsilon}/\left(\tau_p\varepsilon_0^2\right) = 0$
Crowe (2000)	Centerline of pipe flow	$\tilde{k} = \left(k_0^{3/2} l_h/\eta_0 + \alpha_p\rho_p g^2\tau_p/\left(\alpha_f\rho_f\right)\right)^{2/3}$
Hwang and Eaton (2006)	HIT	$\tilde{k} = \tau_p\left(\varepsilon_0 - \tilde{\varepsilon} + \bar{\bar{\Phi}} g V_t\right)/\left(2\bar{\bar{\Phi}}\right)$
Schwarzkopf et al. (2009)	Homogeneous turbulence	$\tilde{k} = \tilde{\varepsilon}^2/\left(0.0587\left(Re_p\right)^{1.4161}\dfrac{\bar{\bar{\Phi}}\mu_f^2\tau_p^2 g^2}{\rho_p\rho_f\pi d_p^4/6}\right)$
Mandø et al. (2009)	Centerline of pipe flow	$\tilde{k}^{3/2} - l_e\bar{\bar{\Phi}}\left(g^2\tau_p^2 - 2\tilde{k}\right)/\tau_p - k_0^{3/2} = 0$
Tanaka and Eaton (2010)	HIT	$\tilde{k} = k_0 + \tau_p(\tilde{\varepsilon} - \varepsilon_0)$
Saito et al. (2019)	HIT	$\tilde{k} = k_0\left(1 + 3.61\tilde{T}/t_f\right)^{-2/3}$
Lee and Hwang (2022)	HIT	$\tilde{k} = \tilde{C}_{\varepsilon_2}\tilde{\varepsilon}^2/\left(C_{\varepsilon_2}\varepsilon_0^2/k_0 - 2\bar{\bar{\Phi}}\tilde{\varepsilon}/\tau_p\right)$, where $\tilde{C}_{\varepsilon_2} = C\bar{\bar{\Phi}} + C_{\varepsilon_2}$, $C = 3$, and $C_{\varepsilon_2} = 1.92$

Table 5-4 Modeling of correlation terms.

Study	$\mathbf{1-\overline{\tilde{u}_i\tilde{v}_i}/\overline{\tilde{u}_i\tilde{u}_i}}$	$\mathbf{1-\overline{\frac{\partial\tilde{u}_i}{\partial x_j}\frac{\partial\tilde{v}_i}{\partial x_j}}/\overline{\frac{\partial\tilde{u}_i}{\partial x_j}\frac{\partial\tilde{u}_i}{\partial x_j}}}$
Danon et al. (1977)	$1-\exp\left(-B\frac{\tau_p}{\tau_k}\right)$	1
	with $\tau_k=\left(\nu_f/\tilde{\varepsilon}\right)^{1/2}$, B is empirical constant	
Chen and Wood (1985)	$1-\exp\left(-B_k\frac{\tau_p}{\tau_e}\right)$	1
	with $B_k=0.0825,\ \tau_e=0.165\tilde{k}/\tilde{\varepsilon}$	
Mostafa and Mongia (1988)	$1-\left(\frac{\tau_{LI}}{\tau_{LI}+\tau_p}\right)$	$1-\left(\frac{\tau_{LI}}{\tau_{LI}+\tau_p}\right)$
	with $\tau_{LI}=0.35\tilde{k}/\tilde{\varepsilon}$	
Tu and Fletcher (1994)	$1-\exp\left(-\frac{B_k\tau_p}{\left(\bar{\tilde{\Phi}}^n\tilde{k}/\tilde{\varepsilon}\right)}\right)$	$1-\exp\left(-\frac{B_\varepsilon\tau_p}{\left(\bar{\tilde{\Phi}}^n\tilde{k}/\tilde{\varepsilon}\right)}\right)$
	with $\begin{cases} n=0\ (\bar{\tilde{\Phi}}\le 1) \\ n=1\ (\bar{\tilde{\Phi}}>1)\end{cases}$, $B_k=0.09,\ B_\varepsilon=0.4$	
Yokomine and Shimizu (1995)	$\left[1-\exp\left(-\frac{\tilde{\varepsilon}}{2\tilde{k}}\tau_p\right)\right]\exp\left(-B_Y\frac{d_p}{l_e}\right)$	1
	with $B_Y=0.1,\ l_e$ is length scale of the eddy	
Lightstone and Hodgson (2004)	$1-\left(\frac{\tau^*}{\tau^*+\tau_p}\right)$	$1-\left(\frac{\tau^*}{\tau^*+\tau_p}\right)$
	with $1/\tau^*=1/\left(0.135\tilde{k}/\tilde{\varepsilon}\right)+\left\lvert\tilde{U}_i-\tilde{V}_i\right\rvert/\left(0.22\tilde{k}^{3/2}/\tilde{\varepsilon}\right)$	

6. Conclusion and Future work

In this study, modulation of homogeneous isotropic turbulence (HIT) due to small and heavy particles was experimentally investigated. HIT was created in a truncated chamber via synthetic jet actuators utilizing woofer speakers, and the flow was measured using a 2D particle image velocimetry (PIV) system. To accurately measure fully 3D HIT with 2D PIV, analysis of uncertainty and error was preceded.

First, the effect of out-of-plane motion on turbulence statistics measured by 2D planar PIV was investigated. Turbulence statistics respond more sensitively to out-of-plane motion than velocity because they contain fluctuating and derivative terms. The specific flow that was considered was 3D isotropic turbulence generated by DNS, from the Johns Hopkins turbulence database. Statistics such as turbulence kinetic energy (TKE), viscous dissipation rate, Taylor and Kolmogorov length scales, and velocity correlations were calculated. Synthetic tracer particle images were utilized, to accurately control various PIV parameters and quantify the error compared to DNS. Camera interframe time, laser sheet thickness, and interrogation window size (W_s) were the three main PIV factors that were examined which influence turbulence statistics when significant out-of-plane motion is present. The following results can be utilized to optimize experimental parameters when examining 3D turbulence via 2D PIV. They can also be used to assess the error level of turbulence statistics from previous HIT studies.

The instantaneous velocity depends on out-of-plane motion value F_o and W_s. The smaller the W_s is, the more sensitive the velocity is to out-of-plane motion. In the case of the smallest normalized W_s of 18.58, the velocity error increased sharply when the F_o value fell below about 0.6.

The TKE and viscous dissipation rate were generally both slightly underestimated compared to DNS for relatively small out-of-plane motion areas, due to the spatial filtering effect of the PIV interrogation windows. However, since these values are both very sensitive to out-of-plane motion, the spatially averaged values reached up to 7 times and 62 times the true value, respectively, for the minimum interrogation window corresponding to 16 x 16 pixels. We also estimated error as a function of F_o, and found that the dissipation rate is significantly more sensitive to out-of-plane motion than TKE.

For the Taylor and Kolmogorov length scales, the error distribution was small compared to the TKE and dissipation rate. As the interframe time was increased, the

distribution shifted, and the length scales became underestimated compared to DNS.

The two-point velocity correlation matched the DNS data very well for small W_s^* = 18.58 and Δt^* = 0.043. As the interframe time was increased for this W_s^*, the correlation decreased quite a bit because of out-of-plane data dropout. As a result, the integral length scale also became underestimated.

Second, we estimated the perspective error in homogeneous isotropic turbulence (HIT) and proposed a method for correcting it. The theoretically derived equation shows that the effect of this error on the velocity is inversely proportional to the distance from the lens to the camera sensor and proportional to the displacement in the out-of-plane direction and the relative position from the sensor center. The error in the velocity propagates when calculating turbulence statistics such as TKE, dissipation rate, and two-point statistics. Because the perspective error is a type of systematic (i.e. bias) error, the true value can be obtained by correction. Correction equations for these statistics were presented under the assumption of isotropy.

Synthetic turbulence was used to verify the equations. Perspective error was added to the synthetic velocity field, and the turbulence statistics were calculated. The error in the TKE and dissipation rate increased toward the edge of the field, as expected. For spatially averaged TKE, the error reached approximately 16%, and the dissipation rate was found to be approximately twice as sensitive to the perspective error compared to TKE. However, using the correction equations, the errors were reduced significantly.

In the case of the velocity correlation coefficient, the perspective error was canceled out or reduced to a small value during the normalization process. However, when the integral length scale was calculated, the error accumulated during the integration process and caused a difference of approximately 8% from the true value. This value was considerably large compared with the 1% error which was obtained after applying the correction. A larger error than that of the velocity correlation was observed for the structure function, which is often used to indirectly calculate the dissipation rate or to confirm isotropy. Misinterpretation regarding isotropy can be avoided using the proposed corrections.

One of the correction equations was examined in an actual experiment, to demonstrate the validity of the technique. TKE was obtained using grid turbulence in a wind tunnel. Using a 2D PIV system with a wide-angle lens, the TKE was overestimated by up to 20 times at the edge of the image. However, when the correction was applied, the results were similar to those obtained when using a lens

with a long focal length (which has small perspective error). Therefore, we believe that the equations presented in this study can be useful for actual experiments to correct for perspective error.

Based on these analyses, experimental parameters were set to make the effect of loss of pair and perspective error appear negligible. We first examined HIT without particles. In the case of pre-unladen turbulence, the mean velocity was small, whereas a turbulent flow structure with various eddies could be clearly observed in the instantaneous velocity field. The TKE was relatively uniform within the region of interest, and the ratio of the RMS velocities in the x and y direction was calculated to be close to unity. This implies that the turbulence was homogeneous and isotropic. The Taylor microscale Reynolds number Re_λ reached 271 at the highest speaker level. The flow followed isotropic turbulence theory as suggested in previous studies. It satisfied the Kolmogorov 4/5 law, which can be obtained from the 3rd-order structure function, and the model energy spectrum collapsed well. These results further demonstrated that the flow generated in the chamber was HIT.

The effect of the particles on the turbulence was examined by comparing the turbulence kinetic energy (TKE) and dissipation rate in pre-unladen and particle-laden turbulence. Particles were injected into the HIT at $Re_\lambda = 237$. Spherical glass particles 164 μm in size were used, which is comparable to the Kolmogorov length scale of the flow. Owing to the high particle density, the Stokes number was approximately 90, and thus the particles settled quickly. The mean flow, which was almost zero before the particles were added, flowed in the downward direction due to viscous drag of the particles. The particles affected not only the mean flow but also the turbulence, due to two-way coupling. In particle-laden turbulence, both the TKE and dissipation rate were attenuated with increasing particle mass loading up to 0.69.

The experimental results were compared with theoretical models proposed in previous studies. Although some models predicted the modulated TKE fairly well, we used the particle-laden transport equations to further improve the physical model for TKE and dissipation rate. The Stokes number in this study was large, but the correlation between the particle and fluid fluctuation velocity had a non-negligible effect, and was thus kept in the model. To overcome the limitations of the point-particle approach, additional dissipation occurring at the particle surface and energy transferred from the mean kinetic energy by the particle wakes were included. These effects made the relationship between the modulated TKE and dissipation rate nonlinear, but allowed better performance in matching our experimental results. The

newly proposed model included some rough approximations and estimation of coefficients. Nevertheless, we believe that this study contributes significantly toward improving our understanding of the two-way coupling phenomenon by providing a more comprehensive physical model of the complex particle-turbulence interaction in a relatively simple form.

In future works, studies on poly-disperse particles can be conducted. In this study, a mono-dispersed particle system has been assumed for simplicity and computational convenience. However, most of the turbulence encountered in nature or engineering includes particles of various sizes. Therefore, it is necessary to proceed with simulations and experiments on changes in turbulence containing particles with various sizes. Based on these data, the theoretical model presented in this study can be extended to be applicable to the poly-disperse particle system.

References

Abdelsamie AH, Lee C (2012) Decaying versus stationary turbulence in particle-laden isotropic turbulence: Turbulence modulation mechanism. Phys Fluids 24:015106

Antonia R, Tang S, Djenidi L, Zhou Y (2019) Finite Reynolds number effect and the 4/5 law. Phys Rev Fluids 4:084602

Armenio V, Fiorotto V (2001) The importance of the forces acting on particles in turbulent flows. Phys Fluids 13:2437-2440

Bagchi P, Balachandar S (2004) Response of the wake of an isolated particle to an isotropic turbulent flow. J Fluid Mech 518:95-123

Balachandar S, Eaton JK (2010) Turbulent dispersed multiphase flow. Annu Rev Fluid Mech 42:111-133

Batchelor GK, Townsend A (1947) Decay of vorticity in isotropic turbulence. Proc R Soc London, Ser A 190:534-550

Bellani G, Variano EA (2014) Homogeneity and isotropy in a laboratory turbulent flow. Exp Fluids 55:1-12

Benedict LH, Gould RD (1996) Towards better uncertainty estimates for turbulence statistics. Exp Fluids 22:129-136

Bernard PS, Wallace JM (2002) Turbulent flow: analysis, measurement, and prediction. John Wiley & Sons,

Birouk M, Chauveau C, Sarh B, Quilgars A, Gökalp I (1996) Turbulence effects on the vaporization of monocomponent single droplets. Combust Sci Technol 113:413-428

Boivin M, Simonin O, Squires KD (1998) Direct numerical simulation of turbulence modulation by particles in isotropic turbulence. J Fluid Mech 375:235-263

Brandt L, Coletti F (2022) Particle-laden turbulence: progress and perspectives. Annu Rev Fluid Mech 54:159-189

Burton TM, Eaton JK (2005) Fully resolved simulations of particle-turbulence interaction. J Fluid Mech 545:67-111

Canuto V, Cheng Y (1997) Determination of the Smagorinsky–Lilly constant CS. Phys Fluids 9:1368-1378

Carter D, Coletti F (2018) Small-scale structure and energy transfer in homogeneous turbulence. J Fluid Mech 854:505-543

Carter D, Petersen A, Amili O, Coletti F (2016) Generating and controlling homogeneous air turbulence using random jet arrays. Exp Fluids 57:1-15

Carter DW, Coletti F (2017) Scale-to-scale anisotropy in homogeneous

turbulence. J Fluid Mech 827:250-284

Chang K, Bewley GP, Bodenschatz E (2012) Experimental study of the influence of anisotropy on the inertial scales of turbulence. J Fluid Mech 692:464-481

Charonko JJ, Vlachos PP (2013) Estimation of uncertainty bounds for individual particle image velocimetry measurements from cross-correlation peak ratio. Meas Sci Technol 24:065301

Chen C, Wood P (1984) Turbulence closure modeling of two-phase flows. Chem Eng Commun 29:291-310

Chen C, Wood P (1985) A turbulence closure model for dilute gas-particle flows. Can J Chem Eng 63:349-360

Christensen K (2004) The influence of peak-locking errors on turbulence statistics computed from PIV ensembles. Exp Fluids 36:484-497

Coleman HW, Steele WG (2018) Experimentation, validation, and uncertainty analysis for engineers. John Wiley & Sons, New Jersey

Comte-Bellot G, Corrsin S (1966) The use of a contraction to improve the isotropy of grid-generated turbulence. J Fluid Mech 25:657-682

Crowe CT (2000) On models for turbulence modulation in fluid–particle flows. Int J Multiphase Flow 26:719-727

Danon H, Wolfshtein M, Hetsroni G (1977) Numerical calculations of two-phase turbulent round jet. Int J Multiphase Flow 3:223-234

De Jong J, Cao L, Woodward S, Salazar J, Collins L, Meng H (2009) Dissipation rate estimation from PIV in zero-mean isotropic turbulence. Exp Fluids 46:499-515

De Kat R, Van Oudheusden B (2012) Instantaneous planar pressure determination from PIV in turbulent flow. Exp Fluids 52:1089-1106

De Silva I, Fernando H (1994) Oscillating grids as a source of nearly isotropic turbulence. Phys Fluids 6:2455-2464

Dou Z, Pecenak ZK, Cao L, Woodward SH, Liang Z, Meng H (2016) PIV measurement of high-Reynolds-number homogeneous and isotropic turbulence in an enclosed flow apparatus with fan agitation. Meas Sci Technol 27:035305

Elghobashi S (1994) On predicting particle-laden turbulent flows. Appl Sci Res 52:309-329

Elghobashi S, Abou-Arab T (1983) A two-equation turbulence model for two-phase flows. The Physics of Fluids 26:931-938

Elghobashi S, Truesdell G (1992) Direct simulation of particle dispersion in a decaying isotropic turbulence. J Fluid Mech 242:655-700

Elghobashi S, Truesdell G (1993) On the two-way interaction between

homogeneous turbulence and dispersed solid particles. I: Turbulence modification. Phys Fluids A 5:1790-1801

Elgobashi S (2006) An updated classification map of particle-laden turbulent flows IUTAM Symposium on Computational Approaches to Multiphase Flow. Springer, pp. 3-10

Fallon T, Rogers C (2002) Turbulence-induced preferential concentration of solid particles in microgravity conditions. Exp Fluids 33:233-241

Ferrante A, Elghobashi S (2003) On the physical mechanisms of two-way coupling in particle-laden isotropic turbulence. Phys Fluids 15:315-329

Goepfert C, Marié J-L, Chareyron D, Lance M (2010) Characterization of a system generating a homogeneous isotropic turbulence field by free synthetic jets. Exp Fluids 48:809-822

Goossens WR (2019) Review of the empirical correlations for the drag coefficient of rigid spheres. Powder Technol 352:350-359

Hain R, Kähler C (2007) Fundamentals of multiframe particle image velocimetry (PIV). Exp Fluids 42:575-587

Han K, Lee H, Hwang W (2020) Pseudo real-time continuous measurements of particle preferential concentration in homogeneous isotropic turbulence. Exp Therm Fluid Sci 112:109968

Hart DP (2000) PIV error correction. Exp Fluids 29:13-22

Hassaini R, Coletti F (2022) Scale-to-scale turbulence modification by small settling particles. J Fluid Mech 949:A30

Hoffman DW, Eaton JK (2021) Isotropic turbulence apparatus with a large vertical extent. Exp Fluids 62:1-11

Hwang W, Eaton JK (2004) Creating homogeneous and isotropic turbulence without a mean flow. Exp Fluids 36:444-454

Hwang W, Eaton JK (2006) Homogeneous and isotropic turbulence modulation by small heavy (St~50) particles. Journal of Fluid Mechanics 564:361-393

Kähler CJ, Astarita T, Vlachos PP, Sakakibara J, Hain R, Discetti S, La Foy R, Cierpka C (2016) Main results of the 4th International PIV Challenge. Exp Fluids 57:1-71

Kähler CJ, Scharnowski S, Cierpka C (2012) On the uncertainty of digital PIV and PTV near walls. Exp Fluids 52:1641-1656

Keane RD, Adrian RJ (1990) Optimization of particle image velocimeters. I. Double pulsed systems. Meas Sci Technol 1:1202

Keane RD, Adrian RJ (1991) Optimization of particle image velocimeters: II. Multiple pulsed systems. Meas Sci Technol 2:963

Keane RD, Adrian RJ (1992) Theory of cross-correlation analysis of PIV

images. Appl Sci Res 49:191-215

Kiger K, Pan C (2000) PIV technique for the simultaneous measurement of dilute two-phase flows. J Fluids Eng 122:811-818

Kim M, Lee H, Hwang W (2021) Experimental study on the flow interaction between two synthetic jets emanating from a dual round orifice. Exp Therm Fluid Sci 126:110400

Kolmogorov AN (1991) Dissipation of energy in the locally isotropic turbulence. Proc R Soc London, Ser A 434:15-17

Kuerten J (2016) Point-Particle DNS and LES of Particle-Laden Turbulent flow-a state-of-the-art review. Flow Turbul Combust 97:689-713

Kulick JD, Fessler JR, Eaton JK (1994) Particle response and turbulence modification in fully developed channel flow. Journal of Fluid Mechanics 277:109-134

Langford JA, Moser RD (1999) Optimal LES formulations for isotropic turbulence. J Fluid Mech 398:321-346

Lecordier B, Westerweel J (2004) The EUROPIV synthetic image generator (SIG) Particle image velocimetry: recent improvements. Springer, pp. 145-161

Lee H, Han K, Park HJ, Jung H, Hwang W (2018) Generation and characterization of homogeneous isotropic turbulence. J Korean Soc Visualization 16:21-29

Lee H, Hwang W (2019) Error quantification of 3D homogeneous and isotropic turbulence measurements using 2D PIV. Int J Heat Fluid Flow 78:108431

Lee H, Hwang W (2022) Prediction of Homogeneous Isotropic Turbulence Modulation by Small and Heavy Particles. Phys Fluids

Lee H, Park HJ, Kim M, Han J, Hwang W (2022) The effect of perspective error on 2D PIV Measurements of homogeneous isotropic turbulence. Exp Fluids 63:122 DOI 10.1007/s00348-022-03483-w

Li Y, Perlman E, Wan M, Yang Y, Meneveau C, Burns R, Chen S, Szalay A, Eyink G (2008) A public turbulence database cluster and applications to study Lagrangian evolution of velocity increments in turbulence. J Turbul 9:N31

Lian H, Charalampous G, Hardalupas Y (2013) Preferential concentration of poly-dispersed droplets in stationary isotropic turbulence. Exp Fluids 54:1-17

Lightstone MF, Hodgson SM (2004) Turbulence Modulation in Gas-Particle Flows: A Comparison of Selected Models. Can J Chem Eng 82:209-219

Lilly DK (1967) The representation of small-scale turbulence in numerical simulation experiments. IBM Form:195-210

Liu S, Katz J, Meneveau C (1999) Evolution and modelling of subgrid scales during rapid straining of turbulence. J Fluid Mech 387:281-320

Liu S, Meneveau C, Katz J (1994) On the properties of similarity subgrid-scale models as deduced from measurements in a turbulent jet. J Fluid Mech 275:83-119

Lucci F, Ferrante A, Elghobashi S (2010) Modulation of isotropic turbulence by particles of Taylor length-scale size. J Fluid Mech 650:5-55

Luo K, Wang Z, Li D, Tan J, Fan J (2017) Fully resolved simulations of turbulence modulation by high-inertia particles in an isotropic turbulent flow. Phys Fluids 29:113301

Ma BF, Jiang HG (2018) Estimation of perspective errors in 2D2C-PIV measurements for 3D concentrated vortices. Exp Fluids 59:1-14

Makita H, Sassa K (1991) Active turbulence generation in a laboratory wind tunnel Advances in turbulence 3. Springer, pp. 497-505

Mandø M, Lightstone M, Rosendahl L, Yin C, Sørensen H (2009) Turbulence modulation in dilute particle-laden flow. Int J Heat Fluid Flow 30:331-338

Mathieu J, Scott J (2000) An introduction to turbulent flow. Cambridge University Press,

Maxey MR, Riley JJ (1983) Equation of motion for a small rigid sphere in a nonuniform flow. The Physics of Fluids 26:883-889

Mazellier N, Danaila L, Renou B (2010) Multi-scale energy injection: a new tool to generate intense homogeneous and isotropic turbulence for premixed combustion. J Turbul 11:N43

Mehrabadi M, Horwitz J, Subramaniam S, Mani A (2018) A direct comparison of particle-resolved and point-particle methods in decaying turbulence. J Fluid Mech 850:336-369

Moisy F, Tabeling P, Willaime H (1999) Kolmogorov equation in a fully developed turbulence experiment. Phys Rev Lett 82:3994

Monchaux R, Bourgoin M, Cartellier A (2010) Preferential concentration of heavy particles: A Voronoï analysis. Phys Fluids 22:103304

Monchaux R, Bourgoin M, Cartellier A (2012) Analyzing preferential concentration and clustering of inertial particles in turbulence. Int J Multiphase Flow 40:1-18

Mostafa A, Mongia H (1988) On the interaction of particles and turbulent fluid flow. Int J Heat Mass Transfer 31:2063-2075

Oh JS, Lee H, Hwang W (2021) Motion blur treatment utilizing deep learning for time-resolved particle image velocimetry. Exp Fluids 62:1-16

Okamoto K, Nishio S, Kobayashi T, Saga T, Takehara K (2000a) Evaluation of the 3D-PIV standard images (PIV-STD project). J Visualization 3:115-123

Okamoto K, Nishio S, Saga T, Kobayashi T (2000b) Standard images for particle-image velocimetry. Meas Sci Technol 11:685

Olivieri S (2013) Analysis of the forces acting on particles in homogeneous isotropic turbulence. Ph. D. thesis, Universita degli Studi di Genova, Genova,

Paris AD (2001) Turbulence attenuation in a particle-laden channel flow. Stanford University,

Park HJ, Lee SG, Oh JS, Nam M, Barrett S, Lee S, Hwang W (2022) The effects of indoor temperature and humidity on local transmission of COVID-19 and how it relates to global trends. PloS one 17:e0271760

Park J, Park H (2021) Particle dispersion induced by vortical interactions in a particle-laden upward jet with a partial crossflow. J Fluid Mech 915

Perlman E, Burns R, Li Y, Meneveau C (2007) Data exploration of turbulence simulations using a database cluster Proceedings of the 2007 ACM/IEEE Conference on Supercomputing. pp. 1-11

Poelma C, Ooms G (2006) Particle-turbulence interaction in a homogeneous, isotropic turbulent suspension. Appl Mech Rev 59:78-90

Poelma C, Westerweel J, Ooms G (2006) Turbulence statistics from optical whole-field measurements in particle-laden turbulence. Exp Fluids 40:347-363

Poelma C, Westerweel J, Ooms G (2007) Particle–fluid interactions in grid-generated turbulence. J Fluid Mech 589:315-351

Pope SB (2000) Turbulent flows. Cambridge university press,

Raffel M, Willert C, Scarano F, Kähler CJ, Werely ST, Kompenhans J (2018) Particle image velocimetry: a practical guide, 3rd edn. Springer, Berlin

Raffel M, Willert CE, Scarano F, Kähler CJ, Wereley ST, Kompenhans J (2018) Particle Image Velocimetry: A Practical Guide. Springer,

Reeves M, Lawson N (2004) Evaluation and correction of perspective errors in endoscopic PIV. Exp Fluids 36:701-705

Richards A, Saad T, Sutherland JC (2018) A fast turbulence generator using graphics Processing Units 2018 Fluid Dynamics Conference. pp. 3559

Roach P (1987) The generation of nearly isotropic turbulence by means of grids. Int J Heat Fluid Flow 8:82-92

Rosa B, Pozorski J, Wang L-P (2020) Effects of turbulence modulation and gravity on particle collision statistics. Int J Multiphase Flow 129:103334

Saad T, Cline D, Stoll R, Sutherland JC (2017) Scalable tools for generating synthetic isotropic turbulence with arbitrary spectra. AIAA Journal 55:327-331

Saad T, Sutherland JC (2016) Comment on “Diffusion by a random velocity field”[Phys. Fluids 13, 22 (1970)]. Phys Fluids 28:22

Saito I, Watanabe T, Gotoh T (2019) A new time scale for turbulence modulation by particles. J Fluid Mech 880

Scarano F (2001) Iterative image deformation methods in PIV. Meas Sci Technol 13:R1

Scarano F, Riethmuller ML (1999) Iterative multigrid approach in PIV image processing with discrete window offset. Exp Fluids 26:513-523

Scarano F, Riethmuller ML (2000) Advances in iterative multigrid PIV image processing. Exp Fluids 29:S051-S060

Scharnowski S, Grayson K, de Silva CM, Hutchins N, Marusic I, Kähler CJ (2017a) New insights on the effect of light sheet mismatch on PIV correlations 12th International Symposium on Particle Image Velocimetry. Busan, Korea,

Scharnowski S, Grayson K, de Silva CM, Hutchins N, Marusic I, Kähler CJ (2017b) Generalization of the PIV loss-of-correlation formula introduced by Keane and Adrian. Exp Fluids 58:1-12

Scharnowski S, Kähler CJ (2016) Estimation and optimization of loss-of-pair uncertainties based on PIV correlation functions. Exp Fluids 57:23

Scharnowski S, Kähler CJ (2020) Particle image velocimetry-Classical operating rules from today's perspective. Opt Lasers Eng 135:106185

Schneiders L, Meinke M, Schröder W (2017) Direct particle–fluid simulation of Kolmogorov-length-scale size particles in decaying isotropic turbulence. J Fluid Mech 819:188-227

Schwarzkopf J, Crowe C, Riley J, Wetchagarun S, Dutta P (2009) Direct numerical simulation of stationary particles in homogeneous turbulence decay: Application of the k–ε model. Int J Multiphase Flow 35:411-416

Schwarzkopf JD, Crowe CT, Dutta P (2009) A turbulence dissipation model for particle laden flow. AlChE J 55:1416-1425

Sciacchitano A, Neal DR, Smith BL, Warner SO, Vlachos PP, Wieneke B, Scarano F (2015) Collaborative framework for PIV uncertainty quantification: comparative assessment of methods. Meas Sci Technol 26:074004

Sciacchitano A, Wieneke B (2016) PIV uncertainty propagation. Meas Sci Technol 27:084006

Sciacchitano A, Wieneke B, Scarano F (2013) PIV uncertainty quantification by image matching. Meas Sci Technol 24:045302

Shen J, Peng C, Wu J, Chong KL, Lu Z, Wang L-P (2022) Turbulence modulation by finite-size particles of different diameters and particle–fluid density ratios in homogeneous isotropic turbulence. J Turbul 23:433-453

Sheng J, Meng H, Fox R (2000) A large eddy PIV method for turbulence dissipation rate estimation. Chem Eng Sci 55:4423-4434

Squires K, Eaton JK (1994) Effect of selective modification of turbulence on two-equation models for particle-laden turbulent flows. J Fluids Eng 116:778-784

Squires KD, Eaton JK (1990) Particle response and turbulence modification in isotropic turbulence. Phys Fluids A 2:1191-1203

Sreenivasan KR (1995) On the universality of the Kolmogorov constant. Phys Fluids 7:2778-2784

Stanislas M, Okamoto K, Kähler C (2003) Main results of the first international PIV challenge. Meas Sci Technol 14:R63

Stanislas M, Okamoto K, Kähler CJ, Westerweel J (2005) Main results of the second international PIV challenge. Exp Fluids 39:170-191

Stanislas M, Okamoto K, Kähler CJ, Westerweel J, Scarano F (2008) Main results of the third international PIV challenge. Exp Fluids 45:27-71

Sung J (2001) Near-wake vortex motion behind a cylinder and its response to oscillatory flow by PIV measurements. Seoul National University,

Tanaka T, Eaton JK (2007) A correction method for measuring turbulence kinetic energy dissipation rate by PIV. Exp Fluids 42:893-902

Tanaka T, Eaton JK (2008) Classification of turbulence modification by dispersed spheres using a novel dimensionless number. Phys Rev Lett 101:114502

Tanaka T, Eaton JK (2010) Sub-Kolmogorov resolution particle image velocimetry measurements of particle-laden forced turbulence. Journal of Fluid Mechanics 643:177-206

Taylor J (1997) Introduction to error analysis, the study of uncertainties in physical measurements. University Science Books, Sausalito

Thielicke W, Sonntag R (2021) Particle Image Velocimetry for MATLAB: Accuracy and enhanced algorithms in PIVlab. J Open Res Software 9

Thielicke W, Stamhuis E (2014) PIVlab–towards user-friendly, affordable and accurate digital particle image velocimetry in MATLAB. J Open Res Software 2

Timmins BH, Wilson BW, Smith BL, Vlachos PP (2012) A method for automatic estimation of instantaneous local uncertainty in particle image velocimetry measurements. Exp Fluids 53:1133-1147

Tu J, Fletcher C (1994) An improved model for particulate turbulence modulation in confined two-phase flows. Int Commun Heat Mass Transfer 21:775-783

Vallée R, Henry C, Hachem E, Bec J (2018) Inelastic accretion of inertial particles by a towed sphere. Phys Rev Fluids 3:024303

Variano EA, Cowen EA (2008) A random-jet-stirred turbulence tank. J Fluid Mech 604:1-32

Vreman AW (2007) Turbulence characteristics of particle-laden pipe flow. J Fluid Mech 584:235-279

Vreman AW (2015) Turbulence attenuation in particle-laden flow in smooth

and rough channels. J Fluid Mech 773:103-136

Vreman AW (2016) Particle-resolved direct numerical simulation of homogeneous isotropic turbulence modified by small fixed spheres. J Fluid Mech 796:40-85

Webster DR, Brathwaite A, Yen J (2004) A novel laboratory apparatus for simulating isotropic oceanic turbulence at low Reynolds number. Limnol Oceanogr Methods 2:1-12

Westerweel J (1997) Fundamentals of digital particle image velocimetry. Meas Sci Technol 8:1379

Westerweel J, Elsinga GE, Adrian RJ (2013) Particle image velocimetry for complex and turbulent flows. Annu Rev Fluid Mech 45:409-436

Wieneke B (2015) PIV uncertainty quantification from correlation statistics. Meas Sci Technol 26:074002

Wilson BM, Smith BL (2013) Taylor-series and Monte-Carlo-method uncertainty estimation of the width of a probability distribution based on varying bias and random error. Meas Sci Technol 24:035301

Wilson BM, Smith BL (2013) Uncertainty on PIV mean and fluctuating velocity due to bias and random errors. Meas Sci Technol 24:035302

Wood A, Hwang W, Eaton JK (2005) Preferential concentration of particles in homogeneous and isotropic turbulence. Int J Multiphase Flow 31:1220-1230

Xu D, Chen J (2013) Accurate estimate of turbulent dissipation rate using PIV data. Exp Therm Fluid Sci 44:662-672

Xue Z, Charonko JJ, Vlachos PP (2014) Particle image velocimetry correlation signal-to-noise ratio metrics and measurement uncertainty quantification. Meas Sci Technol 25:115301

Yan F, Lightstone M, Wood P (2007) Numerical study on turbulence modulation in gas–particle flows. Heat Mass Transfer 43:243-253

Yang T, Shy S (2005) Two-way interaction between solid particles and homogeneous air turbulence: particle settling rate and turbulence modification measurements. J Fluid Mech 526:171-216

Yeung P, Zhou Y (1997) Universality of the Kolmogorov constant in numerical simulations of turbulence. Phys Rev E 56:1746

Yokomine T, Shimizu A (1995) Prediction of turbulence modulation by using k-ε model for gas-solid flows Multiphase Flow 1995. Elsevier, pp. 191-199

Yokomine T, Shimizu A, Saitoh A, Higa K (2002) Heat transfer of multiple impinging jets with gas–solid suspensions. Exp Therm Fluid Sci 26:617-626

Yoon JH, Lee SJ (2002) Direct comparison of 2D PIV and stereoscopic PIV measurements. Meas Sci Technol 13:1631

Zimmermann R, Xu H, Gasteuil Y, Bourgoin M, Volk R, Pinton J-F, Bodenschatz E, Research ICfT (2010) The Lagrangian exploration module: An apparatus for the study of statistically homogeneous and isotropic turbulence. Rev Sci Instrum 81:055112

국문 초록

작고 무거운 입자에 의해 변화하는 균질 등방성 난류에 대한 실험 및 이론적 연구

서울대학교 공과대학

기계항공공학부

이 훈 상

입자에 의한 난류의 변화는 오랜 기간 풀리지 않은 난제이다. 선행 연구에서는 입자가 포함된 난류에서의 물리량을 예측하기 위한 다양한 모델들이 제시되어 왔다. 그러나 이러한 모델들은 한계점들을 가지며, 이들 중 몇몇은 실험적으로 입증되지 않았다. 본 연구에서는 균질한 등방성 난류 (HIT)를 이용하여, 입자에 의해 변화하는 난류 운동 에너지 (TKE)와 소산율을 실험적으로 조사하였다. 입자의 직경은 164 μm (HIT의 Kolmogorov scale과 유사한 크기)이고 밀도는 수송상 (carrier phase)인 air에 비해 약 2,000배 가량 더 크다. 2D 입자영상유속계 (PIV)로 입자 투입 이전과 이후의 HIT를 관찰하였다. 입자를 투입하기 이전 난류의 Taylor microscale Reynolds 수는 271까지 도달하였다. TKE와 rms velocity를 통해 확인했을 때, 난류는 상당히 균질하고 등방성을 가졌다. 계산된 에너지 스펙트럼 역시 생성된 난류가 등방성 난류 이론을 따르고 있음을 검증한다. 작고 무거운 입자가 이 HIT에 추가되는 경우, TKE와 소산율이 감소하는 것으로 나타났다. 난류의 수송방정식에서 시작하여 TKE와 소산율에 대한 새로운 물리 모델을 유도하였다. 점 입자 접근법 (point-particle

approach)의 한계를 극복하기 위해, 입자 표면에서 발생하는 추가 소산과 입자의 유한한 크기에 의해 발생하는 후류 효과를 고려하였다. 새로 제안된 모델은 만족스러운 성능을 보였으며, 실험 데이터와 일치하게 나타났다.

주요어: 입자 포함 난류, 다상 유동, 균질한 등방성 난류, 난류 변조, 입자-난류 상호작용

학번: 2017-24654